Computational multi-scale constitutive model for wood cell-wall mechanics.

Saavedra Flores, Erick Isaac

Swansea University
Prifysgol Abertawe

Computational Multi-scale Constitutive Model for Wood Cell-wall Mechanics

by

Erick Isaac Saavedra Flores

Submitted to Swansea University in fulfillment of the requirements for the degree of Doctor of Philosophy

Swansea University

Swansea

July 2011

DECLARATIONS

(i) This work has not previously been accepted in substance for any degree and is not being concurrently submitted in candidature for any degree.

Signed ..... (candidate)

Date 14/July/2011

(ii) This work is result of my own work and investigation, except where otherwise stated. Other sources have been acknowledged by giving explicit references. A bibliography is appended.

Signed ..... (candidate)

Signed ..... (supervisor)

Date 14/July/2011

(iii) I hereby give consent for my thesis, if accepted, to be available for photocopying and inter-library loan, and for the title and summary to be made available to outside organizations.

Signed ..... (candidate)

Date 14/July/2011

Acknowledgments

I want first to thank my supervisor Dr Eduardo de Souza Neto for the help and guidance provided during these years of PhD studies.

The financial support from the Department of Civil Engineering from the University of Santiago, Chile, that makes possible my studies is also gratefully acknowledged.

I would like to thank my sister, Betsy, and my brother, Adolfo, who have always been in my heart and have constituted exceptional role models to follow since we were children and I was the youngest one. Our beautiful friendship means a lot to me and I hope to pass this example of attachment on to my children along their lives.

I also wish to express my gratitude to my parents, Hernán Saavedra and Besis Flores, for giving me life in the first place, for their unconditional support and continuous encouragement. To my father, who sowed the seeds that led to my interest in science, and to my mum, who taught me what love, care and comprehension mean.

Special thanks (strictly in alphabetic order) to my nephew Alvarito, my sister-in-law, Claudia, my cousin Gerald, my mother-in-law, Isabel, my niece Ivanita, my aunty Juani, my sister-in-law, Mariana, my father-in-law, Mario, my former brother-in-law, Paulo, my niece Valentinita and finally, my nephew Vicentito. I love them.

I devote my deepest love to my two children Francisca and Benjamín. They are the reason of my life. I admire them and am sure that they will become great persons. I will always be proud of them. God bless them.

I am most grateful and deeply indebted with you, Natalia. I would never have embarked in this journey without your support, guidance and unconditional love. All my everlasting love for you.

Finally, I would like to dedicate this thesis to my god father Claudio who sadly passed away few months ago before I finished this dissertation. Your love, kindness and teachings will forever remain in our memories.

Swansea, Wales, United Kingdom. 2011.

SUMMARY

This research investigates the non-linear irreversible behaviour of wood cell-walls by means of a finite element-based computational multi-scale approach. A finite strain three-scale model is proposed where the overall response of the cell-wall composite is obtained by the computational homogenisation of a Representative Volume Element (RVE) of cell-wall material, called here *microfibril–RVE*. This RVE is composed of three basic constituents: hemicellulose, lignin and cellulose, and the latter with its corresponding crystalline and amorphous fractions. Furthermore, in a lower scale, the crystalline and amorphous portions of cellulose form a periodic arrangement represented by a single material whose mechanical response prediction, in turn, involves the computational homogenisation of a RVE, named *cellulose core–RVE*. Numerical material tests are conducted with the proposed model. The results are compared to published experimental data and demonstrate the predictive capability of the proposed model in capturing key features of cell-wall behaviour, such as fibre reorientation-induced stiffening, viscous relaxation, recovery mechanism and hysteresis. The present results suggest a failure mechanism for the cell-wall under straining, which is associated with the inelastic yielding of the amorphous portion of cellulose fibres.

In order to reduce CPU times and memory requirements in the present three-scale finite element model, this research also addresses the impact of the use of symmetry conditions in multi-scale models. Two types of RVE symmetry often found in practice are considered: staggered-translational and point symmetry. These are analysed under three types RVE of kinematical constraints: periodic boundary fluctuations, linear boundary displacements (which gives an upper bound for the macroscopic stiffness) and the minimum kinematical constraint (corresponding to uniform boundary tractions and providing a lower bound for the macroscopic stiffness). Numerical examples show that substantial savings in computing times are achieved by taking advantage of such symmetries. Speed-up factors in excess of seven have been found in such cases, when both symmetry conditions considered are present at the same time. In addition, for completeness, the direct enforcement of such constraints within a Newton-based finite element solution procedure for the RVE equilibrium problem is detailed in this thesis.

Contents

List of Figures

Notation

$\boldsymbol{B}^e$	Elastic left Cauchy-Green strain tensor
$\boldsymbol{b}$	RVE body force vector
$\mathbf{B}$	Global strain-displacement matrix
$\mathscr{C}'$	Configuration $\mathscr{C}$ rotated in 180°
$\mathscr{C}$	Original configuration of the RVE
$\mathbf{C}$	Constraint matrix
$\mathbf{D}$	Consistent tangent operator
$\boldsymbol{e}_j$	Generic base vector
E	Young's modulus
ev	Volumetric degree of crystallinity of cellulose
$\dot{\boldsymbol{F}}$	Macroscopic deformation gradient rate tensor
$\mathfrak{F}_y$	Functional associated with point $\boldsymbol{y}$ which maps the strain history, $\boldsymbol{\varepsilon}_\mu^t$, up to time t, into the stress $\boldsymbol{\sigma}_\mu$ of time t
$\mathbf{F}$	Residual force vector
$\boldsymbol{F}_\mu$	Microscopic deformation gradient defined over the local RVE
$\boldsymbol{F}$	Deformation gradient at any arbitrary point $\boldsymbol{x}$ of the macroscopic continuum
$\dot{\boldsymbol{F}}_\mu$	Microscopic deformation gradient rate tensor
$\hat{G}$	Incremental virtual work functional
G	Virtual work functional
H	Hardening modulus
$\mathbb{I}$	Fourth-order identity tensor
$\boldsymbol{I}$	Second-order identity tensor
J	Jacobian of the deformation map

$\mathbf{K}$	Tangent stiffness matrix
K	Bulk modulus
l	Characteristic length of the macroscopic continuum
l_μ	Characteristic length of RVE
$\mathscr{L}_v$	*Lie derivative*
MFA	Microfibril angle
$\boldsymbol{n}$	Outward normal unit vector
$\boldsymbol{n}^j$	Outward unit vector, normal to the subset Γ^j
$\mathbf{N}_b$	Matrix of shape functions of the elements sharing the boundary $\partial\Omega_\mu^h$ of the discretised RVE
$\hat{\mathbf{P}}_\mu$	Incremental constitutive functional at the RVE level that delivers the array of First Piola-Kirchhoff stress components
$\hat{\boldsymbol{P}}_\mu$	Approximate incremental microscopic constitutive function
$\boldsymbol{P}_\mu$	Microscopic first Piola-Kirchoff stress tensor
$\boldsymbol{P}$	Macroscopic or homogenised first Piola-Kirchoff stress tensor
$\boldsymbol{p}^j$	Constant vector associated with the pair of cell sides j of $\partial\Omega_\mu$
$\boldsymbol{q}^j$	Constant vectors defined by a staggered-translational mapping between points of subdomains Ω_+^j and Ω_-^j
RVE	Representative Volume Element of material
t	Instant of time
$\boldsymbol{t}^e$	External surface traction vector
$\tilde{\boldsymbol{u}}_\mu$	Displacement fluctuation field
$\tilde{\mathbf{u}}_\mu$	Array of global nodal displacement fluctuations
$\boldsymbol{u}_\mu$	RVE (or microscropic) displacement field
$\mathscr{V}_\mu$	Functional set of kinematically admissible displacement fluctuations
$\mathscr{V}_\mu^h$	Finite element discretisation of $\mathscr{V}_\mu$
V_μ	Volume of the RVE associated to point $\boldsymbol{x}$ of the macroscopic continuum, in the *reference* configuration

$\boldsymbol{x}$ Arbitrary point of the macroscopic continuum

$\boldsymbol{y}_\oplus, \boldsymbol{y}_\ominus$ Pair of points with a one-to-one correspondence given by point-symmetry

$\boldsymbol{y}$ Arbitrary point of the microscopic continuum

$\boldsymbol{y}_+, \boldsymbol{y}_-$ Pair of points with a one-to-one correspondence given by the standard periodicity or by staggered-translational symmetry

$\boldsymbol{z}^j$ Zero Nodal displacement fluctuations vector with $j = 1 \ldots N$points

α Ogden hyperelastic constant for a model with 1 term in the Ogden strain-energy function serie

$\boldsymbol{\alpha}$ Set of internal variables

$\Delta\mu$ Variation of MFA

Δt Time interval

$\delta\tilde{\mathbf{u}}_\mu^{(k)}$ Iterative correction to the displacement fluctuation during a typical Newton iteration (k)

$\partial\Omega_\mu$ Boundary of RVE domain

$\partial^{1/2}\Omega_\mu$ Boundary of half RVE domain

$\partial^{1/4}\Omega_\mu$ Boundary of quarter RVE domain

$\partial\Omega_\mu^h$ Finite element discretisation of $\partial\Omega_\mu$

$\partial^{1/2}\Omega_\mu^h$ Finite element discretisation of $\partial^{1/2}\Omega_\mu$

$\partial^{1/4}\Omega_\mu^h$ Finite element discretisation of $\partial^{1/4}\Omega_\mu$

$\boldsymbol{\varepsilon}_\mu$ Microscopic strain tensor field

$\boldsymbol{\varepsilon}_\mu^t$ Microscopic strain history up to time t

$\dot{\boldsymbol{\varepsilon}}$ Macroscopic strain rate field

$\boldsymbol{\varepsilon}$ Finite element array of macroscopic engineering strains

$\boldsymbol{\varepsilon}$ Macroscopic or homogenised strain tensor

$\dot{\boldsymbol{\varepsilon}}_\mu$ Microscopic strain rate field

Γ^j Subset of the boundary $\partial\Omega_\mu$ associated with the pair j of cell sides

$^{1/2}\Gamma^j$ Subset of the boundary $\partial^{1/2}\Omega_\mu$ associated with the pair j of cell sides

μ Microfibril angle

ν Poisson ratio

μ_o Initial microfibril angle

$\boldsymbol{\eta}$ Virtual displacement vector

$\boldsymbol{\eta}$ Array of global nodal virtual displacements

η_m Deviatoric viscosity parameter in the Maxwell model

η_p Viscosity-related parameter in the Prandtl model

Ω_μ RVE domain in its *reference* configuration

$^{1/2}\Omega_\mu$ Half RVE domain

$^{1/2}\Omega_\mu^h$ Finite element discretisation of $^{1/2}\Omega_\mu$

$^{1/4}\Omega_\mu^h$ Finite element discretisation of $^{1/4}\Omega_\mu$

$^{1/4}\Omega_\mu$ Quarter RVE domain

Ω_μ^h Finite element discretisation of Ω_μ

Φ Von Mises yield function

Ψ Ogden strain energy function

$\boldsymbol{\sigma}_\mu$ Microscopic Cauchy stress tensor field

$\hat{\boldsymbol{\sigma}}_\mu$ Incremental constitutive function for the microscopic Cauchy stress tensor

$\hat{\boldsymbol{\sigma}}_\mu$ Incremental constitutive functional at the RVE level that delivers the array of Cauchy stress components

σ_{sy} Shear yield stress for the conventional von Mises model

σ_y Initial yield stress (uniaxial yield stress for the conventional von Mises and Tresca models)

$\boldsymbol{\sigma}$ Macroscopic or homogenised Cauchy stress tensor field

$\boldsymbol{\sigma}$ Finite element array of macroscopic or homogenised engineering stress array

$\boldsymbol{\tau}$ Kirchhoff stress tensor

χ Ogden hyperelastic constant for a model with 1 term in the Ogden strain-energy function serie

λ_j Principal stretches with $j = 1 \ldots 3$

Ξ Dissipation potential

$\langle \cdot \rangle$ Ramp function

∇ Material gradient operator with respect to the *reference* coordinates

∇^s Symmetric gradient operator

$\otimes$ Standard tensorial product

$\otimes_s$ Symmetric tensor product

$\{+,-\}$ Subscripts associated with the set $+$ and $-$ of points (nodes) which satisfy periodic constraint or staggered-translational symmetry in the RVE (mesh)

$\{i,b\}$ Subscripts associated with the corresponding set of interior and boundary points (nodes) of the RVE (mesh)

$\{\oplus,\ominus\}$ Subscripts associated with the corresponding set $\oplus$ and $\ominus$ of points (nodes) which satisfy point symmetry in the RVE (mesh)

$\{d,f,p\}$ Subscripts associated with the corresponding set of *dependent*, *free* and *prescribed* degrees of freedom in the RVE mesh

$det(\cdot)$ Determinant of $(\cdot)$

CHAPTER 1

Introduction

1.1 Objectives and methodology

Over the last few years, the investigation of complex and intricate mechanisms of wood at nano- and microscopic scale levels, has shown remarkable progress, particularly in relation to the understanding of the linear elastic material response by means of conventional multi-scale finite element models (Holmberg et al. 1999, Hofstetter et al. 2005, Hofstetter et al. 2007, Qing and Mishnaevsky 2009*a*, Qing and Mishnaevsky 2009*b*, Qing and Mishnaevsky 2010).

Despite the fact that such multi-scale models offer the possibility of describing more accurately the stress response under complex strain paths of difficult representation by means of conventional internal variable-based phenomenological models, at present only few attempts have been made in capturing the non-linear dissipative response of wood at various scales.

Probably one of the crucial factors in understanding the mechanical dissipation of wood across different scales is the role that the three major nanostructural constituents play and the irreversible processes that they show in the cell-wall. These are hemicellulose, lignin and cellulose, and the latter with its corresponding crystalline and amorphous fractions.

Despite the considerable effort devoted to the experimental study of the basic constituents in the cell-wall, only little is known at present about their mechanical properties and interactions (Burgert et al. 2006). An important contribution in the understanding of cell-wall mechanics has been given by Keckés and his co-workers (Keckés et al. 2003). They showed how wood tissue and individual cells are able to undergo large strains without apparent damage. They have proposed a recovery mechanism after irreversible deformation, interpreted as a *stick-and-slip* mechanism at the molecular level. They showed that this *velcro*-like mechanism provides a plastic response similar to the crystallographic sliding in polycrystalline metals.

The main objective of this research is to investigate the highly non-linear irreversible behaviour of wood cell-wall by means of a finite element-based computational multi-scale approach. In an attempt to capture the main non-linear phenomenological responses found in the cell-wall, a fully coupled three-scale finite element model is proposed where the cell-wall material is idealised as a periodic microstructure.

One of the most important goals of the present research is the numerical modelling of the following features found in the cell-wall material: fibre reorientation-induced stiffening, viscous relaxation, recovery mechanism and loading/unloading processes. Here, we anticipate that a very good predictive capability is shown when the homogenised mechanical response of the present model is compared with experimental information. Moreover, from the numerical results, it is found that yielding in the amorphous fraction of the cellulose could be interpreted as a potential mechanism of failure in the wood cell.

In order to reduce computing times and memory requirements in the present three-scale finite element-based model, this research has also addressed the use of symmetry conditions in the reduction of CPU times. If, on one hand, multi-scale finite element models offer the possibility of describing more accurately the stress response under complex strain paths, on the other hand they suffer from the drawback of excessive computing costs. These costs are usually acceptable when finite element analyses of a single RVE are used to calibrate parameters of a macroscopic phenomenological model (refer, for instance, to Giusti, Blanco, de Souza Neto and Feijóo (2009), Pellegrino et al. (1999) and Speirs et al. (2008)). However, when fully coupled multi-scale finite element analyses are needed (Matsui et al. 2004, Miehe et al. 2002, Terada et al. 2003), where the macroscopic equilibrium problem is solved simultaneously with one RVE equilibrium problem per macroscopic Gauss quadrature point, computing times and memory requirements soon become prohibitive. In such cases, even with the use of simple phenomenological models and relatively coarse meshes at the RVE level, computing costs may rise by several orders of magnitude when compared to conventional single-scale analyses of similarly sized macroscopic problems. To address this issue, various strategies, including the use of parallel processing, sub-stepping schemes and the use of more efficient linear solvers, have been suggested in the literature (Matsui et al. 2004, Somer et al. 2009). It is emphasised that regardless of any strategies adopted to reduce computational costs, the choice of the smallest possible RVE always remains a crucial factor. Two types of symmetry are considered: staggered-translational and point symmetry. It is remarked that the direct enforcement of such symmetry conditions within a Newton-based finite element solution procedure for the RVE equilibrium problem is straightforward and, for completeness, is detailed in this thesis. We anticipate here that substantial savings in computing times are shown by numerical examples. For instance, speed-up factors in excess of seven are found when both symmetries considered are present at the same time.

1.2 Layout of the thesis

The present thesis consists of 6 chapters organised as follows.

The present Chapter 1 discusses the objectives and methodology of this work. Some results are anticipated here.

Chapter 2 presents a brief review of wood mechanics at different scales. Here, the structure of wood at macro- and microscopic scale is studied. The chemical constituents present in the wood cell-wall are also reviewed. At the end of this chapter, the mechanics of wood cell and wood cell-wall is described.

Chapter 3 presents the theoretical background of the adopted homogenisation-based multi-scale theory in continuum form as described in (de Souza Neto and Feijóo 2006, de Souza Neto and Feijóo 2010). First, the basic principles of the theory under the infinitesimal strains framework, and the fundamental concept of Representative Volume Element are reviewed. Then, the linear boundary displacement, the periodic boundary displacement fluctuations and the uniform boundary tractions model are introduced, with their corresponding finite element implementations. At the end of the chapter, the theory is extended to the finite strains case.

The symmetry considerations are presented in Chapter 4 together with their corresponding computational implementation within the adopted implicit finite element framework. Numerical examples showing substantial savings in CPU times when symmetries are considered are also presented in this Chapter.

The finite element-based multi-scale model of wood cell-wall is presented in Chapter 5. The main numerical tests are conducted here. The results are compared to published experimental data and are also discussed in detail. Key features of cell-wall behaviour are addressed, such as fibre reorientation-induced stiffening, viscous relaxation, recovery mechanism and hysteresis.

Finally, Chapter 6 summarises the main conclusions obtained from the present thesis.

As a general scheme of notation, throughout this thesis scalars are written as italic light-face letters; points, first and second order tensors as italic bold-face letters; and finite element arrays (vectors and matrices) as upright bold-face letters.

CHAPTER 2

Structure and mechanics of wood at different scales

The purpose of this chapter is to describe briefly the morphology and composition of wood at different scales. For further information, we refer, for instance, Kollman and Côté (1968), Dinwoodie (1981), Bodig and Jayne (1982) and Smith et al. (2003).

2.1 Structure of wood at macroscopic scale

At macroscopic scale, trees trunks show a typical internal structure, consisting of multiple concentric layers through their corresponding cross-sections (refer to Figure 2.1). The first and outermost layer corresponds to the bark, which can be divided into an inner and an outer portion. The inner bark comprises great part of the living tissue of the tree and is composed by the *cork cambium*, where new layers of cork are formed, and by the *secondary phloem*, where large quantities of nutrients are transported throughout the tree. The outer bark comprises deposits of dead cells. Inwards, the next layer is called *vascular cambium*, where new wood cells are produced, along with the relegation of older cells into the bark or into the inner region of the trunk. Within the bark, and comprising the *vascular cambium* and the bulk of the stem is the wood, represented by two main regions concentrically distributed around the *pith* or central portion of the trunk. The first outer region is called *sapwood*, whose principal functions are structural support, transport of water and minerals and storage of carbohydrate reserves. It represents from 10% to 60% of the total radius of the tree trunk (Dinwoodie 1981). The second inner region is named *heartwood* and accomplishes functions of support and resistance to decay. Since *sapwood* contains the most nutrients reserves, it is highly attractive to the attack of decay organisms, becoming much less durable than *heartwood*.

2.2 Wood microstructure

Microscopically, wood is composed mainly by an arrangement of long slender tubular cells, oriented nearly parallel to the axis of the stem and firmly

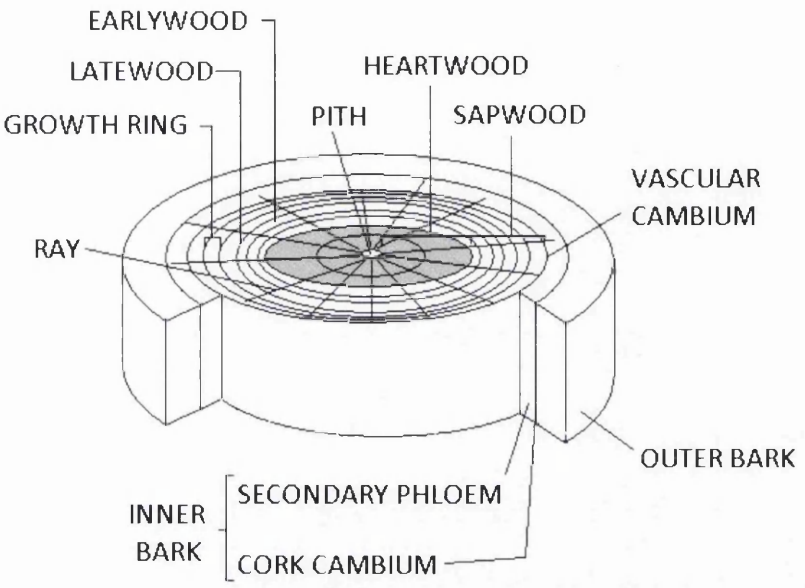

Figure 2.1: Diagramatic illustration of the cross-section of a trunk, showing the principal structural features.

cemented together, with dimensions and shapes variable within a tree and among species (refer to Figure 2.2).

In hardwoods, this cellular microstructure consists basically of three types of cells, called *fibres*, *vessels* and *parenchimas*, whose main functions are structural support, water transport and storage, respectively.

Generally, *fibres* are elongated cells, averaging 1.2mm long and 10 - 50μm in diameter (Tsoumis 1991). Their walls are considerably thicker than those of *vessels* and normally they are sparsely perforated. On the contrary, *vessels* are usually shorter, of length about 0.2 – 1.2mm and relatively wide, up to 0.5mm (Dinwoodie 1981). *Parenchimas* are usually present horizontally, in the form of rays (Figure 2.1) or vertically, either homogeneously distributed or in distinct zones.

In softwoods, *tracheids* are the most common type of cell (Figure 2.3). Usually they have poligonal cross-sections and their principal functions are support and transport of water and minerals. Their length varies from 3 to 4mm with diameters between 30 – 40μm (Gardner 2002).

As a consequence of seasonal changes, most tree species show periodical variations in the thickness and width of *tracheids*, represented by concentric growth rings (Figure 2.4). Cells developed during rainy months of the year, when the dominant function is conduction, are called *earlywood tracheids*, being characterised by thin walls with thickness of about 1.78μm thick (Bodig and Jayne 1982). Cells generated during dry months, when the main function

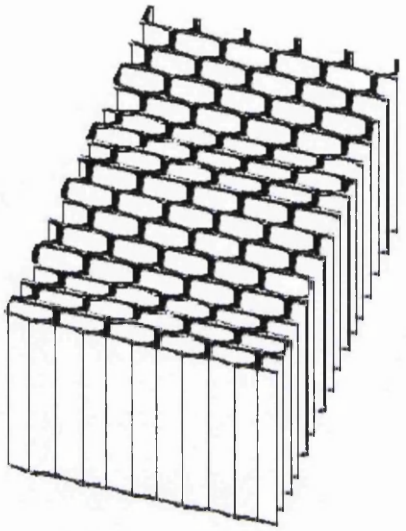

Figure 2.2: Typical microscopic cellular arrangement in wood.

is support, are called *latewood tracheids* and have thicknesses up to 10μm (Dinwoodie 1981).

Additionally, other types of *tracheids* in softwoods can be found in the lower side of branches and in inclined stems. They are called *compression wood* and commonly have round cross-sections and thick cell-walls. For instance, in Norway spruce, typical *compression wood tracheids* have an average thickness of 4.6μm, mean length of 2.2mm and an average diameter of $21.1\,\mu$m (Tarmian and Azadfallah 2009). In order to illustrate the morphological differences among *compression wood*, *earlywood* and *latewood tracheids*, Figure 2.5 shows their corresponding cross-section views.

2.3 Nanoscopic constituents in the wood cell-wall

At the nanoscopic level, wood cell-wall contains three major chemical constituents: cellulose, hemicellulose and lignin. Cellulose is encountered in a proportion of 40 – 50% by weight of wood substance, hemicellulose in 25% and lignin between 20 – 30% approximately (Smith et al. 2003).

Cellulose is a long polymer composed of glucose units. It is organised into periodic arrangements of crystalline and amorphous (non-crystalline) regions along their length, called in what follows crystalline-amorphous cellulose core (refer to Figure 2.6 for further details). This periodic arrangement is covered with an outer surface layer made up of amorphous cellulose (Xu et al. 2007). The proportion of crystalline volume is determined by its (volumetric) degree

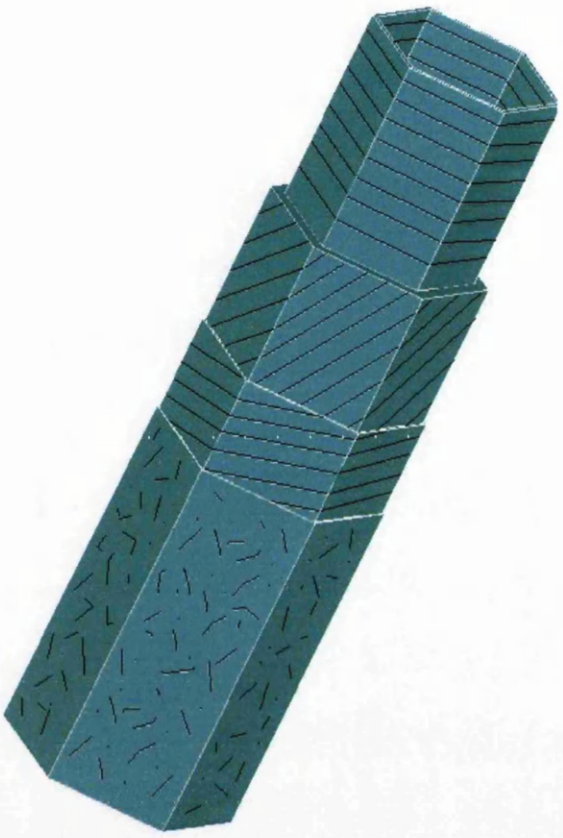

Figure 2.3: Typical wood *tracheid* with four layers in the cell-wall. From inside to outside, these are the S3, S2, S1 and P-M layers. The different orientations of the cellulose fibres through the cell-wall result in an increase of the overall stiffness in the wood cell.

of crystallinity. The high stiffness of the cellulose is due to its crystalline fraction whereas its flexibility is provided by the amorphous part (Timar-Balazsy and Eastop 1998). Only its non-crystalline fraction may absorb moisture and consequently, change its mechanical properties.

Contrary to crystalline cellulose, hemicellulose is a polymer with little strength, built up of sugar units. Its structure is partially random, with mechanical properties highly sensitive to moisture changes, becoming very soft with the presence of water and stiff with the loss of moisture.

Lignin is a complete amorphous polymer that contributes to cement the individual cells together and to provide shear strength. It is the most hydrophobic component in the cell-wall, with relatively stable mechanical properties under moisture changes.

These three main constituents, cellulose, hemicellulose and lignin, form a complex network characterised by cellulose acting as a fibre embedded in a

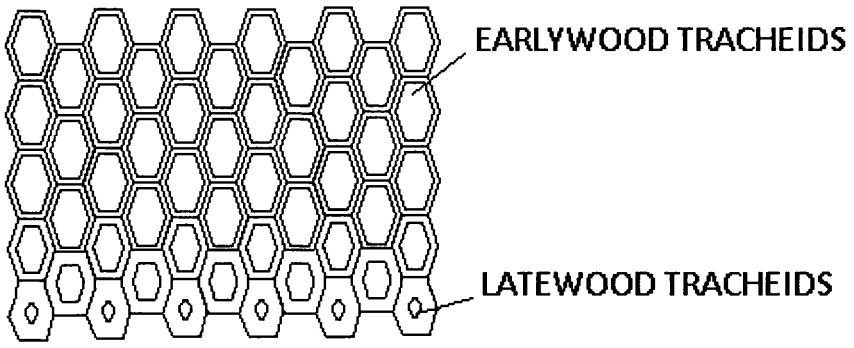

Figure 2.4: Variation in the morphology of wood cells, indicating *earlywood tracheids* and *latewood tracheids*.

matrix composed by hemicellulose and lignin. This spatial arrangement of components is known as *microfibril*, and can be considered as a periodic unit building block of rectangular cross-section with infinite length (see Figure 2.7).

The specific orientation of *microfibrils* relative to the longitudinal cell axis is called *microfibril angle* (MFA) and constitutes one of the most important parameters controlling the balance between stiffness and flexibility in trees.

Depending on the proportions of chemical components and *microfibril angle*, the cell-wall of softwood *tracheids* can be divided in the following layers (refer to Figure 2.3). The layer which connects two adjacent cells is called middle lamella (M). It is characterised by the significative abundance of lignin. The subsequent layer is referred to as primary wall (P). Commonly, this latter is very thin and therefore both layers, P and M, are treated as compound middle lamella. The remaining internal portion of cell-wall is called secondary and can be subdivided into outer (S1), middle (S2) and inner (S3) layers.

Through the cell-wall, the *microfibril* takes different orientations, generating a mechanical locking effect and consequently, an increase in the overall stiffness in the cell (Perré and Keey 2007). Among all these layers, S2 is the thickest and most influential factor in the mechanical behaviour of wood cells. It comprises about 80 – 90% of the total volume of cell-wall (Hofstetter et al. 2005) and concentrates a high content of cellulose corresponding to 50% by weight (Bodig and Jayne 1982). Because of the structural importance of this layer, in what follows the term MFA will be used exclusively to indicate the orientation of the *microfibril* in the S2 cell-wall layer (refer to Figure 2.8).

For further information about cell-wall layers and their functions from a structural point of view, we refer to Booker and Sell (1998).

2.4 Mechanics of wood cell and cell-wall

Depending mainly on the structural function, wood cells can exhibit notable differences in MFAs within each tree. For instance, *compression wood* cells are characterised by having large MFAs in tree branches in order to withstand strong wind loads and continuous vibrations without breaking. A sufficiently large MFA allows the cell to be more flexible and consequently to tolerate adequately the high levels of deformation encountered naturally in branches. On the contrary, in trunks of tall trees, *earlywood* and *latewood tracheids* present low MFAs to ensure a stiffer stem and to support the increasing weight of the tree (Figure 2.9). Experimental information about the influence of MFA on the overall stiffness of wood cells obtained by tensile testing has been reported widely (Sedighi-Gilani and Navi 2007).

Despite the considerable amount of experimental investigation carried out in wood cell and cell-wall in recent years, only little is known about mechanical properties and mechanical interactions among its constituents (Burgert et al. 2006). However, one of the most important contributions in the understanding of cell-wall mechanics has been given recently by Keckés and his co-workers (Keckés et al. 2003). By means of tensile tests on *compression wood* tissues and individual cells of Norway spruce, they reported a change in the orientation of the MFA from 46^o to 35^o when an axial strain of 20% was applied. This reorientation of MFA was interpreted as a mechanism of shear deformation in the lignin-hemicellulose matrix, allowing cellulose fibres to rotate into an orientation more parallel to the cell axis. In addition, they showed how wood tissue and individual cells are able to undergo large deformations without apparent damage during tensile tests. Furthermore, they pointed out a recovery mechanism after irreversible deformation, interpreted as a *stick-and-slip* mechanism at the molecular level. They showed that this *velcro*-like mechanism provides a plastic response similar to that encountered in metals due to crystallographic sliding.

As shall be seen later, one of the main contributions of the present work will be the development of a multi-scale finite element model in order to study the complex non-linear phenomena present within the wood cell-wall. In what follows, we describe the basis of the homogenisation-based multi-scale theory.

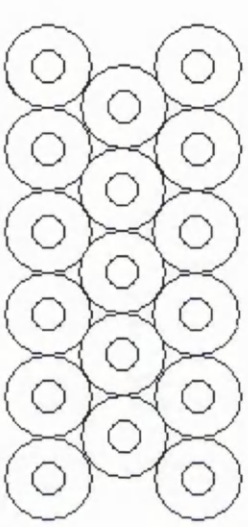

(a) *Compression wood tracheids.*

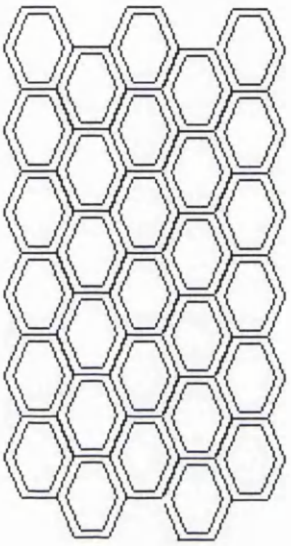

(b) *Earlywood tracheids.*

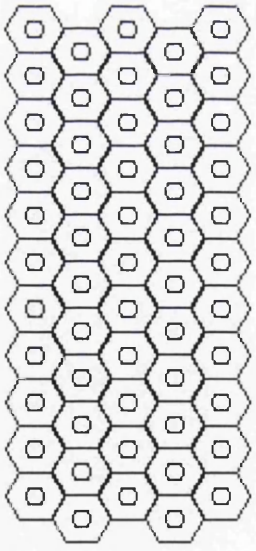

(c) *Latewood tracheids.*

Figure 2.5: Cross-section views of different *tracheids*.

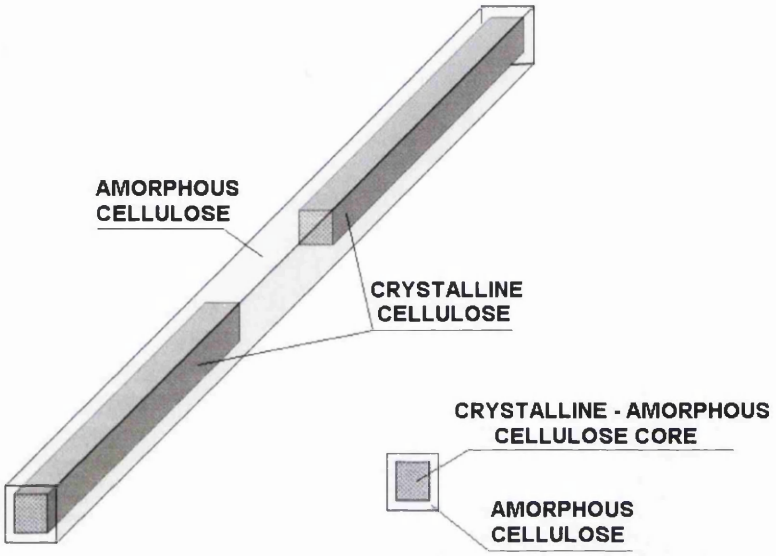

Figure 2.6: Schematic representation of cellulose with its crystalline and amorphous fractions.

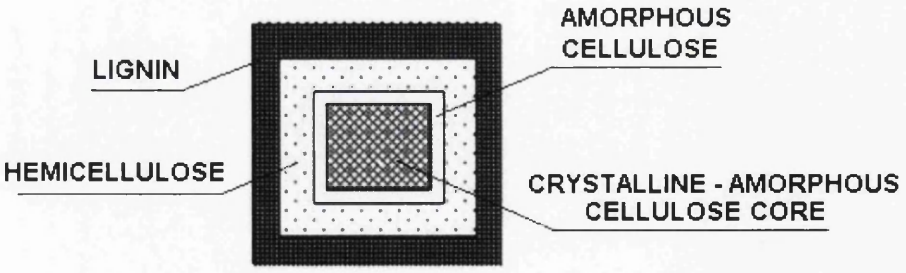

Figure 2.7: Idealised representation of the *microfibril* with its basic components in the wood cell-wall.

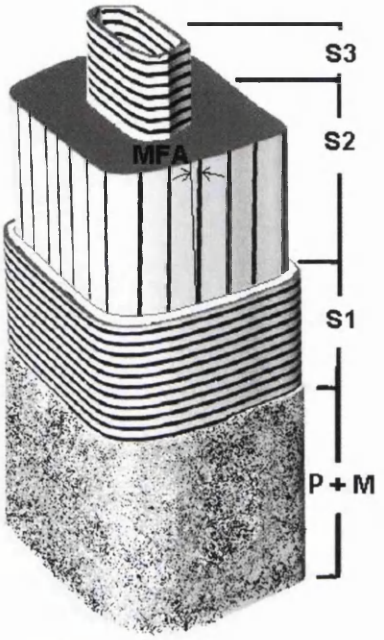

Figure 2.8: Typical *tracheid* with its different layers and *microfibril angle* (MFA).

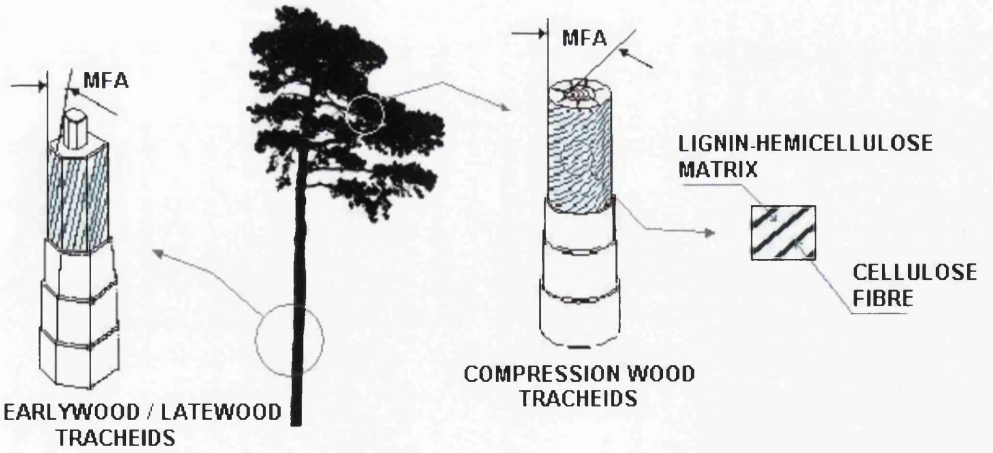

Figure 2.9: MFA of *earlywood/latewood tracheids* and *compression wood* cells in different parts of a tree. Depending on the structural function, MFA may vary considerably to provide more flexibility in the branches or more stiffness in the trunk.

CHAPTER 3

Homogenisation-based multi-scale theory

3.1 Introduction

Over the last two decades, homogenisation-based multi-scale constitutive modelling techniques relying on the volume averaging of the stress and strain fields over a Representative Volume Element (RVE) of material have attracted considerable attention within the Computational Mechanics community (Giusti, Novotny, de Souza Neto and Feijóo 2009, Matsui et al. 2004, Michel et al. 1999, Miehe et al. 1999, Miehe et al. 2002, Pellegrino et al. 1999, Castaneda 1991, Suquet 1993, Terada et al. 2003). The interest in this area stems mainly from the suitability of multi-scale models of this type for finite element implementation and, more importantly, from their potential ability in capturing non-linear response of difficult representation by means of conventional internal variable-based phenomenological models. In this context, the development of multi-scale constitutive models seems to be a very promising alternative for the description of complex solid materials, circumventing the natural limitations of the classical phenomenological approaches.

The formulation presented here provides an axiomatic variational framework for the family of multi-scale constitutive theories. Here, the main assumptions are: the local strain and stress volume averaging relationships; the Principle of Virtual Work for the RVE; the choice of a set of kinematical constraints over the RVE domain; and the Hill-Mandel Principle of Macro-Homogeneity (Hill , 1965; Mandel , 1971). In what follows, the description of the above variational approach is given. For further details, we refer to de Souza Neto and Feijóo (2006).

3.2 Infinitesimal multi-scale constitutive theory

The point of departure of the present family of homogenisation-based multi-scale constitutive theories of solids is the assumption that stresses and strains at any arbitrary point $\boldsymbol{x}$ of the macroscopic continuum are the volume average of the microscopic stress and strain tensor fields defined over a local representative volume element (RVE). The RVE is such that its domain Ω_μ has a

characteristic length, l_μ, much smaller than that of the macroscopic continuum, l, and at the same time, is sufficiently large to represent the mechanical behaviour of the heterogeneous medium in the averaged sense (refer to Figure 3.1). The RVE is assumed to be formed by a solid part and a void part that can include pores and cracks. Models of the present type are described in

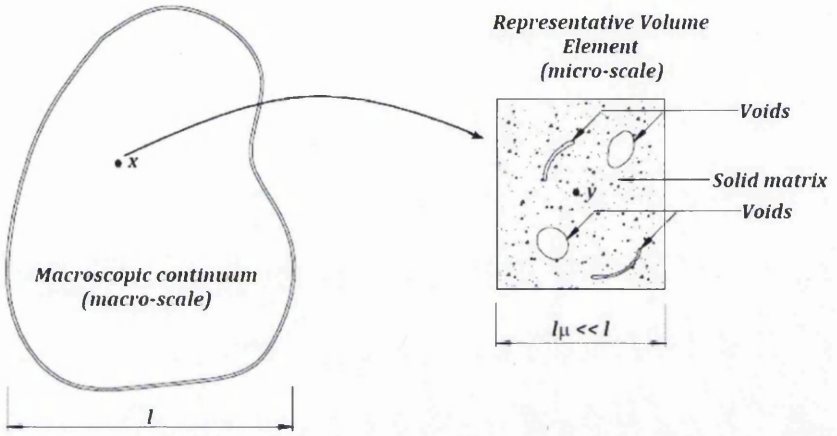

Figure 3.1: Macroscopic continuum and associated local RVE.

further detail, for instance, in Michel et al. (1999) and Pellegrino et al. (1999).

At any instant t, the macroscopic or homogenised strain tensor $\boldsymbol{\varepsilon}$ at a point $\boldsymbol{x}$ of the macro-continuum is assumed to be the volume average of the microscopic strain tensor field $\boldsymbol{\varepsilon}_\mu$ over the domain Ω_μ:

$$\boldsymbol{\varepsilon}(\boldsymbol{x},t) = \frac{1}{V_\mu}\int_{\Omega_\mu} \boldsymbol{\varepsilon}_\mu(\boldsymbol{y},t)\,dV, \tag{3.1}$$

where V_μ is the volume of the RVE associated to point $\boldsymbol{x}$, $\boldsymbol{y}$ denotes the local RVE coordinates and

$$\boldsymbol{\varepsilon}_\mu \equiv \nabla^s \boldsymbol{u}_\mu, \tag{3.2}$$

with ∇^s denoting the symmetric gradient operator and $\boldsymbol{u}_\mu$ the RVE (or microscropic) displacement field.

Further, it is possible to decompose the displacement field $\boldsymbol{u}_\mu$ as a sum of a linear displacement $\boldsymbol{\varepsilon}(\boldsymbol{x},t)\boldsymbol{y}$, which represents a homogeneous strain, and a displacement fluctuation field $\tilde{\boldsymbol{u}}_\mu$, i.e.,

$$\boldsymbol{u}_\mu(\boldsymbol{y},t) = \boldsymbol{\varepsilon}(\boldsymbol{x},t)\boldsymbol{y} + \tilde{\boldsymbol{u}}_\mu(\boldsymbol{y},t). \tag{3.3}$$

The displacement fluctuations field represents local variations about the linear displacement $\boldsymbol{\varepsilon}(\boldsymbol{x},t)\boldsymbol{y}$ and do not contribute to the macroscopic scale strain.

The field $\tilde{\boldsymbol{u}}_\mu$ depends on the presence of heterogeneities within the RVE. Thus, the microscopic strain field can now be defined as,

$$\boldsymbol{\varepsilon}_\mu(\boldsymbol{y},t) = \boldsymbol{\varepsilon}(\boldsymbol{x},t) + \nabla^s \tilde{\boldsymbol{u}}_\mu. \tag{3.4}$$

Analogously to definition (3.1), the macroscopic or homogenised stress tensor field $\boldsymbol{\sigma}$, at a point $\boldsymbol{x}$ of the macro-continuum, is assumed to be the volume average of the microscopic stress tensor $\boldsymbol{\sigma}_\mu$, over Ω_μ:

$$\boldsymbol{\sigma}(\boldsymbol{x},t) = \frac{1}{V_\mu}\int_{\Omega_\mu} \boldsymbol{\sigma}_\mu(\boldsymbol{y},t)\, dV. \tag{3.5}$$

In general, the present multi-scale contitutive theory requires the prescription of kinematical constraints upon the selected RVE. Such constraints define the functional set of kinematically admissible displacement fluctuations – denoted $\mathscr{V}_\mu$ in what follows – which coincides with the corresponding space of virtual kinematically admissible displacements of the RVE (de Souza Neto and Feijóo 2006). Different choices of space $\mathscr{V}_\mu$ lead in general to different constitutive models, such as the widely used affine (or linear) boundary displacement, periodic boundary fluctuations and uniform boundary traction models. Here these three models are considered and the corresponding definitions of $\mathscr{V}_\mu$ will be given later in this Chapter.

Another fundamental concept in multi-scale constitutive theories of the present type is the Hill-Mandel Principle of Macro-homogeneity (Hill (1965); Mandel (1971)), which establishes that the macroscopic stress power must equal the volume average of the microscopic stress power over Ω_μ:

$$\boldsymbol{\sigma} : \dot{\boldsymbol{\varepsilon}} = \frac{1}{V_\mu}\int_{\Omega_\mu} \boldsymbol{\sigma}_\mu : \dot{\boldsymbol{\varepsilon}}_\mu\, dV, \tag{3.6}$$

for any kinematically admissible microscopic strain rate field $\dot{\boldsymbol{\varepsilon}}_\mu$, at any state of the RVE characterised by a microscopic stress field $\boldsymbol{\sigma}_\mu$ in equilibrium.

The Hill-Mandel Principle above requires the RVE body force vector $\boldsymbol{b}$ and external surface traction vector $\boldsymbol{t}^e$ to produce no virtual work (de Souza Neto and Feijóo 2006) – they are purely reactive to the imposed kinematical constraints. That is:

$$\int_{\partial\Omega_\mu} \boldsymbol{t}^e \cdot \boldsymbol{\eta}\, dA = 0\,; \qquad \int_{\Omega_\mu} \boldsymbol{b}\cdot\boldsymbol{\eta}\, dV = 0 \quad \forall \boldsymbol{\eta} \in \mathscr{V}_\mu. \tag{3.7}$$

As a result, the virtual work equilibrium equation for the RVE is reduced to

$$\int_{\Omega_\mu} \boldsymbol{\sigma}_\mu(\boldsymbol{y},t) : \nabla^s \boldsymbol{\eta}\, dV = 0 \quad \forall \boldsymbol{\eta} \in \mathscr{V}_\mu. \tag{3.8}$$

Internal traction forces arising, for instance, from frictional contact on crack surfaces or internal pressure of fluids contained within RVE voids have been ommitted for simplicity in (3.8), but could be included in a straightforward manner.

With the RVE response described by a generic local dissipative constitutive theory, the microscopic stress tensor $\boldsymbol{\sigma}_\mu$ is a functional of the history of $\boldsymbol{\varepsilon}_\mu$. This can be symbolically expressed as

$$\boldsymbol{\sigma}_\mu(\boldsymbol{y},t) = \mathfrak{F}_y(\boldsymbol{\varepsilon}_\mu^t(\boldsymbol{y})), \tag{3.9}$$

where the functional $\mathfrak{F}_y$ associated with point $\boldsymbol{y}$ maps the strain history, $\boldsymbol{\varepsilon}_\mu^t$, up to time t, into the stress $\boldsymbol{\sigma}_\mu$ of time t. In view of the constitutive assumption (3.9), the expression of the virtual work principle in (3.8) leads to

$$\int_{\Omega_\mu} \mathfrak{F}_y\{[\nabla^s \boldsymbol{u}_\mu(\boldsymbol{y},t)]^t\} : \nabla^s \boldsymbol{\eta}\, dV = 0 \quad \forall \boldsymbol{\eta} \in \mathcal{V}_\mu. \tag{3.10}$$

By taking into account Equations (3.2) and (3.4), the above relation can be expressed as

$$G(\boldsymbol{\varepsilon}, \tilde{\boldsymbol{u}}_\mu, \boldsymbol{\eta}) \equiv \int_{\Omega_\mu} \mathfrak{F}_y\{[\boldsymbol{\varepsilon}(\boldsymbol{x},t) + \nabla^s \tilde{\boldsymbol{u}}_\mu(\boldsymbol{y},t)]^t\} : \nabla^s \boldsymbol{\eta}\, dV = 0 \quad \forall \boldsymbol{\eta} \in \mathcal{V}_\mu, \tag{3.11}$$

where we have defined G as virtual work functional. Equation (3.11) defines the *microscopic equilibrium problem* stated as follows: *Given the history of the macroscopic strain tensor $\boldsymbol{\varepsilon} = \boldsymbol{\varepsilon}(\boldsymbol{x},t)$, at a point $\boldsymbol{x}$ of the macro-continuum, find a microscopic displacement fluctuation field $\tilde{\boldsymbol{u}}_\mu \in \mathcal{V}_\mu$, such that for each instant t, Equation* (3.11) *is satisfied.*

3.3 Different types of multi-scale models

In order to complete the formulation presented in the previous section 3.2, a functional space $\mathcal{V}_\mu$ must be specified so as to make problem (3.11) well-posed. Depending on the choice of $\mathcal{V}_\mu$, four multi-scale models can be found typically in the literature. These are:

(i) *Periodic RVE boundary displacement fluctuations model*;

(ii) *The linear RVE boundary displacement model*;

(iii) *The minimum kinematical constraint or uniform RVE boundary traction model*;

(iv) *The Taylor or constant RVE strain model, generally called the rule of mixtures.*

In general, Taylor model provides a poor description of the constitutive response in solid materials. It is a widely known fact that this model does not consider the possible interactions present among phases or those contact forces coming from internal crack surfaces or voids, which may have a crucial impact in the mechanical macroscopic response. It assumes the strain to be homogeneous within the RVE. Consequently, Taylor model will not be further discussed in this work. In the following, we review the kinematical assumptions for the remaining three multi-scale models.

3.3.1 Periodic boundary fluctuations

This is typically associated with the modelling of periodic media. In this particular case, the RVE is a so-called *unit cell* whose periodic repetition generates the entire heterogeneous macro-continuum. Figure 3.2 shows a typical

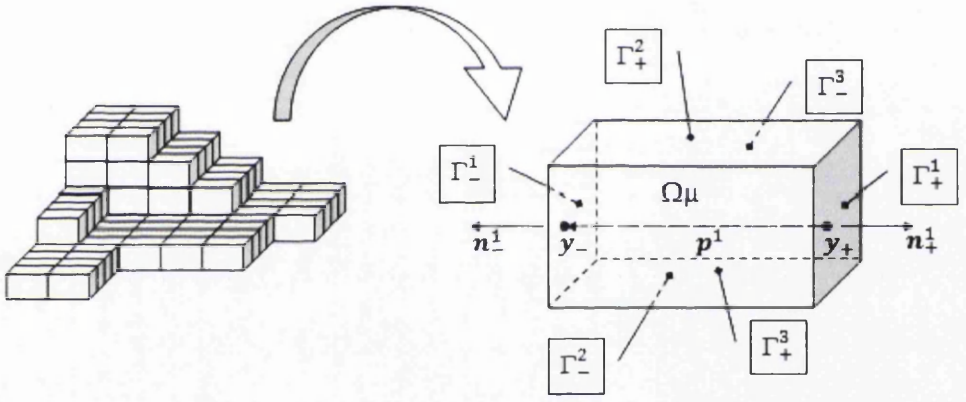

Figure 3.2: Three-dimensional periodic medium represented by parallelepiped-shaped unit cells.

three-dimensional representation of a heterogeneous periodic microstructure, formed by parallelepiped-shaped unit cells. In this case, each pair j of cell sides consists of equally sized subsets Γ_+^j and Γ_-^j of $\partial\Omega_\mu$ with respective unit normal fields $\boldsymbol{n}_+^j$ and $\boldsymbol{n}_-^j$, such that

$$\boldsymbol{n}_+^j = -\boldsymbol{n}_-^j, \tag{3.12}$$

with a one-to-one correspondence between points $\boldsymbol{y}_+$ and $\boldsymbol{y}_-$ belonging respectively to the subsets Γ_+^j and Γ_-^j. The fundamental kinematical assumption which defines the space $\mathcal{V}_\mu$ for this class of constitutive models consists in prescribing identical displacement fluctuation vectors for each pair $\{\boldsymbol{y}_+, \boldsymbol{y}_-\}$ of corresponding points:

$$\tilde{\boldsymbol{u}}_\mu(\boldsymbol{y}_+, t) = \tilde{\boldsymbol{u}}_\mu(\boldsymbol{y}_-, t). \tag{3.13}$$

Note that the one-to-one correspondence between points belonging to a pair j of boundary subsets can be expressed by

$$\boldsymbol{y}_- = \boldsymbol{y}_+ + \boldsymbol{p}^j, \tag{3.14}$$

where $\boldsymbol{p}^j$ are constant vectors associated with the size of the RVE. For this particular model, these vectors are related to the periodicity of the microstructure. Accordingly, the space $\mathcal{V}_\mu$ is defined as

$$\mathcal{V}_\mu = \{\tilde{\boldsymbol{u}}_\mu \text{ sufficiently regular } \mid \tilde{\boldsymbol{u}}_\mu(\boldsymbol{y}_+, t) = \tilde{\boldsymbol{u}}_\mu(\boldsymbol{y}_-, t) \ \forall \text{ pairs } \{\boldsymbol{y}_+, \boldsymbol{y}_-\}\}. \tag{3.15}$$

Additionally, taking into account the orthogonality condition (3.7), the definition of $\mathcal{V}_\mu$ implies that $\boldsymbol{t}^e$ is anti-periodic on $\partial\Omega_\mu$, i.e.,

$$\boldsymbol{t}^e(\boldsymbol{y}^+, t) = -\boldsymbol{t}^e(\boldsymbol{y}^-, t) \quad \forall \ \ pairs\{\boldsymbol{y}^+, \boldsymbol{y}^-\} \in \partial\Omega_\mu. \tag{3.16}$$

In similar form, it is also possible to conclude that the body force vector $\boldsymbol{b}$ is (de Souza Neto and Feijóo 2006):

$$\boldsymbol{b}(\boldsymbol{y}, t) = \boldsymbol{0} \ \ in \ \ \Omega_\mu. \tag{3.17}$$

3.3.2 Linear boundary displacements constraint

For this class of models, the space $\mathcal{V}_\mu$ is defined as

$$\mathcal{V}_\mu = \{\tilde{\boldsymbol{u}}_\mu \text{ sufficiently regular } \mid \tilde{\boldsymbol{u}}_\mu(\boldsymbol{y}, t) = \boldsymbol{0} \ \forall \ \boldsymbol{y} \in \partial\Omega_\mu\}. \tag{3.18}$$

That is, the displacements field along the boundary $\partial\Omega_\mu$ is fully prescribed:

$$\boldsymbol{u}_\mu(\boldsymbol{y}, t) = \boldsymbol{\varepsilon}(\boldsymbol{x}, t)\boldsymbol{y}. \tag{3.19}$$

In this case, the external surface traction, $\boldsymbol{t}^e$, orthogonal to $\mathcal{V}_\mu$ belongs to the space of all sufficiently regular fields over $\partial\Omega_\mu$. Finally, the body force vector $\boldsymbol{b}$ here is, as for the periodic boundary displacement fluctuations model,

$$\boldsymbol{b}(\boldsymbol{y}, t) = \boldsymbol{0} \ \ in \ \ \Omega_\mu. \tag{3.20}$$

3.3.3 Uniform boundary traction or minimal kinematic constraint

This class of models assumes the minimum kinematical constraint of the RVE (de Souza Neto and Feijóo 2006) compatible with the strain averaging (3.1). The corresponding space $\mathcal{V}_\mu$ is given by

$$\mathcal{V}_\mu = \{\tilde{\boldsymbol{u}}_\mu \text{ sufficiently regular } \mid \int_{\partial\Omega_\mu} \tilde{\boldsymbol{u}}_\mu \otimes_s \boldsymbol{n} \, dA = \boldsymbol{0}\}, \tag{3.21}$$

where $\otimes_s$ denotes the symmetric tensor product. The (reactive) tractions on the boundary of the RVE resulting from the present kinematical constraint satisfy (de Souza Neto and Feijóo 2006)

$$\boldsymbol{t}^e(\boldsymbol{y},t) = \boldsymbol{\sigma}_\mu(\boldsymbol{y},t)\,\boldsymbol{n}(\boldsymbol{y}) = \boldsymbol{\sigma}(\boldsymbol{x},t)\,\boldsymbol{n}(\boldsymbol{y}) \;\; \forall\, \boldsymbol{y} \in \partial\Omega_\mu, \tag{3.22}$$

where $\boldsymbol{\sigma}$ is the macroscopic stress. That is, uniform boudary traction fields are the only reactions compatible with the minimum kinematical constraint.

As for the linear and periodic boundary condition models, the above choice of $\mathscr{V}_\mu$ implies $\boldsymbol{b}(\boldsymbol{y},t) = \boldsymbol{0}$ in Ω_μ.

3.4 Finite element approximation

This section describes the numerical approximation of multi-scale constitutive models by means of the Finite Element Method. A generic non-linear implicit finite element discretisation scheme is used as the underlying framework. In what follows, the microscopic constitutive response that characterises the behaviour of the RVE material is assumed to be described within the framework of continuum thermodynamics with internal variables (de Souza Neto et al. 2008, Lemaitre and Chaboche 1990).

The first crucial component of the implicit finite element approximation consists of an incremental (time-discrete) counterpart of the original microscopic constitutive law. In this case, an implicit numerical algorithm is used to discretise the rate constitutive equations of the internal variable-based model. Within a time interval $\Delta t = t_{n+1} - t_n$, with a given initial value $\boldsymbol{\alpha}_n$ for the set of internal variables at time t_n, the microscopic stress tensor $\boldsymbol{\sigma}_\mu|_{n+1}$ at time t_{n+1} is determined by the chosen numerical integration algorithm as a function of the microscopic strain tensor $\boldsymbol{\varepsilon}_\mu|_{n+1}$ at time t_{n+1}. This procedure gives rise to an approximate (generally implicit) incremental constitutive function, $\hat{\boldsymbol{\sigma}}_\mu$, for the stress tensor, such that

$$\boldsymbol{\sigma}_\mu|_{n+1} = \hat{\boldsymbol{\sigma}}_\mu(\boldsymbol{\varepsilon}_\mu|_{n+1}, \Delta t; \boldsymbol{\alpha}_n) = \hat{\boldsymbol{\sigma}}_\mu(\boldsymbol{\varepsilon}_{n+1} + \nabla^s \tilde{\boldsymbol{u}}_\mu|_{n+1}, \Delta t; \boldsymbol{\alpha}_n). \tag{3.23}$$

Equation (3.23) is analogous to a (generally non-linear) elastic constitutive law applicable within the time interval $[t_n, t_{n+1}]$ and may be understood as the discretised counterpart of (3.9).

The next basic ingredient in the finite element approximation to the considered multi-scale models is the incremental counterpart of the microscopic equilibrium problem (3.11). By replacing the time-continuum constitutive functional $\mathfrak{F}_y$ of (3.11) with its time-discrete counterpart $\hat{\boldsymbol{\sigma}}_\mu$ of (3.23), the incremental equilibrium problem of step $n+1$ is obtained:

$$\hat{G}(\boldsymbol{\varepsilon}_{n+1}, \tilde{\boldsymbol{u}}_\mu|_{n+1}, \boldsymbol{\eta}) \equiv \int_{\Omega_\mu} \hat{\boldsymbol{\sigma}}_\mu(\boldsymbol{\varepsilon}_{n+1} + \nabla^s \tilde{\boldsymbol{u}}_\mu|_{n+1}, \Delta t; \alpha_n) : \nabla^s \boldsymbol{\eta}\, dV \qquad \forall \boldsymbol{\eta} \in \mathscr{V}_\mu \tag{3.24}$$

where $\hat{G}$ is the incremental virtual work functional.

Finally, to complete the numerical approximation to the model, a standard finite element discretisation h is introduced in the time-discrete problem (3.24). By replacing the domain Ω_μ with its discrete counterpart Ω_μ^h and the infinite-dimensional functional space $\mathcal{V}_\mu$ with the corresponding finite-dimensional counterpart $\mathcal{V}_\mu^h$ the fully spatial-temporal discretised version of (3.24) is obtained:

$$G^h(\tilde{\mathbf{u}}_\mu|_{n+1}) \equiv \left\{ \int_{\Omega_\mu^h} \mathbf{B}^T \hat{\boldsymbol{\sigma}}_\mu(\boldsymbol{\varepsilon}_{n+1} + \mathbf{B}\tilde{\mathbf{u}}_\mu|_{n+1})\, dV \right\} \cdot \boldsymbol{\eta} = 0 \qquad \forall \boldsymbol{\eta} \in \mathcal{V}_\mu, \tag{3.25}$$

in which $\mathbf{B}$ denotes the global strain-displacement matrix, $\boldsymbol{\varepsilon}_{n+1}$ is the prescribed finite element array of macroscopic engineering strains at time t_{n+1}, $\hat{\boldsymbol{\sigma}}_\mu$ is the incremental constitutive functional at the RVE level that delivers the array of stress components, $\tilde{\mathbf{u}}_\mu|_{n+1}$ is the array of global nodal displacement fluctuations and $\boldsymbol{\eta}$ is the array of global nodal virtual displacements.

Within the present framework, the algebraic equation system (3.25) is solved by the quadratically convergent Newton-Raphson iterative procedure. Then, with a given $\boldsymbol{\varepsilon}_{n+1}$, the following equation system is solved for the iterative correction $\delta\tilde{\mathbf{u}}_\mu^{(k)}$ to the displacement fluctuation during the typical Newton iteration (k):

$$[\mathbf{F}^{(k-1)} + \mathbf{K}^{(k-1)}\delta\tilde{\mathbf{u}}_\mu^{(k)}] \cdot \boldsymbol{\eta} = 0 \qquad \forall \boldsymbol{\eta} \in \mathcal{V}_\mu^h, \tag{3.26}$$

where

$$\mathbf{F}^{(k-1)} \equiv \int_{\Omega_\mu^h} \mathbf{B}^T \hat{\boldsymbol{\sigma}}_\mu(\boldsymbol{\varepsilon}_{n+1} + \mathbf{B}\tilde{\mathbf{u}}_\mu^{(k-1)})\, dV \tag{3.27}$$

is the residual vector, and

$$\mathbf{K}^{(k-1)} \equiv \int_{\Omega_\mu^h} \mathbf{B}^T \mathbf{D}^{(k-1)} \mathbf{B}\, dV \tag{3.28}$$

is the tangent stiffness matrix, with

$$\mathbf{D}^{(k-1)} \equiv \left. \frac{\mathrm{d}\hat{\boldsymbol{\sigma}}_\mu}{\mathrm{d}\boldsymbol{\varepsilon}} \right|_{\boldsymbol{\varepsilon}=\boldsymbol{\varepsilon}_{n+1}+\mathbf{B}\tilde{\mathbf{u}}_\mu^{(k-1)}} \tag{3.29}$$

denoting the consistent tangent operator associated with the numerical algorithm represented by $\hat{\boldsymbol{\sigma}}_\mu$. The new guess $\tilde{\mathbf{u}}_\mu^{(k)}$ for the solution $\tilde{\mathbf{u}}_\mu$ is updated according to

$$\tilde{\mathbf{u}}_\mu^{(k)} = \tilde{\mathbf{u}}_\mu^{(k-1)} + \delta\tilde{\mathbf{u}}_\mu^{(k)}. \tag{3.30}$$

Due to its relevance to one of the main contributions of this thesis, we show in the following some practical details of the actual computer implementation of finite element approximations to the periodic and uniform traction multi-scale models. The implementation of the linear boundary model is omitted due to its standard procedure in general linear solids mechanic problems, requiring no further consideration.

3.4.1 Periodic boundary fluctuations model

At the outset, for convenience, we shall assume the finite element mesh topology here to be such that a one-to-one correspondence exists between nodes of opposing sides of the RVE boundary. In this case, the kinematical constraint (3.13) can be enforced by simply requiring each pair of such nodes to have identical displacement fluctuation. Further, we split the RVE mesh into three subsets of nodes: one set of interior nodes, with corresponding quantities denoted by the subscript i, and; two sets of boundary nodes denoted, respectively, with subscripts $+$ and $-$ so that for each node of set $+$ with coordinate $\boldsymbol{y}_+$ there is a corresponding node of set $-$ with coordinate $\boldsymbol{y}_-$ satisfying (3.14). By taking this partition into account, the discretised space of kinematically admissible nodal displacement fluctuation vectors, $\mathscr{V}_\mu^h$, is defined according to

$$\mathscr{V}_\mu^h = \left\{ \mathbf{v} = \begin{bmatrix} \mathbf{v}_i \\ \mathbf{v}_+ \\ \mathbf{v}_- \end{bmatrix} \;\middle|\; \mathbf{v}_+ = \mathbf{v}_- \right\}. \tag{3.31}$$

By applying the same partition to the components of $\mathbf{F}$, $\mathbf{K}$, $\delta\tilde{\mathbf{u}}_\mu$ and $\boldsymbol{\eta}$, the Newton-Raphson equation (3.26) can be explicitly written as

$$\left\{ \begin{bmatrix} \mathbf{F}_i \\ \mathbf{F}_+ \\ \mathbf{F}_- \end{bmatrix}^{(k-1)} + \begin{bmatrix} \mathbf{k}_{ii} & \mathbf{k}_{i+} & \mathbf{k}_{i-} \\ \mathbf{k}_{+i} & \mathbf{k}_{++} & \mathbf{k}_{+-} \\ \mathbf{k}_{-i} & \mathbf{k}_{-+} & \mathbf{k}_{--} \end{bmatrix}^{(k-1)} \begin{bmatrix} \delta\tilde{\mathbf{u}}_i \\ \delta\tilde{\mathbf{u}}_+ \\ \delta\tilde{\mathbf{u}}_+ \end{bmatrix}^{(k)} \right\} \cdot \begin{Bmatrix} \boldsymbol{\eta}_i \\ \boldsymbol{\eta}_+ \\ \boldsymbol{\eta}_+ \end{Bmatrix} = 0 \quad \forall \boldsymbol{\eta}_i, \boldsymbol{\eta}_+ \tag{3.32}$$

Straightforward algebraic operations on the above equation yields

$$\left\{ \begin{bmatrix} \mathbf{F}_i \\ \mathbf{F}_+ + \mathbf{F}_- \end{bmatrix}^{(k-1)} + \begin{bmatrix} \mathbf{k}_{ii} & \mathbf{k}_{i+} + \mathbf{k}_{i-} \\ \mathbf{k}_{+i} + \mathbf{k}_{-i} & \mathbf{k}_{++} + \mathbf{k}_{+-} + \mathbf{k}_{-+} + \mathbf{k}_{--} \end{bmatrix}^{(k-1)} \begin{bmatrix} \delta\tilde{\mathbf{u}}_i \\ \delta\tilde{\mathbf{u}}_+ \end{bmatrix}^{(k)} \right\} \cdot \begin{Bmatrix} \boldsymbol{\eta}_i \\ \boldsymbol{\eta}_+ \end{Bmatrix} = 0 \quad \forall \boldsymbol{\eta}_i, \boldsymbol{\eta}_+, \tag{3.33}$$

which, in view of the arbitrariness of $\boldsymbol{\eta}_i$ and $\boldsymbol{\eta}_+$, leads to the reduced form

$$\begin{bmatrix} \mathbf{k}_{ii} & \mathbf{k}_{i+} + \mathbf{k}_{i-} \\ \mathbf{k}_{+i} + \mathbf{k}_{-i} & \mathbf{k}_{++} + \mathbf{k}_{+-} + \mathbf{k}_{-+} + \mathbf{k}_{--} \end{bmatrix}^{(k-1)} \begin{bmatrix} \delta\tilde{\mathbf{u}}_i \\ \delta\tilde{\mathbf{u}}_+ \end{bmatrix}^{(k)} = - \begin{bmatrix} \mathbf{F}_i \\ \mathbf{F}_+ + \mathbf{F}_- \end{bmatrix}^{(k-1)}. \tag{3.34}$$

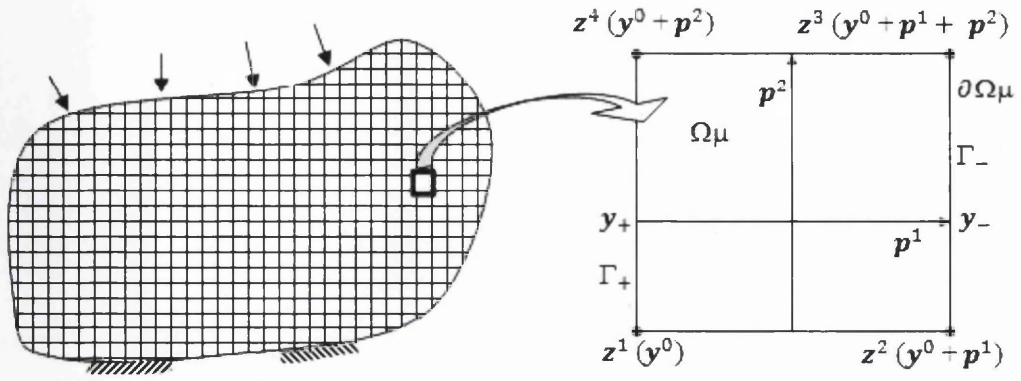

Figure 3.3: On the left, division of periodic medium into rectangular unit cells. On the right, a repeating unit cell with zero fluctuations in the corners and one-to-one correspondence between opposite sides of the cell.

In what follows, and for simplicity, our presentation will focus on two-dimensional models. However, its application to the three-dimensional case is straightforward. Without loss of generality, any periodic medium can be represented as an array of rectangular unit cells (refer to Figure 3.3).

Accordingly, if the lower left corner of the RVE has coordinate $\boldsymbol{y}^0$, the coordinates of the remaining three corners are defined from (3.14) as $\boldsymbol{y}^0+\boldsymbol{p}^1$, $\boldsymbol{y}^0+\boldsymbol{p}^2$ and $\boldsymbol{y}^0+\boldsymbol{p}^1+\boldsymbol{p}^2$, with $\boldsymbol{p}^1$ and $\boldsymbol{p}^2$ denoting the vectors defined in (3.14) and illustrated in Figure 3.3. If the fluctuation displacement $\tilde{\boldsymbol{u}}_\mu$ at point $\boldsymbol{y}^0$ is known, then according to relationships (3.13) and (3.14) the fluctuation is also known at these three additional points of the boundary. These four points define and delimit the domain Ω_μ of the rectangular base cell.

To eliminate rigid body motions, the lower left corner $\boldsymbol{y}^0$ of the cell is assigned a prescribed zero displacement fluctuation and, as a result, the fluctuation $\tilde{\boldsymbol{u}}_\mu$ at the remaining three corners is equally set to zero:

$$\tilde{\boldsymbol{u}}_\mu(\boldsymbol{y}^0) = \tilde{\boldsymbol{u}}_\mu(\boldsymbol{y}^0+\boldsymbol{p}^1) = \tilde{\boldsymbol{u}}_\mu(\boldsymbol{y}^0+\boldsymbol{p}^1+\boldsymbol{p}^2) = \tilde{\boldsymbol{u}}_\mu(\boldsymbol{y}^0+\boldsymbol{p}^2) = \boldsymbol{0}, \qquad (3.35)$$

where, for simplicity, the argument t has been omitted in function $\tilde{\boldsymbol{u}}_\mu$. Nodes with zero prescribed fluctuations are denoted $\boldsymbol{z}^1,\cdots,\boldsymbol{z}^n$ in the figures (see nodes $\boldsymbol{z}^1$–$\boldsymbol{z}^4$ in Figure 3.3). Having defined such nodes, the solution of the Newton-Raphson equation (3.34) can be undertaken in the usual fashion after removing the corresponding prescribed degrees of freedom from the system.

3.4.2 Uniform boundary traction model

A direct discretisation of definition (3.21) gives the discretised version of the minimally constrained vector space of kinematically admissible displacement

fluctuations field, $\mathcal{V}_\mu^h$, expressed as

$$\mathcal{V}_\mu^h = \left\{ \mathbf{v} = \begin{bmatrix} \mathbf{v}_i \\ \mathbf{v}_b \end{bmatrix} \mid \int_{\partial\Omega_\mu^h} \mathbf{N}_b \mathbf{v}_b \otimes_s \mathbf{n}\, dA = \mathbf{0} \right\}, \tag{3.36}$$

where $\mathbf{v}_i$ and $\mathbf{v}_b$ are the nodal displacement fluctuation vectors for the set of interior nodes and for the set of boundary nodes (denoted by subscript b), respectively, and $\mathbf{N}_b$ is the matrix of shape functions of the elements sharing the boundary $\partial\Omega_\mu^h$ of the discretised RVE.

The above discretised (linear) kinematical constraint (3.36) may be rewritten in a compact form as

$$\mathbf{C}\, \mathbf{v}_b = \mathbf{0}, \tag{3.37}$$

where $\mathbf{C}$ is the *constraint matrix* which takes into account the dependency of three or six arbitrary degrees of freedom (in two or three dimensions, respectively) on the discretised boundary $\partial\Omega_\mu^h$ respect to the remaining boundary degrees of freedom of the RVE.

By partitioning the set of boundary degrees of freedom into three subsets: *free*, *dependent* and *prescribed*, denoted respectively with subscripts f, d and p, Equation (3.37) can be written as

$$\begin{bmatrix} \mathbf{C}_f & \mathbf{C}_d & \mathbf{C}_p \end{bmatrix} \begin{bmatrix} \mathbf{v}_f \\ \mathbf{v}_d \\ \mathbf{v}_p \end{bmatrix} = \mathbf{0}. \tag{3.38}$$

By assigning zero displacement fluctuations to the prescribed set, $\mathbf{v}_p = \mathbf{0}$, to eliminate rigid body motions, Equation (3.38) reduces to

$$\mathbf{v}_d = \mathbf{R}\mathbf{v}_f, \tag{3.39}$$

where

$$\mathbf{R} = -\mathbf{C}_d^{-1}\, \mathbf{C}_f. \tag{3.40}$$

Finally, by taking the above into account we arrive after straightforward manipulations at the Newton-Raphson correction formula for the present model:

$$\begin{bmatrix} \mathbf{k}_{ii} & \mathbf{k}_{if} + \mathbf{k}_{id}\mathbf{R} \\ \mathbf{k}_{fi} + \mathbf{R}^T\mathbf{k}_{di} & \mathbf{k}_{ff} + \mathbf{k}_{fd}\mathbf{R} + \mathbf{R}^T\mathbf{k}_{df} + \mathbf{R}^T\mathbf{k}_{dd}\mathbf{R} \end{bmatrix}^{(k-1)} \begin{bmatrix} \delta\tilde{\mathbf{u}}_i \\ \delta\tilde{\mathbf{u}}_f \end{bmatrix}^{(k)} = - \begin{bmatrix} \mathbf{F}_i \\ \mathbf{F}_f + \mathbf{R}^T\mathbf{F}_d \end{bmatrix}^{(k-1)}. \tag{3.41}$$

In what follows, the axiomatic variational framework presented up to here is extended to the description of a family of large strain multi-scale constitutive theories.

3.5 Large strain formulation

The main assumption in this family of large strain multi-scale constitutive theory presented here is that the deformation gradient $\boldsymbol{F}$ at any arbitrary point $\boldsymbol{x}$ of the macroscopic continuum is the volume average of the microscopic deformation gradient field $\boldsymbol{F}_\mu$ defined over the local RVE. Similarly to (3.1), at any instant t, the macroscopic or homogenised deformation gradient $\boldsymbol{F}$ at a point $\boldsymbol{x}$ can be expressed as

$$\boldsymbol{F}(\boldsymbol{x},t) = \frac{1}{V_\mu}\int_{\Omega_\mu} \boldsymbol{F}_\mu(\boldsymbol{y},t)\, dV, = \boldsymbol{I} + \frac{1}{V_\mu}\int_{\Omega_\mu} \nabla \boldsymbol{u}_\mu\, dV, \tag{3.42}$$

where V_μ and Ω_μ are the volume of the RVE and its domain, respectively, in their *reference* configuration. Here, $\boldsymbol{I}$ denotes the second order identity tensor, ∇ the material gradient operator (with respect to the *reference* coordinates), and $\boldsymbol{u}_\mu$ and $\boldsymbol{y}$ as defined in Section 3.2.

Further, it is possible to decompose the displacement field $\boldsymbol{u}_\mu$ as a sum of a linear displacement $(\boldsymbol{F}(\boldsymbol{x},t) - \boldsymbol{I})\boldsymbol{y}$ and a displacement fluctuation field $\tilde{\boldsymbol{u}}_\mu$, i.e.,

$$\boldsymbol{u}_\mu(\boldsymbol{y},t) = (\boldsymbol{F}(\boldsymbol{x},t) - \boldsymbol{I})\boldsymbol{y} + \tilde{\boldsymbol{u}}_\mu(\boldsymbol{y},t). \tag{3.43}$$

In addition, analogously to definition (3.42), the macroscopic or homogenised first Piola-Kirchoff stress tensor field $\boldsymbol{P}$, at a point $\boldsymbol{x}$ of the macrocontinuum, is assumed to be the volume average of the microscopic first Piola-Kirchoff stress tensor $\boldsymbol{P}_\mu$, over Ω_μ:

$$\boldsymbol{P}(\boldsymbol{x},t) = \frac{1}{V_\mu}\int_{\Omega_\mu} \boldsymbol{P}_\mu(\boldsymbol{y},t)\, dV. \tag{3.44}$$

Following the context of large strains, the Hill-Mandel Principle of Macrohomogeneity establishes that the macroscopic stress power must equal the volume average of the microscopic stress power over Ω_μ for any kinematically admissible microscopic deformation gradient rate field $\dot{\boldsymbol{F}}_\mu$, at any state of the RVE in equilibrium. It can be expressed as

$$\boldsymbol{P} : \dot{\boldsymbol{F}} = \frac{1}{V_\mu}\int_{\Omega_\mu} \boldsymbol{P}_\mu : \dot{\boldsymbol{F}}_\mu\, dV. \tag{3.45}$$

Similarly to (3.7), the Hill-Mandel Principle above requires the RVE body force vector per unit *reference* volume and external surface traction vector measured per unit *reference* area to produce no virtual work. As a result, and

ignoring contact stresses or internal pressure of fluids contained in the RVE, the virtual work equilibrium equation for the RVE is reduced to

$$\int_{\Omega_\mu} \boldsymbol{P}_\mu(\boldsymbol{y},t) : \nabla\boldsymbol{\eta}\, dV = 0 \qquad \forall \boldsymbol{\eta} \in \mathcal{V}_\mu. \tag{3.46}$$

To complete the large strain continuum formulation, the functional space $\mathcal{V}_\mu$ is specified following the same description given in Section 3.3, requiring no further discussion.

The computational implementation of the above finite strain multi-scale constitutive theory follows the same steps described in Section 3.4, for the corresponding small strains counterpart.

By introducing a numerical approximation, resulting from time-discretisation at the micro-scale, the approximate incremental microscopic constitutive function, $\hat{\boldsymbol{P}}_\mu$, for a time interval $[t_n, t_{n+1}]$, becomes

$$\boldsymbol{P}_\mu|_{n+1} = \hat{\boldsymbol{P}}_\mu(\boldsymbol{F}_\mu|_{n+1}, \Delta t; \boldsymbol{\alpha}_n) = \hat{\boldsymbol{P}}_\mu(\boldsymbol{F}_{n+1} + \nabla\tilde{\boldsymbol{u}}_\mu|_{n+1}, \Delta t; \boldsymbol{\alpha}_n), \tag{3.47}$$

with Δt and $\boldsymbol{\alpha}_n$ representing the increment of time and the microscopic internal variable field, as defined in Section 3.4. Consequently, the discretised counterpart of the macroscopic first Piola kirchhoff stress tensor can be computed:

$$\boldsymbol{P}_{n+1} = \frac{1}{V_\mu}\int_{\Omega_\mu} \hat{\boldsymbol{P}}_\mu(\boldsymbol{F}_{n+1} + \nabla\tilde{\boldsymbol{u}}_\mu|_{n+1}, \Delta t; \alpha_n)\, dV. \tag{3.48}$$

Similarly, the RVE incremental equilibrium problem can be expressed as

$$\int_{\Omega_\mu} \hat{\boldsymbol{P}}_\mu(\boldsymbol{F}_{n+1} + \nabla\tilde{\boldsymbol{u}}_\mu|_{n+1}, \Delta t; \alpha_n) : \nabla\boldsymbol{\eta}\, dV \;\; = 0 \quad \forall \boldsymbol{\eta} \in \mathcal{V}_\mu, \tag{3.49}$$

which consists in finding a kinematically admissible displacement fluctuations field $\tilde{\boldsymbol{u}}_\mu|_{n+1} \in \mathcal{V}_\mu$, for a given macroscopic deformation gradient, $\boldsymbol{F}_{n+1}$, and microscopic internal variable field, α_n, such that relation (3.49) is satisfied.

Lastly, to complete the numerical approximation to the present finite strain multi-scale model, a standard finite element discretisation h is introduced in (3.49). By replacing the domain Ω_μ with its discrete counterpart Ω_μ^h and the infinite-dimensional functional space $\mathcal{V}_\mu$ with the corresponding finite-dimensional counterpart $\mathcal{V}_\mu^h$, the fully spatial-temporal discretised version of (3.49) is obtained:

$$\left\{\int_{\Omega_\mu^h} \mathbf{B}^T\hat{\mathbf{P}}_\mu(\mathbf{F}_{n+1} + \mathbf{B}\tilde{\mathbf{u}}_\mu|_{n+1})\, dV\right\} \cdot \boldsymbol{\eta} = 0 \qquad \forall \boldsymbol{\eta} \in \mathcal{V}_\mu^h, \tag{3.50}$$

in which $\mathbf{B}$ denotes the global discrete gradient matrix containing the appropriate shape function derivatives, $\mathbf{F}_{n+1}$ is the array of macroscopic deformation gradient components at time t_{n+1}, $\hat{\mathbf{P}}_\mu$ is the incremental constitutive functional at the RVE level that delivers the array of First Piola-Kirchhoff stress components, $\tilde{\mathbf{u}}_\mu|_{n+1}$ is the array of global nodal displacement fluctuations and $\boldsymbol{\eta}$ is the array of global nodal virtual displacements.

Finally, Equation (3.50) together with the finite element-discrete version of (3.48) define the fully discretised multi-scale constitutive model. The discretisation of the different kinematical constraints coincides with that described in the preceding section and therefore, it is omitted here.

As shall be seen in Chapter 4, one important point in the present work will be the consideration of implicit symmetries present commonly in microstructures, in order to reduce computer times and memory requirements.

CHAPTER 4

Symmetry conditions

4.1 Introduction

In this chapter, we explore the consequences of further symmetry conditions that arise often in the modelling of microstructures. What we show here is that, in many circumstances of practical interest, when the RVE possesses special symmetries, very simple considerations can lead to substantial savings in computing times in the solution of the microscopic equilibrium problem. The obvious benefits of such savings become particularly pronounced in coupled two-scale simulations, where the macroscopic equilibrium problem is solved simultaneously with (possibly) a large number of microscopic equilibrium problems at Gauss-point level (Matsui et al. 2004). The computational effort put in the solution of the RVE equilibrium problem is directly related to the number of degrees of freedom of the discretised RVE domain. In this context, the presence of additional symmetries may allow the choice of RVEs with domain comprising only a symmetric portion of the generic domain considered in the above. Whenever such conditions are met, substantial reductions in computational costs associated with CPU time and storage requirements may be achieved. In particular, these will be useful in the treatment of wood cell wall.

The two types of RVE symmetry explored here – staggered-translational and point symmetry – are present in a large number of examples reported in the literature (Michel et al. 1999, Pellegrino et al. 1999, Matsui et al. 2004, Giusti, Blanco, de Souza Neto and Feijóo 2009, Somer et al. 2009), but unfortunately have not been exploited to reduce the size of the RVE equilibrium problem. Nevertheless, the use of symmetry considerations for computing time reductions in this context has been originally considered by Ohno et al. (2001), but limited to the analysis of periodic media (with the corresponding periodicity kinematical assumption). Here we extend their analysis by considering in addition the other two classes of models – linear boundary displacements and uniform boundary traction.

In what follows, for the sake of clarity we will keep our explanation restricted to two-dimensional problems under infinitesimal strains. However, at the end of this chapter, some numerical examples will be given, for both two and three dimensions, under small and finite strains regime. We refer here to Saavedra Flores and de Souza Neto (2010).

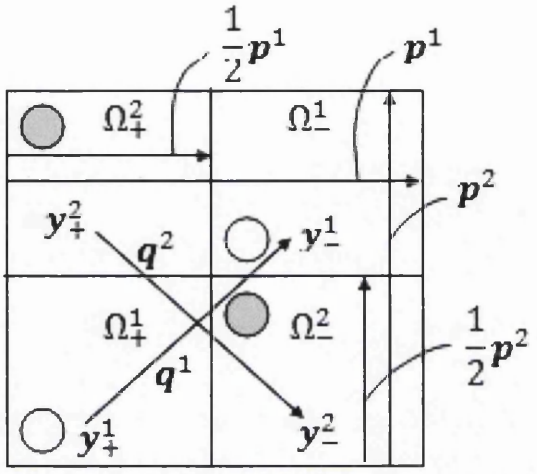

Figure 4.1: Example of unit cell where staggered-translational symmetry is present. Constant vectors $\boldsymbol{q}^j$ link different points in the domain that satisfy Equation (4.4)

4.2 Staggered-translational symmetry

Here we shall say that *staggered-translational symmetry* is met if the original RVE may be split into four non-overlapping subdomains (refer to Figure 4.1):

$$\Omega_\mu = \Omega_+^1 \cup \Omega_-^1 \cup \Omega_+^2 \cup \Omega_-^2 \tag{4.1}$$

with the material properties *and* kinematical constraints at any point $\boldsymbol{y}_+^j \in \Omega_+^j$ being identical to those of the corresponding point $\boldsymbol{y}_-^j \in \Omega_-^j$, related to $\boldsymbol{y}_+^j$ by the staggered-translational mapping

$$\boldsymbol{y}_-^j = \boldsymbol{y}_+^j + \boldsymbol{q}^j. \tag{4.2}$$

The constant vectors $\boldsymbol{q}^j$ are

$$\boldsymbol{q}^1 = \tfrac{1}{2}(\boldsymbol{p}^1 + \boldsymbol{p}^2), \qquad \boldsymbol{q}^2 = \tfrac{1}{2}(\boldsymbol{p}^1 - \boldsymbol{p}^2), \tag{4.3}$$

where $\boldsymbol{p}^j$ are the vectors given in (3.14). It is emphasised here that in the general case, these vectors are determined by the size of the RVE (Figure 4.1) but in the particular case of the periodic boundary fluctuations model, vectors $\boldsymbol{p}^j$ coincide with those that define the periodicity of the RVE. For the general case, the following relation holds:

$$\tilde{\boldsymbol{u}}_\mu(\boldsymbol{y}_+^j, t) = \tilde{\boldsymbol{u}}_\mu(\boldsymbol{y}_-^j, t), \tag{4.4}$$

so that the knowledge of the displacement fluctuation field over, say, ${}^{1/2}\Omega_\mu \equiv \Omega_+^1 \cup \Omega_+^2$ is sufficient to determine $\tilde{\boldsymbol{u}}_\mu$ over the entire domain Ω_μ. This allows

the finite element approximation to the multi-scale constitutive model to be made by discretising only the half-domain ${}^{1/2}\Omega_\mu$ with appropriate symmetry conditions imposed on its boundary $\partial^{1/2}\Omega_\mu$.

We remark that symmetry relation (4.4) is not satisfied in general when the linear boundary displacement or the minimum constraint models are considered. That is, a staggered-translational symmetric medium (with pairs of points related by (4.2) having identical mechanical properties) will not in general have staggered-translational kinematics under such constraints. Thus, the implementation of this type of symmetry will be addressed only for the periodic boundary fluctuations model.

4.2.1 Periodic boundary displacement fluctuations model

With the lower left corner of the original RVE (Figure 4.2(a)) having zero prescribed fluctuation, (4.4) implies that

$$\tilde{\boldsymbol{u}}_\mu(\boldsymbol{y}^0, t) = \tilde{\boldsymbol{u}}_\mu(\boldsymbol{y}^0 + \boldsymbol{q}^1, t) = \mathbf{0}, \tag{4.5}$$

i.e., the displacement fluctuation at the centre of the original RVE (point $\boldsymbol{z}^5$) is zero. Further use of (4.4) allows the RVE to be re-defined as the half-domain ${}^{1/2}\Omega_\mu$ with its boundary $\partial^{1/2}\Omega_\mu$ split into three pairs of subsets $\{{}^{1/2}\Gamma^j_+, {}^{1/2}\Gamma^j_-\}$ (refer to Figure 4.2(b)) and the direct enforcement of identical fluctuations for corresponding pairs of boundary points follows the same procedure as that described for the original (full) RVE. Then, similarly to (3.31), the space $\tilde{\mathscr{V}}^h_\mu$ for the discretised reduced RVE, with domain ${}^{1/2}\Omega^h_\mu$, is here defined as

$$\tilde{\mathscr{K}}^h_\mu = \left\{ \mathbf{v} = \begin{bmatrix} \mathbf{v}_i \\ \mathbf{v}_+ \\ \mathbf{v}_- \\ \mathbf{v}_{o_1} \\ \mathbf{v}_{o_2} \\ \mathbf{v}_{o_3} \end{bmatrix} \;\middle|\; \mathbf{v}_+ = \mathbf{v}_- \;;\; \mathbf{v}_{o_1} = \mathbf{v}_{o_2} = \mathbf{v}_{o_3} \right\}, \tag{4.6}$$

where $\mathbf{v}_i$, $\mathbf{v}_+$ and $\mathbf{v}_-$ have been defined in (3.31) and vectors $\mathbf{v}_{o_1}$, $\mathbf{v}_{o_2}$ and $\mathbf{v}_{o_3}$ are the nodal displacement fluctuations at points o_1, o_2 and o_3 of Figure 4.2(b), respectively. The prescription of identical fluctuations for the set $\{\mathbf{v}_{o_1}, \mathbf{v}_{o_2}, \mathbf{v}_{o_3}\}$ of nodal vectors follows directly from (4.4), but since unlike the standard case this set does not form a pair, the corresponding constraint has been made explicit in definition (4.6).

Following the same procedure as that of the previous chapter, we obtain,

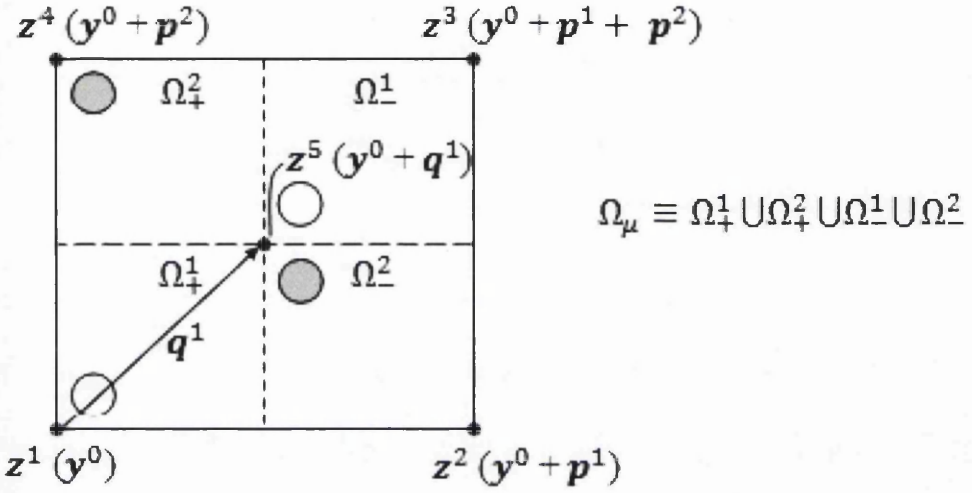

(a) Original domain Ω_μ.

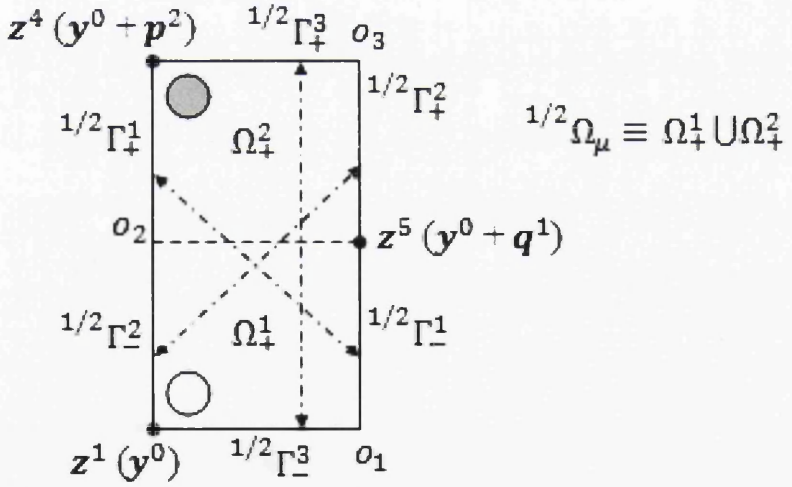

(b) Half-domain, $^{1/2}\Omega_\mu$. Arrows indicate one-to-one correspondence.

Figure 4.2: Reduction of the original RVE into a half-domain when staggered-translational symmetry is present. Figures show zero-fluctuation points highlighted with black points for Ω_μ and $^{1/2}\Omega_\mu$, respectively.

after straightforward manipulations,

$$\begin{bmatrix} \mathbf{k}_{ii} & \mathbf{k}_{i+}+\mathbf{k}_{i-} \\ \mathbf{k}_{+i}+\mathbf{k}_{-i} & \mathbf{k}_{++}+\mathbf{k}_{+-}+\mathbf{k}_{-+}+\mathbf{k}_{--} \\ \mathbf{k}_{o_1 i}+\mathbf{k}_{o_2 i}+\mathbf{k}_{o_3 i} & \mathbf{k}_{o_1+}+\mathbf{k}_{o_1-}+\mathbf{k}_{o_2+}+\mathbf{k}_{o_2-}+\mathbf{k}_{o_3+}+\mathbf{k}_{o_3-} \end{bmatrix}$$

$$\begin{bmatrix} \mathbf{k}_{io_1}+\mathbf{k}_{io_2}+\mathbf{k}_{io_3} \\ \mathbf{k}_{+o_1}+\mathbf{k}_{+o_2}+\mathbf{k}_{+o_3}+\mathbf{k}_{-o_1}+\mathbf{k}_{-o_2}+\mathbf{k}_{-o_3} \\ \mathbf{k}_{o_1o_1}+\mathbf{k}_{o_1o_2}+\mathbf{k}_{o_1o_3}+\mathbf{k}_{o_2o_1}+\mathbf{k}_{o_2o_2}+\mathbf{k}_{o_2o_3}+\mathbf{k}_{o_3o_1}+\mathbf{k}_{o_3o_2}+\mathbf{k}_{o_3o_3} \end{bmatrix}^{(k-1)} \begin{bmatrix} \delta\tilde{\mathbf{u}}_i \\ \delta\tilde{\mathbf{u}}_+ \\ \delta\tilde{\mathbf{u}}_{o_1} \end{bmatrix}^{(k)}$$

$$= - \begin{bmatrix} \mathbf{F}_i \\ \mathbf{F}_+ + \mathbf{F}_- \\ \mathbf{F}_{o_1} + \mathbf{F}_{o_2} + \mathbf{F}_{o_3} \end{bmatrix}^{(k-1)} . \tag{4.7}$$

In summary, straightforward symmetry considerations in the present case allowed a significant reduction in the number of unknowns by using a reduced RVE domain, comprising only one half of the domain adopted in the original problem whose system of linearised finite element equations is given in (3.34). As we shall see in the numerical examples presented later, this results in substantial reductions in computational costs for analyses involving RVEs with staggered-translational symmetry.

4.3 Point symmetry

In two-dimensional problems, point symmetry is defined by the invariance of the RVE material properties *and* kinematical constraints to rotations of 180°. This is illustrated in Figure 4.3, where the original configuration, $\mathscr{C}$, of the RVE coincides with the configuration $\mathscr{C}'$ obtained by rotating $\mathscr{C}$ by 180°. We start by observing that the Cartesian components of a second-order tensor are invariant to changes of basis comprising a 180° rotation. Then consider the coordinate systems defined by the basis vectors $\{\boldsymbol{e}_1, \boldsymbol{e}_2\}$ and $\{\boldsymbol{e}'_1, \boldsymbol{e}'_2\}$ differing by a rotation of 180° (see Figure 4.3). Without loss of generality, we assume the origin of the two systems to be located at the centre of the RVE. The invariance of second-order tensors implies that any imposed macroscopic strain will have the same representation in both coordinate systems. This, combined with the assumed symmetry of material properties and kinematical constraints, requires the equilibrium problem to have identical representation in both systems. As a result, any fluctuation field satisfies

$$\tilde{\boldsymbol{u}}_\mu(\boldsymbol{y}_\oplus, t) = -\tilde{\boldsymbol{u}}_\mu(\boldsymbol{y}_\ominus, t) \tag{4.8}$$

for any pairs $\{\boldsymbol{y}_\oplus, \boldsymbol{y}_\ominus\}$ of points of Ω_μ such that

$$\boldsymbol{y}_\oplus = -\boldsymbol{y}_\ominus. \tag{4.9}$$

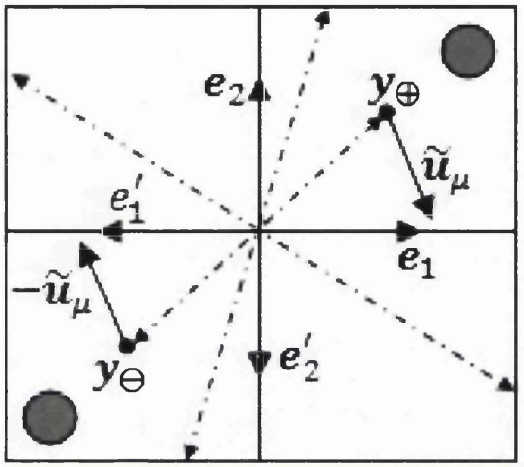

Figure 4.3: Typical RVE with point symmetry.

In the following, the numerical implementation taking advantage of point symmetry is detailed for the three classes of multi-scale models considered here.

4.3.1 Periodic boundary displacement fluctuations model

Due to the point symmetry conditions (see Figure 4.4(a)), points z^6 and z^8 of $\partial\Omega_\mu$ satisfy condition (3.13) satisfy condition (3.13) and (4.8) simultaneously. The same applies to points z_5, z_7 and z_9. Hence, we have

$$\tilde{u}_\mu(z^5,t) = \tilde{u}_\mu(z^6,t) = \tilde{u}_\mu(z^7,t) = \tilde{u}_\mu(z^8,t) = \tilde{u}_\mu(z^9,t) = \mathbf{0}. \qquad (4.10)$$

In addition, again as a consequence of (3.13) and (4.8), the displacement fluctuation field along the side of the micro-cell defined by points z^4 and z^3 satisfies a point symmetry about point z^8. The same type of displacement fluctuation symmetry is observed along the lines z^1-z^2, z^1-z^4, z^2-z^3, z^6-z^8 and z^9-z^7, as shown by Figure 4.4(a). Similarly to the staggered-translational symmetry case, the present point symmetry allows the domain of analysis to be reduced to one symmetric half, ${}^{1/2}\Omega_\mu$, of the original domain Ω_μ. The reduced RVE domain is shown in Figure 4.4(b). The boundary $\partial^{1/2}\Omega_\mu$ here can be conveniently split into three pairs of subsets, $\{\Gamma^1_+, \Gamma^1_-\}$, $\{\Gamma^2_\oplus, \Gamma^2_\ominus\}$ and $\{\Gamma^3_\oplus, \Gamma^3_\ominus\}$. The original constraint (3.13) holds for pair $\{\Gamma^1_+, \Gamma^1_-\}$. For pairs

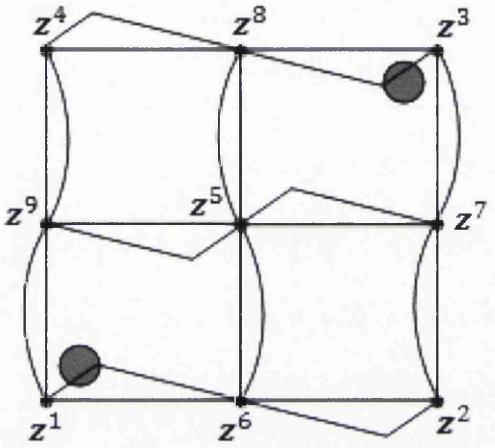

(a) Displacement fluctuations variation and zero-values.

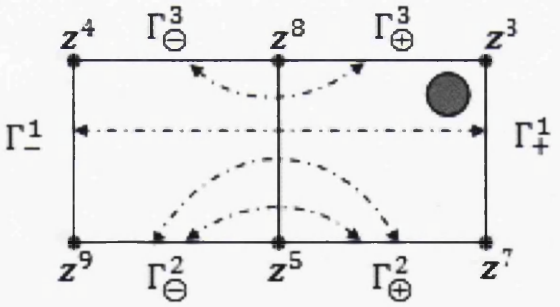

(b) One-to-one correspondence between points on $^{1/2}\partial\Omega_\mu$

Figure 4.4: Point symmetry

$\{\Gamma^2_\oplus, \Gamma^2_\ominus\}$ and $\{\Gamma^3_\oplus, \Gamma^3_\ominus\}$, constraint (4.8) applies instead. To write the corresponding equilibrium equations, we use the definitions

$$\{\Gamma_+, \Gamma_-\} \equiv \{\Gamma^1_+, \Gamma^1_-\}, \qquad \{\Gamma_\oplus, \Gamma_\ominus\} \equiv \{\Gamma^2_\oplus \cup \Gamma^3_\oplus, \Gamma^2_\ominus \cup \Gamma^3_\ominus\}. \tag{4.11}$$

Accordingly, on the discretised half-domain ${}^{1/2}\Omega^h_\mu$, the space $\tilde{\mathscr{K}}^h_\mu$ of kinematically admissible nodal displacement fluctuation vectors is defined as

$$\tilde{\mathscr{K}}^h_\mu = \left\{ \mathbf{v} = \begin{bmatrix} \mathbf{v}_i \\ \mathbf{v}_+ \\ \mathbf{v}_- \\ \mathbf{v}_\oplus \\ \mathbf{v}_\ominus \end{bmatrix} \;\middle|\; \mathbf{v}_+ = \mathbf{v}_- \;\; ; \;\; \mathbf{v}_\oplus = -\mathbf{v}_\ominus \right\}. \tag{4.12}$$

Note that the one-to-one correspondence between nodes of $\{\Gamma^1_+, \Gamma^1_-\}$ follows the rule of (3.14). For the pairs $\{\Gamma^2_\oplus, \Gamma^2_\ominus\}$ and $\{\Gamma^3_\oplus, \Gamma^3_\ominus\}$ the one-to-one nodal correspondence satisfies the rotational symmetry about $\boldsymbol{z}^5$ about $\boldsymbol{z}^8$, respectively.

Finally, by following the same procedure as that leading to (3.34) and (4.7), the reduced linearised equilibrium equation here is obtained as

$$\begin{bmatrix} \mathbf{k}_{ii} & \mathbf{k}_{i+} + \mathbf{k}_{i-} & \mathbf{k}_{i\oplus} - \mathbf{k}_{i\ominus} \\ \mathbf{k}_{+i} + \mathbf{k}_{-i} & \mathbf{k}_{++} + \mathbf{k}_{+-} + \mathbf{k}_{-+} + \mathbf{k}_{--} & \mathbf{k}_{+\oplus} - \mathbf{k}_{+\ominus} + \mathbf{k}_{-\oplus} - \mathbf{k}_{-\ominus} \\ \mathbf{k}_{\oplus i} - \mathbf{k}_{\ominus i} & \mathbf{k}_{\oplus+} + \mathbf{k}_{\oplus-} - \mathbf{k}_{\ominus+} - \mathbf{k}_{\ominus-} & \mathbf{k}_{\oplus\oplus} - \mathbf{k}_{\oplus\ominus} - \mathbf{k}_{\ominus\oplus} + \mathbf{k}_{\ominus\ominus} \end{bmatrix}^{(k-1)}$$

$$\cdot \begin{bmatrix} \delta\tilde{\mathbf{u}}_i \\ \delta\tilde{\mathbf{u}}_+ \\ \delta\tilde{\mathbf{u}}_\oplus \end{bmatrix}^{(k)} = - \begin{bmatrix} \mathbf{F}_i \\ \mathbf{F}_+ + \mathbf{F}_- \\ \mathbf{F}_\oplus - \mathbf{F}_\ominus \end{bmatrix}^{(k-1)}. \tag{4.13}$$

4.3.2 Linear boundary displacement model

Under the linear boundary displacement constraint, point symmetry is also preserved for RVEs whose material properties satisfy 180° rotations symmetry. Hence, in this case the domain of analysis can also be reduced to one symmetric half ${}^{1/2}\Omega_\mu$. Figure 4.5 shows the reduced domain with the corresponding boundary constraints. For the purpose of computer implementation, the boundary $\partial^{1/2}\Omega_\mu$ is conveniently split into a subset $\Gamma_0 \equiv \Gamma^1_0 \cup \Gamma^2_0 \cup \Gamma^3_0$, and a pair of subsets $\{\Gamma_\oplus, \Gamma_\ominus\}$. The constraint defined by (3.19), corresponding to zero displacement fluctuations, holds on Γ_0 whereas for pairs of points belonging to $\{\Gamma_\oplus, \Gamma_\ominus\}$ constraint (4.8) applies instead.

Following the same procedure described in the previous sections, and taking into account definition (3.18), the discretised version of the kinematically

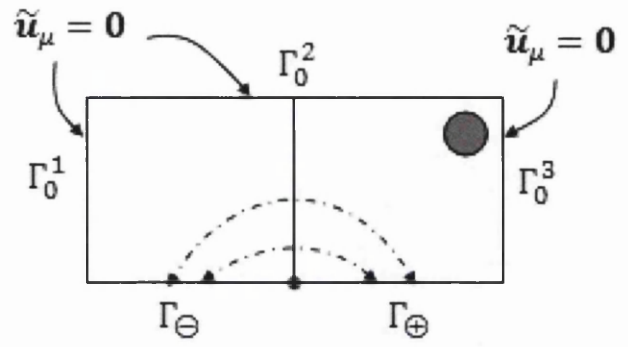

Figure 4.5: Half domain and linear boundary displacements constraint.

admissible displacement fluctuations space, $\tilde{\mathscr{K}}_\mu^h$, can be defined on the discretised half-domain ${}^{1/2}\Omega_\mu^h$, as

$$\tilde{\mathscr{K}}_\mu^h = \left\{ \mathbf{v} = \begin{bmatrix} \mathbf{v}_i \\ \mathbf{v}_\oplus \\ \mathbf{v}_\ominus \end{bmatrix} \quad | \quad \mathbf{v}_\oplus = -\mathbf{v}_\ominus \right\}. \tag{4.14}$$

The corresponding Newton-Raphson equilibrium iteration results in

$$\begin{bmatrix} \mathbf{k}_{ii} & \mathbf{k}_{i\oplus} - \mathbf{k}_{i\ominus} \\ \mathbf{k}_{\oplus i} - \mathbf{k}_{\ominus i} & \mathbf{k}_{\oplus\oplus} - \mathbf{k}_{\oplus\ominus} - \mathbf{k}_{\ominus\oplus} + \mathbf{k}_{\ominus\ominus} \end{bmatrix}^{(k-1)} \cdot \begin{bmatrix} \delta\tilde{\mathbf{u}}_i \\ \delta\tilde{\mathbf{u}}_\oplus \end{bmatrix}^{(k)} = - \begin{bmatrix} \mathbf{F}_i \\ \mathbf{F}_\oplus - \mathbf{F}_\ominus \end{bmatrix}^{(k-1)}. \tag{4.15}$$

4.3.3 Uniform boundary traction model

From point symmetry assumption in the RVE and definition (3.21), we have

$$\int_{\partial\Omega_\mu} \tilde{\boldsymbol{u}}_\mu \otimes_s \boldsymbol{n}\, dA = \int_{\partial\Omega_\mu^1} \tilde{\boldsymbol{u}}_\mu(\boldsymbol{y}_\oplus, t) \otimes_s \boldsymbol{n}_\oplus\, dA + \int_{\partial\Omega_\mu^2} \tilde{\boldsymbol{u}}_\mu(\boldsymbol{y}_\ominus, t) \otimes_s \boldsymbol{n}_\ominus\, dA = \mathbf{0}, \tag{4.16}$$

where $\boldsymbol{y}_\oplus$ and $\boldsymbol{y}_\ominus$ satisfy constraint (4.8), with normal vectors $\boldsymbol{n}_\oplus$ and $\boldsymbol{n}_\ominus$, respectively, satisfying $\boldsymbol{n}_\oplus = -\boldsymbol{n}_\ominus$. Here, $\boldsymbol{y}_\oplus$ and $\boldsymbol{y}_\ominus$ are generic points on the corresponding half-boundaries $\partial\Omega_\mu^1$ and $\partial\Omega_\mu^2$, such that $\partial\Omega_\mu = \partial\Omega_\mu^1 \cup \partial\Omega_\mu^2$. Then it follows that

$$\int_{\partial\Omega_\mu^1} \tilde{\boldsymbol{u}}_\mu(\boldsymbol{y}_\oplus, t) \otimes_s \boldsymbol{n}_\oplus\, dA = \mathbf{0}. \tag{4.17}$$

Condition (4.17) is illustrated in Figure 4.6. Here, similar to the linear boundary model, the boundary $\partial^{1/2}\Omega_\mu$ is partitioned into a subset $\Gamma_1 \equiv \Gamma_1^1 \cup \Gamma_1^2 \cup \Gamma_1^3$

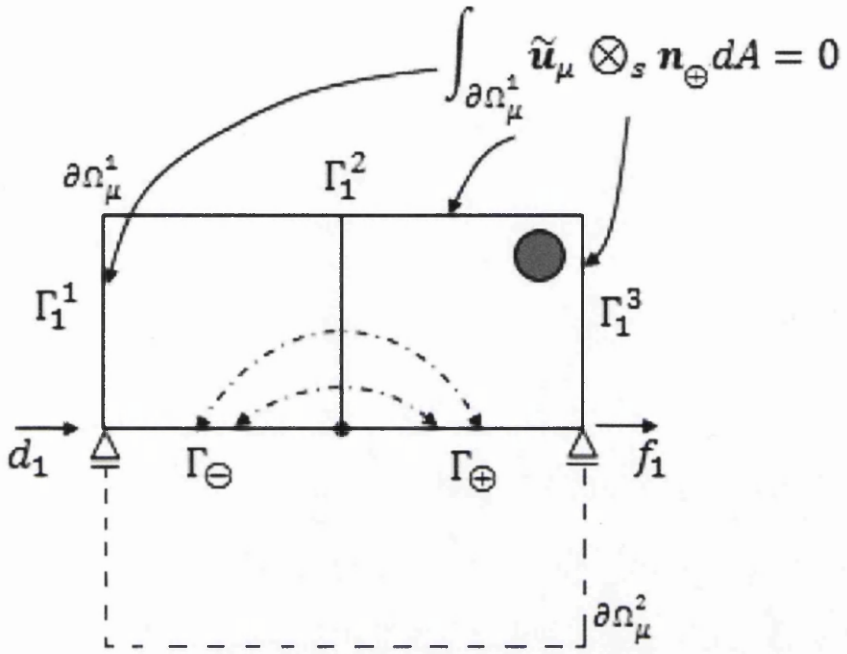

Figure 4.6: Half domain with minimal kinematic constraint.

(on $\partial\Omega^1_\mu$), and a pair of subsets $\{\Gamma_\oplus, \Gamma_\ominus\}$, such that constraint (4.17) holds for Γ_1, and Equation (4.8) for pairs located on $\{\Gamma_\oplus, \Gamma_\ominus\}$.

It is emphasised here that the assumptions of minimal kinematic constraint and linear boundary displacements place no restrictions on the geometry of the RVE. Hence, all results presented here for these two classes of multi-scale models apply equally to any RVE with point symmetry (regardless of its shape).

In the present case, the discretised space $\tilde{\mathscr{K}}^h_\mu$, can be defined on the discretised half-domain ${}^{1/2}\Omega^h_\mu$ alone as

$$\tilde{\mathscr{K}}^h_\mu = \left\{ \mathbf{v} = \begin{bmatrix} \mathbf{v}_i \\ \mathbf{v}_f \\ \mathbf{v}_d \\ \mathbf{v}_{f1} \\ \mathbf{v}_{d1} \\ \mathbf{v}_\oplus \\ \mathbf{v}_\ominus \end{bmatrix} \quad | \quad \mathbf{v}_d = \mathbf{R} \begin{bmatrix} \mathbf{v}_f \\ \mathbf{v}_{f1} \end{bmatrix} \quad ; \quad \mathbf{v}_\oplus = -\mathbf{v}_\ominus \quad ; \quad \mathbf{v}_{f1} = -\mathbf{v}_{d1} \right\}, \tag{4.18}$$

with $\mathbf{v}_{f1}$ and $\mathbf{v}_{d1}$ representing the displacement fluctuations of the degrees of freedom illustrated in Figure 4.6. Vectors $\mathbf{v}_f$, $\mathbf{v}_d$, $\mathbf{v}_\oplus$ and $\mathbf{v}_\ominus$ have the same definition as before. Matrix $\mathbf{R}$ is defined here as

$$\mathbf{R} = -\mathbf{C}_d^{-1} \left[\mathbf{C}_f \;\; (\mathbf{C}_{f1} - \mathbf{C}_{d1}) \right]. \tag{4.19}$$

The resulting reduced Newton-Raphson iteration in the present case reads

$$\begin{bmatrix} \mathbf{k}_{ii} & \mathbf{k}_{I} & \mathbf{k}_{VIII} \\ \begin{bmatrix} \mathbf{k}_{fi} \\ \mathbf{k}_{f1i} - \mathbf{k}_{d1i} \end{bmatrix} + \mathbf{R}^T \mathbf{k}_{di} & \begin{bmatrix} \mathbf{k}_{II} \\ \mathbf{k}_{III} - \mathbf{k}_{IV} \end{bmatrix} + \mathbf{R}^T \mathbf{k}_{V} & \begin{bmatrix} \mathbf{k}_{IX} \\ \mathbf{k}_{X} - \mathbf{k}_{XI} \end{bmatrix} + \mathbf{R}^T \mathbf{k}_{XII} \\ \mathbf{k}_{\oplus i} - \mathbf{k}_{\ominus i} & \mathbf{k}_{VI} - \mathbf{k}_{VII} & \mathbf{k}_{XIII} - \mathbf{k}_{XIV} \end{bmatrix}^{(k-1)} \cdot \begin{bmatrix} \delta\tilde{\mathbf{u}}_i \\ \delta\tilde{\mathbf{u}}_f \\ \delta\tilde{\mathbf{u}}_{f1} \\ \delta\tilde{\mathbf{u}}_{\oplus} \end{bmatrix}^{(k)} = - \begin{bmatrix} \mathbf{F}_i \\ \begin{bmatrix} \mathbf{F}_f \\ \mathbf{F}_{f1} - \mathbf{F}_{d1} \end{bmatrix} + \mathbf{R}^T \mathbf{F}_d \\ \mathbf{F}_{\oplus} - \mathbf{F}_{\ominus} \end{bmatrix}^{(k-1)}, \tag{4.20}$$

where:

$$\mathbf{k}_I = [\, \mathbf{k}_{if} \;\; (\mathbf{k}_{if1} - \mathbf{k}_{id1}) \,] + \mathbf{k}_{id}\mathbf{R}\,, \qquad \mathbf{k}_{II} = [\, \mathbf{k}_{ff} \;\; (\mathbf{k}_{ff1} - \mathbf{k}_{fd1}) \,] + \mathbf{k}_{fd}\mathbf{R}\,,$$
$$\mathbf{k}_{III} = [\, \mathbf{k}_{f1f} \;\; (\mathbf{k}_{f1f1} - \mathbf{k}_{f1d1}) \,] + \mathbf{k}_{f1d}\mathbf{R}\,, \qquad \mathbf{k}_{IV} = [\, \mathbf{k}_{d1f} \;\; (\mathbf{k}_{d1f1} - \mathbf{k}_{d1d1}) \,] + \mathbf{k}_{d1d}\mathbf{R}\,,$$
$$\mathbf{k}_V = [\, \mathbf{k}_{df} \;\; (\mathbf{k}_{df1} - \mathbf{k}_{dd1}) \,] + \mathbf{k}_{dd}\mathbf{R}\,, \qquad \mathbf{k}_{VI} = [\, \mathbf{k}_{\oplus f} \;\; (\mathbf{k}_{\oplus f1} - \mathbf{k}_{\oplus d1}) \,] + \mathbf{k}_{\oplus d}\mathbf{R}\,,$$
$$\mathbf{k}_{VII} = [\, \mathbf{k}_{\ominus f} \;\; (\mathbf{k}_{\ominus f1} - \mathbf{k}_{\ominus d1}) \,] + \mathbf{k}_{\ominus d}\mathbf{R}\,, \qquad \mathbf{k}_{VIII} = \mathbf{k}_{i\oplus} - \mathbf{k}_{i\ominus}\,,$$
$$\mathbf{k}_{IX} = \mathbf{k}_{f\oplus} - \mathbf{k}_{f\ominus}\,, \qquad \mathbf{k}_{X} = \mathbf{k}_{f1\oplus} - \mathbf{k}_{f1\ominus}\,,$$
$$\mathbf{k}_{XI} = \mathbf{k}_{d1\oplus} - \mathbf{k}_{d1\ominus}\,, \qquad \mathbf{k}_{XII} = \mathbf{k}_{d\oplus} - \mathbf{k}_{d\ominus}\,,$$
$$\mathbf{k}_{XIII} = \mathbf{k}_{\oplus\oplus} - \mathbf{k}_{\oplus\ominus}\,, \qquad \mathbf{k}_{XIV} = \mathbf{k}_{\ominus\oplus} - \mathbf{k}_{\ominus\ominus}\,.$$

4.4 Simultaneous symmetry conditions

If both the staggered-translational and point symmetries discussed in the above are present, then a further reduction in computational costs can be obtained. As commented in Section 4.2, the implementation of the staggered-translational symmetry is given only for the periodic boundary displacement fluctuations model. Thus, in the following, the simulatenous symmetries condition will be addressed only for this particular model.

4.4.1 Periodic boundary displacement fluctuations model

Figure 4.7(a) shows a typical chessboard-type pattern where both symmetry conditions are met. In such cases, conditions (4.4) and (4.8) must be satisfied simultaneously. This implies that thirteen points of the RVE have zero displacement fluctuation:

$$\tilde{\boldsymbol{u}}_\mu(\boldsymbol{z}^j, t) = \mathbf{0}, \qquad j = 1, \cdots, 13. \tag{4.21}$$

In this case, the analysis can be reduced to a symmetric quarter of the original RVE domain, which we shall refer to as ${}^{1/4}\Omega_\mu$. The choice of ${}^{1/4}\Omega_\mu$ is not arbitrary. The reduced RVE domain must be selected such that the

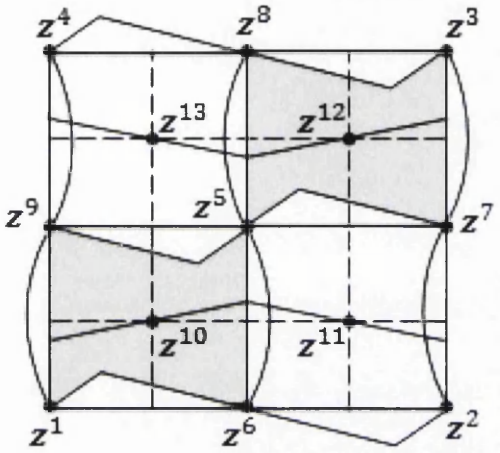

(a) Displacement fluctuation field and zero-values for the simultaneous symmetry case.

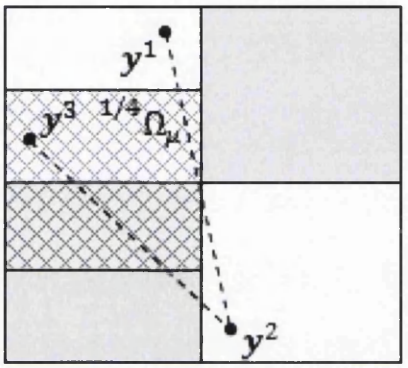

(b) Choice of a quarter-domain $^{1/4}\Omega_\mu$ (region with diagonal lines).

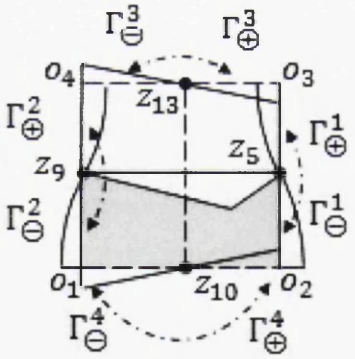

(c) One-to-one correspondence between points on $^{1/4}\partial\Omega_\mu$

Figure 4.7: Simultaneous staggered-translational and point-symmetry.

entire field of displacement fluctuations of the original RVE domain Ω_μ can be obtained directly from the field over ${}^{1/4}\Omega_\mu$ by using constraints (4.4) and (4.8) alone. One possible choice is the reduced domain shown in Figure 4.7(b). For instance, this figure shows an arbitrary point $\boldsymbol{y}^1 \in \Omega_\mu$ lying outside ${}^{1/4}\Omega_\mu$. By point symmetry, the fluctuation at point $\boldsymbol{y}^2$, also lying outside ${}^{1/4}\Omega_\mu$, is

$$\tilde{\boldsymbol{u}}_\mu(\boldsymbol{y}^2, t) = -\tilde{\boldsymbol{u}}_\mu(\boldsymbol{y}^1, t). \tag{4.22}$$

By staggered-translational symmetry, this fluctuation is identical to that of point $\boldsymbol{y}^3$ which, in turn, belongs to the reduced domain ${}^{1/4}\Omega_\mu$:

$$\tilde{\boldsymbol{u}}_\mu(\boldsymbol{y}^2, t) = -\tilde{\boldsymbol{u}}_\mu(\boldsymbol{y}^1, t) = -\tilde{\boldsymbol{u}}_\mu(\boldsymbol{y}^3, t). \tag{4.23}$$

To define the appropriate boundary kinematical constraints in this case, we firstly note that the simultaneous symmetry conditions imply that the displacement fluctuation field on each side of the reduced RVE has point symmetry about the corresponding mid-point (see Figure 4.7(c)). It is then convenient to split the reduced RVE boundary $\partial^{1/4}\Omega_\mu$ into four pairs of subsets $\{\Gamma^j_\oplus, \Gamma^j_\ominus\}$ such that the one-to-one correspondence between points $\boldsymbol{y}_\oplus$ and $\boldsymbol{y}_\ominus$ belonging to a pair of subsets is defined by point symmetry about the mid-point of each side. The boundary constraint to be imposed in this case satisfies Equation (4.8).

To proceed with the description of the finite element implementation of the present type of RVE symmetry, similarly to (4.11) we define

$$\{\Gamma_\oplus, \Gamma_\ominus\} \equiv \left\{ \bigcup_{j=1}^{4} \Gamma^j_\oplus, \bigcup_{j=1}^{4} \Gamma^j_\ominus \right\}. \tag{4.24}$$

The space of kinematically admissible nodal displacement fluctuation vectors over the discretised reduced domain ${}^{1/4}\Omega^h_\mu$ is accordingly defined as

$$\tilde{\mathscr{K}}^h_\mu = \left\{ \mathbf{v} = \begin{bmatrix} \mathbf{v}_i \\ \mathbf{v}_\oplus \\ \mathbf{v}_\ominus \\ \mathbf{v}_{o_1} \\ \mathbf{v}_{o_2} \\ \mathbf{v}_{o_3} \\ \mathbf{v}_{o_4} \end{bmatrix} \quad | \quad \mathbf{v}_\oplus = -\mathbf{v}_\ominus \quad ; \quad \mathbf{v}_{o_1} = -\mathbf{v}_{o_2} = \mathbf{v}_{o_3} = -\mathbf{v}_{o_4} \right\} \tag{4.25}$$

where $\mathbf{v}_{o_1}$, $\mathbf{v}_{o_2}$, $\mathbf{v}_{o_3}$ and $\mathbf{v}_{o_4}$ contain the degrees of freedom of the corner nodes of the cell as shown in Figure 4.7(c) and $\mathbf{v}_\oplus$ and $\mathbf{v}_\ominus$ contain the degrees of freedom of the boundary nodes that satisfy the point symmetric one-to-one correspondence referred to in the above.

Finally, with the above at hand, we find that the iterative correction to the nodal displacement fluctuation vector for a Newton-Raphson iteration (k) in the present case is obtained as the solution of the equation system:

$$\begin{bmatrix} \mathbf{k}_{ii} & \mathbf{k}_{i\oplus} - \mathbf{k}_{i\ominus} \\ \mathbf{k}_{\oplus i} - \mathbf{k}_{\ominus i} & \mathbf{k}_{\oplus\oplus} - \mathbf{k}_{\oplus\ominus} - \mathbf{k}_{\ominus\oplus} + \mathbf{k}_{\ominus\ominus} \\ \mathbf{k}_{o_1 i} - \mathbf{k}_{o_2 i} + \mathbf{k}_{o_3 i} - \mathbf{k}_{o_4 i} & \mathbf{k}_{o_1\oplus} - \mathbf{k}_{o_1\ominus} - \mathbf{k}_{o_2\oplus} + \mathbf{k}_{o_2\ominus} + \mathbf{k}_{o_3\oplus} - \mathbf{k}_{o_3\ominus} - \mathbf{k}_{o_4\oplus} + \mathbf{k}_{o_4\ominus} \end{bmatrix}$$

$$\begin{bmatrix} \mathbf{k}_{io_1} - \mathbf{k}_{io_2} + \mathbf{k}_{io_3} - \mathbf{k}_{io_4} \\ \mathbf{k}_{\oplus o_1} - \mathbf{k}_{\oplus o_2} + \mathbf{k}_{\oplus o_3} - \mathbf{k}_{\oplus o_4} - \mathbf{k}_{\ominus o_1} + \mathbf{k}_{\ominus o_2} - \mathbf{k}_{\ominus o_3} + \mathbf{k}_{\ominus o_4} \\ \mathbf{k}_{\mathrm{I}} - \mathbf{k}_{\mathrm{II}} + \mathbf{k}_{\mathrm{III}} - \mathbf{k}_{\mathrm{IV}} \end{bmatrix}^{(k-1)} \begin{bmatrix} \delta\tilde{\mathbf{u}}_i \\ \delta\tilde{\mathbf{u}}_\oplus \\ \delta\tilde{\mathbf{u}}_{o_1} \end{bmatrix}^{(k)}$$

$$= - \begin{bmatrix} \mathbf{F}_i \\ \mathbf{F}_\oplus - \mathbf{F}_\ominus \\ \mathbf{F}_{o_1} - \mathbf{F}_{o_2} + \mathbf{F}_{o_3} - \mathbf{F}_{o_4} \end{bmatrix}^{(k-1)} \tag{4.26}$$

with

$$\mathbf{k}_{\mathrm{I}} = \mathbf{k}_{o_1 o_1} - \mathbf{k}_{o_1 o_2} + \mathbf{k}_{o_1 o_3} - \mathbf{k}_{o_1 o_4}\,, \quad \mathbf{k}_{\mathrm{II}} = \mathbf{k}_{o_2 o_1} - \mathbf{k}_{o_2 o_2} + \mathbf{k}_{o_2 o_3} - \mathbf{k}_{o_2 o_4}\,,$$
$$\mathbf{k}_{\mathrm{III}} = \mathbf{k}_{o_3 o_1} - \mathbf{k}_{o_3 o_2} + \mathbf{k}_{o_3 o_3} - \mathbf{k}_{o_3 o_4}\,, \quad \mathbf{k}_{\mathrm{IV}} = \mathbf{k}_{o_4 o_1} - \mathbf{k}_{o_4 o_2} + \mathbf{k}_{o_4 o_3} - \mathbf{k}_{o_4 o_4}.$$

As we shall see in the following section, the savings in computing time in the present case can be substantial.

4.5 Numerical examples

This section illustrates by means of numerical examples the significant reductions in computational costs that are obtained as a result of the relatively straightforward implementation of the symmetry conditions discussed in the preceding sections. For completeness, the resulting speed-up factors achieved for both single-scale analysis (i.e., analysis involving the RVE alone) and fully coupled two-scale analysis are presented. Since we are interested in quantifying the reduction of CPU times in the analyses, arbitrary loading programmes are imposed in all of the numerical examples. In all cases, the full Newton-Raphson scheme, characterised by quadratic rates of asymptotic convergence, is adopted in the solution of the RVE equilibrium problem as well as in the global (macroscopic) equilibrium problem. The corresponding linear systems of equations are dealt with by the HSL/MA41 direct sparse frontal solver (Amestoy and Duff 1993).

4.5.1 Point-symmetry. Square unit cell with two circular holes

This example illustrates the point-symmetry case under the linear boundary displacement and uniform boundary traction assumptions. A square RVE (shown in Figure 4.11(a)) under plane stress is assumed which is made of a von Mises elastic-perfectly plastic matrix containing two holes. Small strains formulation is considered here. The diameter of each hole is taken as 20% of the

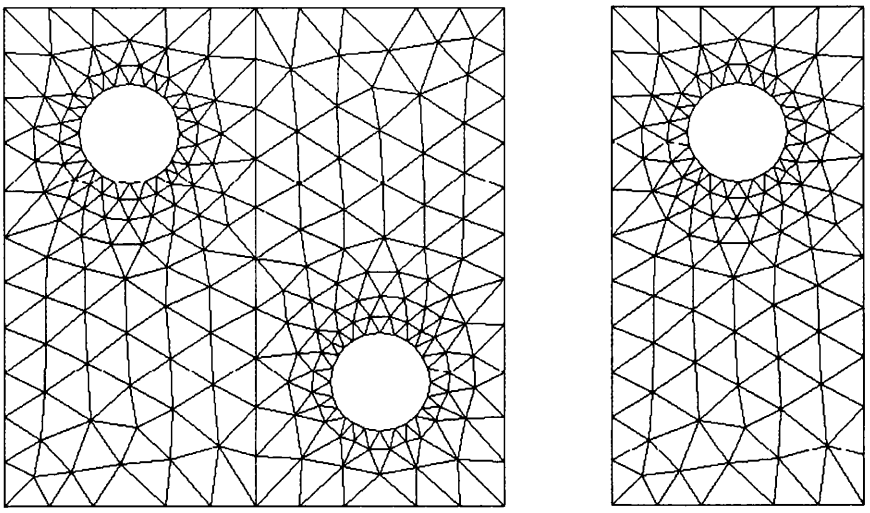

(a) Full square RVE geometry without symmetry considerations.

(b) Half square RVE when point symmetry conditions are included.

Figure 4.8: Typical square RVE with two circular voids.

length of the side of the RVE. The matrix material has Young modulus $E = 200\text{GPa}$, Poisson ratio $\nu = 0.3$ and yield stress $\sigma_y = 0.24\text{GPa}$. A single-scale analysis is carried out where the RVE is subjected to an incremental macroscopic engineering strain array $\boldsymbol{\epsilon} = \{\epsilon_{xx}, \epsilon_{yy}, \gamma_{xy}\} = \{0.0015, 0.0004, 0.0035\}^T$ imposed in 20 proportional steps. In all cases (and in what follows), x and y axes coincide respectively with the horizontal and vertical directions. For comparison, the calculations are carried out for the full RVE (Figure 4.11(a)) as well as for a reduced counterpart (Figure 4.11(b)) obtained by considering the underlying point symmetry. The full RVE is discretised by a mesh of 418 three-noded linear triangular elements and a total of 253 nodes. The reduced RVE mesh contains 209 elements and 132 nodes. In order to make consistent comparisons, the full RVE mesh was generated through a rotation of coordinates of the half-RVE mesh. The macroscopic array of stress components obtained at the end of the loading programme for the linear boundary displacement model

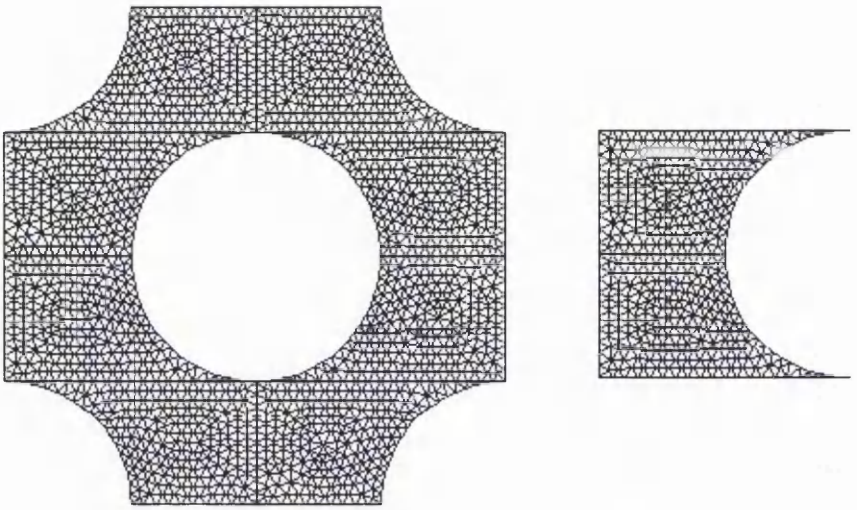

(a) Full RVE geometry, without symmetry considerations.

(b) Quarter-domain RVE.

Figure 4.9: Typical square RVE with staggered circular holes.

is $\boldsymbol{\sigma} = \{\sigma_{xx}, \sigma_{yy}, \tau_{xy}\}^T = \{0.1286, 0.0695, 0.0951\}^T$GPa. For the uniform boundary traction model in turn we obtain $\boldsymbol{\sigma} = \{0.0985, 0.0597, 0.0921\}^T$GPa.

Very importantly, the CPU time required in the solution of the linear boundary displacements model, with the reduced RVE is only 53% of that required when the full RVE is used, corresponding to a speed-up factor of 1.89. Similarly, in the solution of the uniform boundary traction model, the speed-up factor obtained is 1.79.

4.5.2 Square unit cell with staggered circular holes

Here we analyse again a model of porous-plastic material. Only the single-scale case is considered under the periodic boundary fluctuations kinematical constraint. Small plastic strains and plane stress are assumed. The pores represented by circular holes in the RVE have staggered-translational symmetry. In the present case, both point-symmetry and staggered-translational symmetry conditions are met. The full RVE, without symmetry considerations, is illustrated in Figure 4.9(a).

The circular holes have diameter equal to one half of the side of the cell. The corresponding mesh has 2768 three-noded linear triangular elements and 1500 nodes. The reduced RVE – in this case comprising only one quarter of its original counterpart – is shown in Figure 4.9(b). The mesh contains 692 elements and 396 nodes. The behaviour of the matrix material is de-

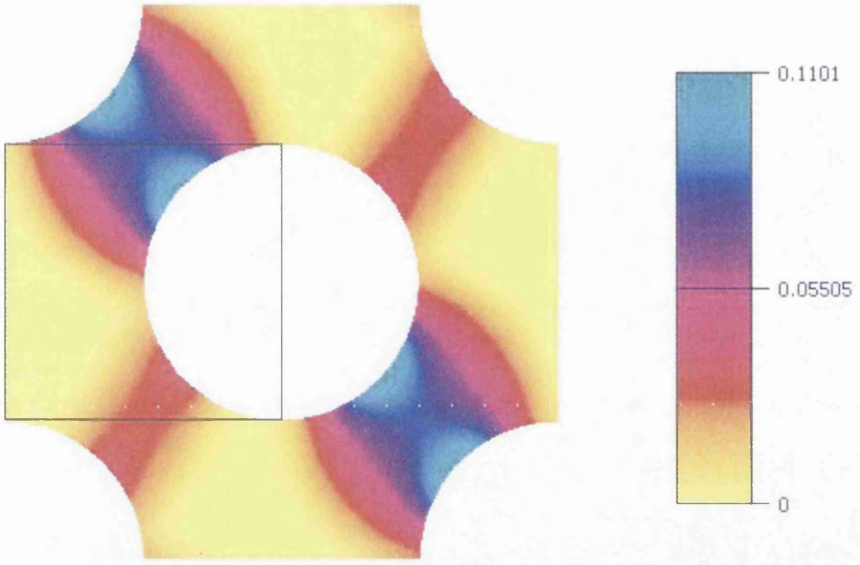

Figure 4.10: Contour diagram of equivalent plastic strains in the full microscopic cell and in a quarter-domain (enclosed by a black square). Simultaneous symmetries are emphasised by the contour plot in the quarter-domain and by its repetition (four times) in the full RVE domain.

scribed by a linearly isotropic hardening von Mises model, with Young modulus $E = 68.9\text{GPa}$, Poisson ratio $\nu = 0.33$, initial yield stress $\sigma_y = 0.24\text{GPa}$ and hardening modulus $H = 2.5\text{GPa}$. The simulation here consists in prescribing a total macroscopic engineering strain array $\boldsymbol{\epsilon} = \{0.02, 0.03, 0.03\}^T$ incrementally in 26 proportional load steps. The resulting homogenised stress components are $\boldsymbol{\sigma} = \{0.119, 0.124, 0.023\}^T\text{GPa}$ for both RVEs. The speed-up factor achieved with the consideration of both symmetries in the reduced RVE was 5.72. These symmetries are emphasised in Figure 4.10, where the corresponding contour plot of accumulated plastic strain at the end of the loading programme is shown for both RVEs.

4.5.3 Square unit cell with centred circular hole

The use of point-symmetry in the RVE is illustrated here under periodic boundary fluctuations kinematical constraint. We consider a periodic porous-plastic medium represented as a square RVE under plane strain conditions containing a centred circular hole, as shown in Figure 4.11(a). The RVE matrix is modelled as an elastic-perfectly plastic von Mises material under infinitesimal strains. An identical RVE was used by Giusti *et al.* (Giusti, Blanco, de Souza Neto and Feijóo 2009) in the estimation of macroscopic

porous-plastic yield surfaces. The size of the hole corresponds to a void ratio of 15%. The matrix material has Young modulus $E = 200$GPa, Poisson ratio $\nu = 0.3$ and yield stress $\sigma_y = 0.24$GPa.

We start with a single-scale analysis, where the RVE is subjected to an incremental macroscopic engineering strain array $\boldsymbol{\epsilon} = \{\epsilon_{xx}, \epsilon_{yy}, \gamma_{xy}\} = \{0.007, 0.01, 0.01\}^T$ imposed in 19 proportional steps. For comparison, the calculations are carried out for the full RVE (Figure 4.11(a)) as well as for a reduced counterpart (Figure 4.11(b)) obtained by considering underlying point-symmetry.

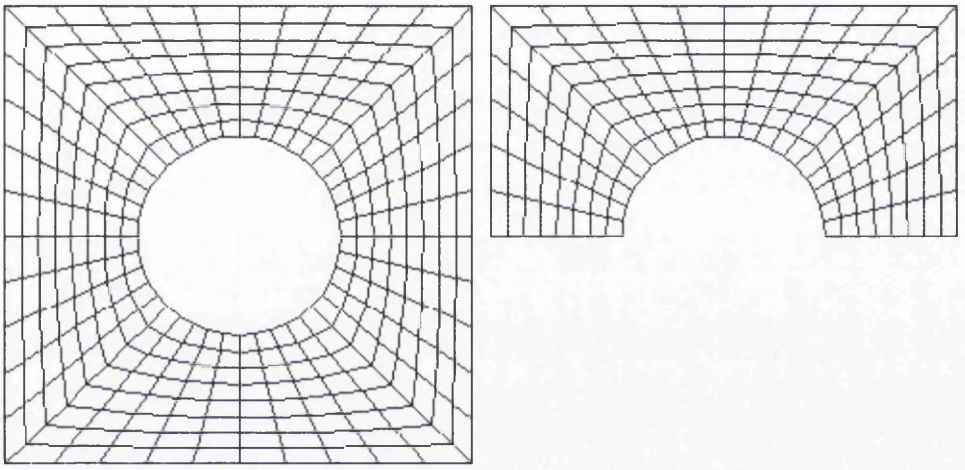

(a) Full square RVE geometry without symmetry considerations.

(b) Half square RVE when point-symmetry condition is included.

Figure 4.11: Typical square RVE with a centred circular void.

The full RVE is discretised by a mesh of 320 eight-noded quadrilateral isoparametric elements with reduced (2×2) Gauss quadrature and a total of 1040 nodes. The reduced RVE mesh contains 160 elements and 537 nodes. The macroscopic array of stress components obtained at the end of the loading programme for both cases is $\boldsymbol{\sigma} = \{\sigma_{xx}, \sigma_{yy}, \tau_{xy}\}^T = \{0.232, 0.232, 7.322 \times 10^{-4}\}^T$GPa. Very importantly, the CPU time required in the solution with the reduced RVE is only 35% of that required when the full RVE is used. This corresponds to a speed-up factor of 2.86.

In a second step, a fully coupled two-scale finite element analysis is carried out where the above RVEs are used to define the macroscopic constitutive response at each Gauss-point of the macroscopic mesh. The macroscopic initial value problem considered consists of a perforated strip with a circular hole in the centre, subjected to uniaxial stretching. For obvious symmetry reasons, only a quarter of the problem geometry is discretised and a mesh of

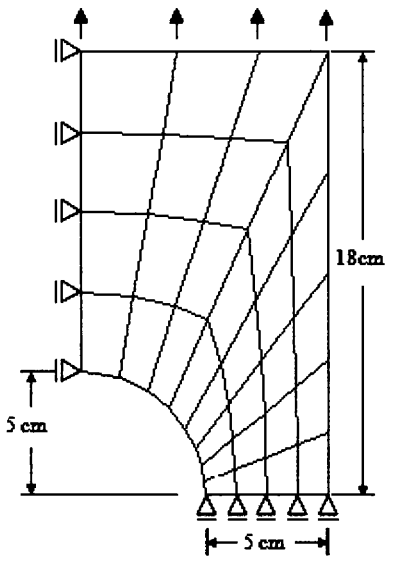

Figure 4.12: Perforated strip under tensile load (Mid-side nodes have been omitted in the mesh).

32 eight-noded quadrilateral elements with reduced (2×2) Gauss quadrature is adopted with a total number of 121 nodes (Figure 4.12).

The loading programme consists in applying a monotonically increasing uniform vertical displacement on the nodes of the upper edge of the mesh up to a total displacement of 0.1% of the original length of the strip. A total number of 60 proportional load steps is used. The total vertical reaction at the constrained nodes of the macroscopic mesh at the end of the loading programme is 8.425KN. Again, a very substantial reduction in CPU time is observed when the point-symmetry is taken into account in the treatment of the RVE equilibrium problem. Here, the total CPU analysis time observed with the reduced RVE is only 31% of that of the full RVE. The corresponding speed-up factor is 3.23.

4.5.4 RVE with honeycomb-type microstructure

In this example, we consider the fully coupled two-scale analysis of materials with honeycomb-type periodic microstructures. The RVE in such cases satisfies both staggered-translational and point symmetry. This type of microstructure is encountered in most species of wood and is also common in many engineered materials. The particular geometry adopted in the present analysis have been obtained from Watanabe et al. (2000) and correspond to Pinus radiata wood cells. It consists of a periodic arrangement of hexagonal cells whose wall material is modelled here by an elastic-perfectly plastic von

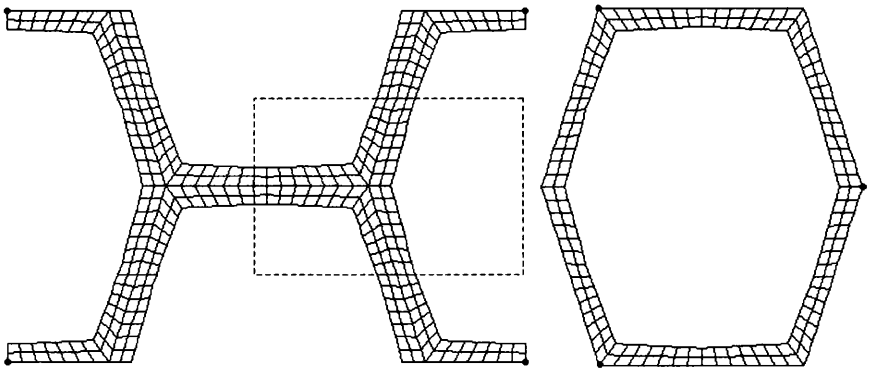

(a) Finite element mesh of full RVE with honeycomb-type pattern, represented by Ω_μ^h. Dashed square shows a quarter-domain.

(b) Mesh of hexagonal RVE, corresponding to a discretised half-domain ${}^{1/2}\Omega_\mu^h$. Use of staggered-translational symmetry.

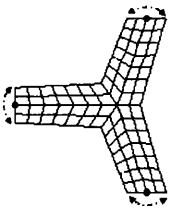

(c) A discretised quarter-domain. Use of staggered-translational and point symmetries.

Figure 4.13: Honeycomb-type microstructure represented by different RVEs.

Mises law under plane strain conditions and small strains regime. The corresponding material constants are: Young modulus $E = 30\text{GPa}$, Poisson ratio $\nu = 0.2$ and yield stress $\sigma_y = 180\text{MPa}$.

For comparison, the coupled two-scale analysis is carried out with the multi-scale constitutive model described by three different RVEs: The full RVE (Figure 4.13(a)); A half-domain RVE (Figure 4.13(b)), obtained by from the full RVE by staggered-translational symmetry consideration alone, and; A quarter-domain RVE (Figure 4.13(c)), obtained by considering both symmetries.

The full RVE mesh contains 336 eight-noded quadrilateral isoparametric elements with reduced (2×2) integration points with a total number of 1221 nodes. The half-domain RVE mesh consists of 168 elements and 672 nodes

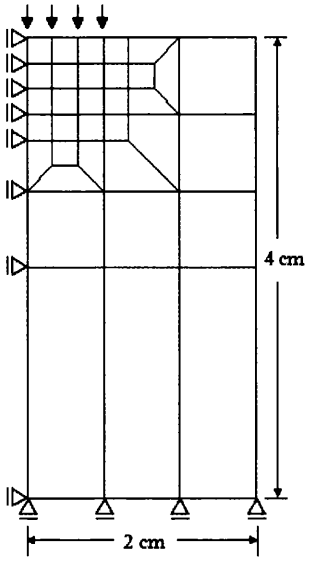

Figure 4.14: Timber block subjected to compression load (Mid-side nodes have been omitted in the mesh).

and the quarter-domain is discretised with 84 elements and 307 nodes. Figure 4.13(c) also illustrates the one-to-one correspondence in the sets of boundary nodes of $\partial^{1/4}\Omega_\mu^h$, as explained earlier (Figure 4.7(c)). The nodes highlighted in black have zero prescribed displacement fluctuation.

The macroscopic problem consists of the compression of a 4cm $\times$4cm specimen of timber in plane strain (Figure 4.14).

A mesh of 34 eight-noded isoparametric quadrilaterals with reduced 2×2 Gauss quadrature is used to discretise one symmetric half of the problem domain with appropriate kinematical constraints imposed along the symmetry lines. The total number of nodes is 123. The compression load is applied by means of a uniform prescribed vertical displacement of the central nodes of upper edge. The total prescribed compressive displacement, corresponding to 0.5% of the initial length of the sample, is applied in 20 incremental steps. The maximum total reactive force on the constrained edge is found to be 57.823N (which is the same in the three cases tested). Again, the speed-up obtained as a result of the symmetry considerations at the RVE level are substantial. For the half-domain RVE, the speed-up factor (compared to the full RVE description) is 2.15. With the quarter-domain RVE description, for which all symmetries are explored simultaneously, the speed-up factor achieved is 7.41.

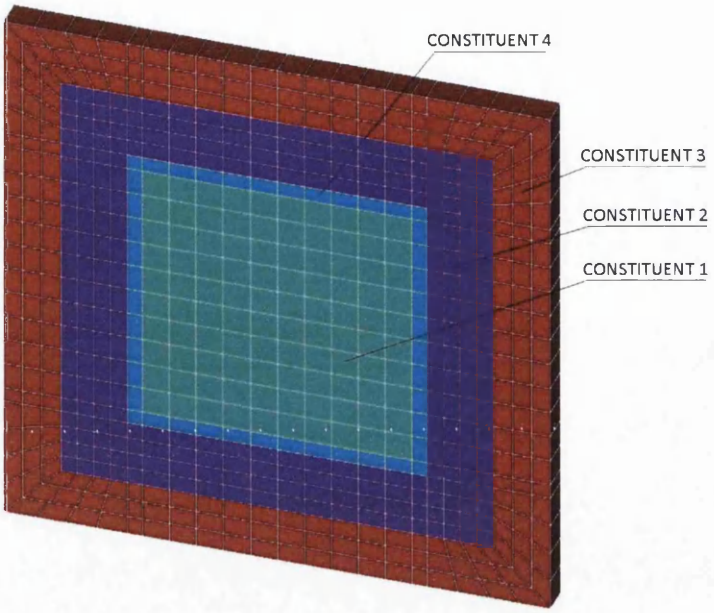

Figure 4.15: Finite element mesh of full *RVE I* domain

4.5.5 RVE with constituent described by a second RVE

In this example, we consider a three-dimensional periodic microstructure represented by a RVE, called *RVE I* (Figure 4.15). *RVE I* satisfies point-symmetry and has four constituents: *constituents 1*, *2*, *3* and *4*, with volume fractions 0.243, 0.325, 0.375 and 0.057, respectively. The mechanical response of constituent *1* is obtained by the computational homogenisation of a second RVE, named *RVE II* (Figure 4.16). This RVE is described by periodic and alternating regions of *constituents A* and *B*, with volume fractions of 0.66 and 0.44, respectively. Material of constituent *A* is assumed to be purely elastic, with Young modulus $E_A = 17.5$GPa and Poisson ratio $\nu_A = 0.3$. Material of constituent *B* is modelled by an elastic-perfectly plastic von Mises law, with Young modulus $E_B = 10.42$GPa, Poisson ratio $\nu_B = 0.23$ and yield stress $\sigma_{y_B} = 0.4$MPa. Similarly, materials of constituents *2*, *3* and *4* are also modelled here as elastic-perfectly plastic von Mises materials. The corresponding mechanical properties of material in constituent *2* are: Young modulus $E_2 = 0.4$GPa, Poisson ratio $\nu_2 = 0.2$ and yield stress $\sigma_{y_2} = 0.22$MPa. For constituent *3*, the properties are : Young modulus $E_3 = 2.75$GPa, Poisson ratio $\nu_3 = 0.3$ and yield stress $\sigma_{y_3} = 0.22$MPa; and for constituent *4*: Young modulus $E_4 = 10.42$GPa, Poisson ratio $\nu_4 = 0.23$ and yield stress $\sigma_{y_4} = 0.4$MPa. Large strain formulation is adopted in all the analyses.

To eliminate volumetric locking, F-Bar methodology (de Souza Neto et al. 1996) is used in the finite element meshes. The full *RVE I* mesh con-

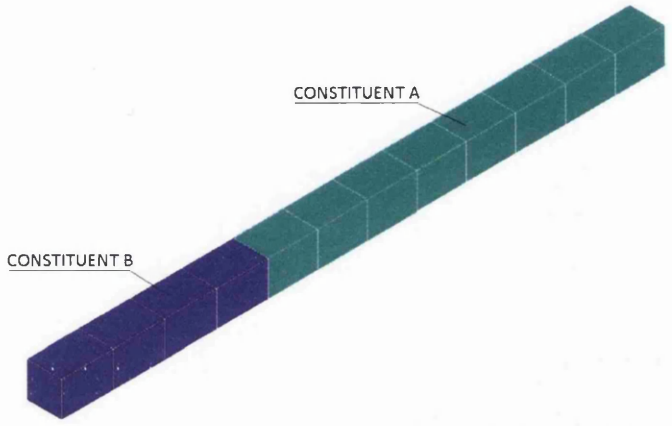

Figure 4.16: Finite element mesh of *RVE II*. This RVE defines the constitutive law at each gauss integration point of the *constituent 1*, in the *RVE I*.

tains 640 F-bar eight-noded hexahedral elements with a total number of 1362 nodes. The *RVE II* mesh has 12 F-bar eight-noded hexahedral elements with a number of 52 nodes.

By taking into account point-symmetry, a half of the full *RVE I* domain is modelled (4.17). The half-domain *RVE I* mesh consists of 320 F-bar eight-noded hexahedral elements and 708 nodes. As shall be seen in the next Chapter 5, a similar geometry will be adopted in the analysis of wood cell-wall.

The simulation here consists in prescribing a total engineering strain array $\boldsymbol{\epsilon} = \{-0.00015, -0.00015, 0.05, 0, 0, 0\}^T$ incrementally on the *RVE I* in 10 proportional load steps. The resulting homogenised stress components are $\boldsymbol{\sigma} = \{0.02613, 0.02613, 0.22595, 0, 0, 0\}^T$GPa for both full and half-*RVE I* domains. The speed-up factor achieved with the consideration of point-symmetry in the reduced *RVE I* domain compared to the corresponding full RVE is 2.08.

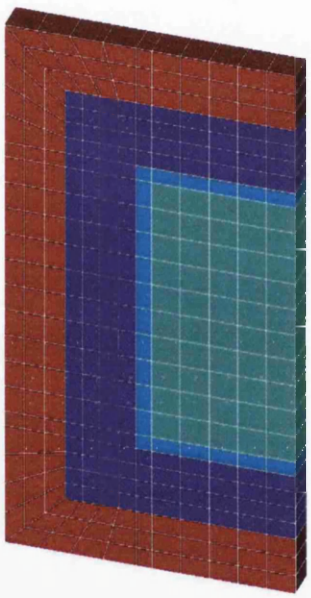

Figure 4.17: Finite element mesh of half *RVE I* domain

CHAPTER 5

Finite element modelling of wood cell-wall

5.1 Introduction

Over the last few years, the investigation of the complex interacting mechanisms of wood at nano- and microscopic levels by means of multi-scale finite element models has brought substantial progress to the understanding of the linear elastic response of these materials (Holmberg et al. 1999, Hofstetter et al. 2005, Hofstetter et al. 2007, Qing and Mishnaevsky 2009*a*, Qing and Mishnaevsky 2009*b*, Qing and Mishnaevsky 2010).

Multi-scale approaches to constitutive modelling have an inherent potential ability to capture the macroscopic dissipative response under complex strain paths which is of difficult representation by means of conventional internal variable-based phenomenological theories. Successful use of methodologies of this type in the context of dissipative phenomena is reported, for example, in the modelling of crystal plasticity (Miehe et al. 1999, Watanabe et al. 2008), frictional granular (Wellmann and Wriggers 2008) and cellular plastic materials (Terada et al. 2003). Until now, however, research on the multi-scale constitutive description of wood appears to have been focussed exclusively on the study of reversible behaviour.

Probably, one of the most crucial factors in understanding the mechanical dissipation in wood across different scales is the role played by its three major nanostructural constituents – hemicellulose, lignin and cellulose – and the associated irreversible processes in the wood cell-wall.

Despite the considerable effort devoted to the experimental study of the basic constituents of wood cell-wall, only little is currently known about their mechanical properties and interactions as a composite material (Burgert et al. 2006). One important contribution to the understanding of cell-wall mechanics has been recently made by Keckés et al. (2003). These authors showed how wood tissue and individual cells are able to undergo large deformations without apparent damage and also proposed a recovery mechanism after irreversible deformation, interpreted as a *stick-slip* mechanism at the molecular level. They showed that this *velcro*-like mechanism produces a plastic response similar to crystallographic sliding in polycrystalline metals.

In this chapter, we investigate the highly non-linear irreversible behaviour

of wood cell-wall by means of a finite element-based computational multi-scale approach. In this context, we propose a three-scale constitutive model where the response of the cell-wall composite (the large scale continuum in the present case) is obtained by the computational homogenisation of a Representative Volume Element (RVE) of cell-wall material (the *microfibril RVE*) at nanoscopic level (the intermediate scale), whose mechanical response prediction, in turn, involves the computational homogenisation of a *cellulose core RVE* made of crystalline and amorphous cellulose (the small scale). A large strain formulation is adopted throughout. We remark that the consideration of finite strain kinematics is crucial in the present context in view of the magnitude of the strains involved in the analyses carried out and resulting phenomena such as large cellulose fibre rotation. We anticipate that key features of the mechanical behaviour of wood cell-wall, such as fibre reorientation-induced stiffening, viscous relaxation, stiffness recovery mechanism and hysteresis are reproduced by the proposed model. The predictive capability of the present multi-scale model is demonstrated by comparing the results obtained in Numerical Material Tests with published experimental data (Keckés et al. 2003). Further investigation of the numerical results suggests a possible failure mechanism for the cell-wall under straining, associated with the inelastic yielding of the amorphous portion of cellulose.

In what follows, we shall focus on the description of this multi-scale model and at the end of this chapter, some numerical results will be given. We refer here to Saavedra Flores et al. (2011).

5.2 Finite element modelling of wood cell-wall

In order gain insight into the complex phenomena of mechanical interactions in wood at the level of chemical constituents, we select *compression wood* of Norway spruce (*Picea abies* (L.) Karts.) for our study. The moisture condition considered here is that found naturally in living trees. In this state, *compression wood* displays remarkable features, particularly suitable for the study of internal mechanisms present in the cell-wall. Under natural conditions, *compression wood* cells are characterised by a low content of cellulose which results in low overall stiffness, and by large MFAs that vary substantially under tensile loading. These features allow *compression wood* cells to become very flexible and develop high levels of deformation and strain when stressed.

The procedure adopted here consists of assuming that the S2 layer is a representative enough portion of the entire cell-wall for the purpose of describing the overall mechanical behaviour of cell-walls. This assumption makes sense since the S2 layer in spruce cells amounts to about 80% of the total cell-wall volume (Fengel and Stoll 1973) and, as was already explained in Chapter 2, is

the principal element controlling the strength in the wood cell. This simplification allows us to model the cell-wall by means of a RVE called *microfibril–RVE*, representing a typical *microfibril* in the middle secondary layer S2. It consists of lignin, hemicellulose, an outer amorphous cellulose layer and a periodic crystalline-amorphous cellulose core (refer to Figure 2.7). Simultaneously, at a lower scale, this periodic arrangement of crystalline-amorphous cellulose is characterised by a single material whose constitutive description is defined by a second RVE, named *cellulose core–RVE*. Consequently, what we propose here is a fully coupled three-scale model, in which the overall mechanical response of the cell-wall composite (large scale) is obtained by the computational homogenisation of the *microfibril*–RVE at the nanoscopic level (intermediate scale). Further, the mechanical response prediction of the *microfibril*–RVE, in turn, involves the computational homogenisation of the cellulose core–RVE at the level of the crystalline and amorphous portions of cellulose (small scale). That is to say, each *microfibril*–RVE equilibrium problem is solved simultaneously with a large number of cellulose core–RVE equilibrium problems at Gauss-point level of the *microfibril*–RVE finite element mesh.

Timell (1982) specified for *compression wood* 30% of cellulose content, about 29% for hemicelluloses and a range of 35–40% for lignin. Similar values for spruce were presented by Timell (1986) later on. Consequently, in the present model we adopt volume fractions of 30, 32.5 and 37.5% for cellulose, hemicellulose and lignin, respectively.

Due to the highly non-linear nature of the phenomena taking place within the cell-wall, we remark that all the aspects of modelling discussed here take into account non-linear kinematics and dissipative response of the material under finite strains regime.

5.2.1 Hemicellulose and lignin. Constitutive description

As previously mentioned, hemicellulose structure is partially amorphous. It is considered that certain fraction of its structure is aligned along the *microfibril* and consequently, its general behaviour can be modelled as orthotropic (Salmén 2004). However, the principal mode of deformation in hemicellulose during tension of the cell-wall is related exclusively to shear, with little contribution of the degree of anisotropy in the mechanical response (Nilsson and Gustafsson 2007). Hence, an assumption of isotropy will be adopted here to describe hemicellulose. In the same way, lignin is assumed to be an isotropic material due to its amorphous nature.

Hemicellulose and lignin materials are modeled here with a visco-elastic/visco-plastic response. Experimental evidence of rate-dependent behaviour in the lignin-hemicellulose matrix, isolated fibres or thin wood tissues can be found, for instance, in Navi (1995), Baley (2002), Keckés et al. (2003) and Sedighi-Gilani and Navi (2007). To capture rate-dependence, we shall

adopt for both hemicellulose and lignin, a constitutive model based on the combined action of two rheological models in parallel arrangement. The first component corresponds to a visco-plastic Prandtl model, whereas the second component, to a visco-elastic Maxwell model. For further details, we refer to Perić and Dettmer (2003). In what follows, we describe the assumptions made in the modelling of each of these rheological components.

(i) *Rate-dependent Prandtl model*

For the description of the constitutive response under finite strains, an isotropic hyperelastic material model is chosen for Prandtl and Maxwell components. Here, a regularised compressible version of the one-term Ogden strain energy function is adopted. The strain-energy function reads:

$$\begin{aligned}\Psi^{ogd} = \tfrac{\chi}{\alpha}((J^{-\frac{1}{3}}\lambda_1)^\alpha + (J^{-\frac{1}{3}}\lambda_2)^\alpha + (J^{-\frac{1}{3}}\lambda_3)^\alpha - 3) \\ +\tfrac{1}{2}K(lnJ)^2,\end{aligned} \tag{5.1}$$

where λ_1, λ_2 and λ_3 are the principal stretches and J the determinant of the deformation gradient, $J = det(\boldsymbol{F}) = \lambda_1\lambda_2\lambda_3$. The material constants here are χ and α and the bulk modulus K. The corresponding parameters assumed in the Prandtl rheological component for hemicellulose are: χ = 6.667e-2GPa, $\alpha = 0.5$ and K = 2.222e-2GPa. These constants are chosen such that the linearised elastic response of the Prandtl/Maxwell constitutive model for hemicellulose (under static conditions and infinitesimal strains) coincides with a linear elastic response given by a Poisson ratio $\nu = 0.2$ (Salmén 2004) and a Young modulus E = 4e-2GPa (Burgert et al. (2006), based on Salmén (2001)), for moist conditions. Further information about the mathematical theory of linearisation in the context of nonlinear elastic solids can found, for instance, in Marsden and Hughes (1983). We note also that other possible sets of Ogden material constants can be adopted in order to obtain the same linearised mechanical response. However, our particular choice has been made not only to fit the response of the hemicellulose material model in the linear elastic range but also to fit the homogenised mechanical behaviour of the *microfibril*-RVE model to experimental data over a larger range of strains.

In lignin, elastic properties can be assumed constant over 12% moisture content (Salmén 2004). Here, we adopt the following constants in the Ogden strain energy function: χ = 1.2GPa, $\alpha = 1.0$ and K = 1.3GPa. In this particular case, the linearised elastic constitutive response of the Prandtl/Maxwell model coincides with the adoption of a linear elastic mechanical behaviour given by a Poisson ratio $\nu = 0.3$ (Salmén 2004) and a Young modulus of E = 1.56GPa (the latter calculated from

the isotropic relationship $G = E/[2(1+\nu)]$, with a shear modulus $G = 0.6$GPa (Salmén 2004) and the adopted Poisson ratio $\nu = 0.3$). Similarly to hemicellulose, we also choose these constants in order to fit the homogenised mechanical response of the *microfibril*–RVE model to experimental information (refer to Section 5.3.4).

For both materials, hemicellulose and lignin, the Prandtl rheological component is modelled within a conventional von Mises visco-plasticity framework, with no hardening, endowed with a potential structure (de Souza Neto et al. 2008, Lemaitre and Chaboche 1990). Unfortunately, little experimental information has been reported on the yield stress of the lignin-hemicellulose matrix. However, in the modelling of the critical shear stress of the lignin-hemicellulose matrix, Altaner and Jarvis (2008) utilised a value of shear yield stress $\sigma_{sy} = 1.1$e-2GPa, based on Fratzl et al. (2004). By using this shear stress and the von Mises criterion, we adopt a value of yield stress $\sigma_y = 1.9$e-2GPa for hemicellulose and lignin.

Due to the lack of experimental information, it is wise to use the simplest possible description of viscous dissipative response. Then, we choose the following standard dissipation potential (de Souza Neto et al. 2008):

$$\Xi = \frac{1}{4\eta_p}\langle\Phi\rangle^2, \tag{5.2}$$

which defines the evolution of the internal variables. Here, Φ represents the von Mises yield criterion, $\langle\cdot\rangle$ the ramp function and η_p a viscosity-related parameter. In order to fit the homogenised mechanical response of the *microfibril*–RVE to experimental information and, in view of the little experimental information about viscosity-related material constants for isolated hemicellulose and lignin, we proceed to adopt a value $\eta_p = 8.5$ and 20.0GPa·s for both materials, respectively.

(ii) *Maxwell model*

As previously mentioned, a hyperelastic description for the Maxwell rheological component given by Equation (5.1) is also adopted here. We note that for a constant deformation in time the mechanical stress provided by Maxwell model tends to zero with time (relaxation). Therefore, under static conditions, the Maxwell rheological component does not contribute in the linearisation process of hemicellulose and lignin models. That is to say, the linearised response of hemicellulose and lignin constitutive models depends solely on the Prandtl rheological component. Consequently, the Ogden constants in the Maxwell model are chosen here exclusively to fit the overall mechanical response of the *microfibril*–RVE model at large strains (refer to Section 5.3.4) but not

to fit the response of the hemicellulose and lignin models to their linear elastic mechanical properties. After the fitting process, the Ogden constants adopted for hemicellulose are: $\chi = 1.2$GPa, $\alpha = 2.3$ and $K = 2.222$e-2GPa; and for lignin: $\chi = 0.2$GPa, $\alpha = 0.3$ and $K = 1.3$GPa.

To capture the viscous response of hemicellulose and lignin in the Maxwell component, we propose to adopt an evolution law suggested by Reese and Govindjee (1998), restricted here to the isochoric viscoelastic response, given by

$$-\frac{1}{2}(\mathscr{L}_v \boldsymbol{B}^e)\boldsymbol{B}^{e-1} = \frac{1}{2\eta_m}(\mathbb{I} - \frac{1}{3}\boldsymbol{I}\otimes\boldsymbol{I}) : \boldsymbol{\tau}, \tag{5.3}$$

with $\mathscr{L}_v$ representing the so-called *Lie derivative* (refer to de Souza Neto et al. (2008)), $\boldsymbol{B}^e$ the elastic left Cauchy Green strain tensor, $\boldsymbol{\tau}$ the Kirchhoff stress tensor, $\otimes$ the standard tensorial product and $\boldsymbol{I}$ and $\mathbb{I}$, the second and fourth order identity tensor, respectively. The only material constant here is the deviatoric viscosity parameter of the Maxwell model, η_m. Here, we shall adopt a value $\eta_m = 6.5$ and 3.1GPa·s for both materials, lignin and hemicellulose, respectively. As shall be seen later in Section 5.3, these values allow us to reproduce a numerical response similar to that found experimentally in wood cells.

5.2.2 Constitutive description of cellulose

The cellulose structure has already been described as a periodic alternation of amorphous and crystalline domains. In addition, an outer amorphous cellulose layer covering this periodic arrangement has been considered. Consequently, to model the whole cellulose, including this additional layer, we follow the procedure described by Andersson (2006). Donaldson and Singh (1998) employed transmission electron microscopy to obtain an average thickness of cellulose about 3.6nm, which included the crystalline core and the amorphous sheeting. Furthermore, Andersson et al. (2004) determined an average thickness of 3.2nm for the crystalline cellulose in Norway spruce. In consequence, a 0.2nm thick layer of amorphous cellulose can be assumed at the surface of the crystalline-amorphous core. Additionally, Andersson et al. (2004) indicated a mass degree of crystallinity of 52%. Since the density of the crystalline and amorphous constituents are approximately in the same order of magnitude, 1.59 and 1.50g/cm^3, respectively (Hofstetter et al. 2005), no distinction between volumetric and mass degree of crystallinity is needed. Considering a mean length of the crystalline fraction about 36.4nm, there should be a length of 18.9nm of amorphous cellulose between two consecutive crystalline units (Andersson 2006).

Further description of the assumptions made in the modelling of both materials is given in the following.

(i) *Amorphous cellulose*

It is obvious that because of the random structure of amorphous cellulose, we assume isotropy. In addition, since the deformation of (amorphous and crystalline) cellulose is very small as a consequence of its interaction with the weak hemicellulose-lignin matrix, a compressible version of the isotropic Neo-Hookean strain-energy function is chosen here, due to its mathematical simplicity and predictive accuracy for moderate deformations.

The amorphous cellulose assumes a conventional von Mises elastic-perfectly plastic law. No viscosity effects are considered since the experimental evidence supporting the assumption of a viscous response of the cellulose is very little. Evidence of the poor deformation recovery of cellulose in amorphous state is provided by molecular models (Chen et al. 2004*a*, Chen et al. 2004*b*). At dry conditions, Chen et al. (2004*a*) determined stress-strain curves for amorphous cellulose, with an average Young modulus $E = 10.42$GPa and a Poisson ratio $\nu = 0.23$. Furthermore, they indicated an onset of plastic yielding at $7-8\%$ strain, corresponding to an approximated yield stress $\sigma_y = 0.8$GPa. Later on, Chen et al. (2004*b*) studied the effects of crosslinks and different water concentrations on stress-strain curves in amorphous cellulose. They reported that the yield stress in stress-strain curves for models containing 50% water was only half the value at dry conditions. Consequently we adopt the above elastic properties and a yield stress $\sigma_y = 0.4$GPa.

(ii) *Crystalline cellulose*

Contrary to amorphous cellulose, the corresponding crystalline fraction is assumed to be elastic (Peura et al. 2007), consisting of a transversally isotropic material. In order to capture this type of constitutive response at large strains, we adopt a generalisation of the compressible version of the isotropic Neo-Hookean strain-energy function. For further details, we refer to Bonet and Burton (1998). Here, it is possible to assume that the Neo-Hookean elastic potential Ψ^{nh} can be decomposed into a fully isotropic component Ψ^{nh}_{iso}, and an orthotropic, transversally isotropic component Ψ^{nh}_{trn}, according to

$$\Psi^{nh} = \Psi^{nh}_{iso} + \Psi^{nh}_{trn}. \tag{5.4}$$

The strain-energy function Ψ^{nh} can be evaluated by knowing the following material constants: the Young modulus and the Poisson ratio of the material on its isotropic plane, E and ν, and the Young modulus and

the shear modulus along the principal axis of orthotropy, E_A and G_A, respectively. The linear elastic mechanical properties chosen here for the crystalline cellulose are $E_A = 134$GPa, $G_A = 4.4$GPa, $\nu = 0.1$ and $E = 27.2$GPa. The same mechanical properties have been used widely in the literature. We refer, for instance, to Bergander and Salmén (2000), Baley (2002) and Salmén (2004).

In Table 1, we list a summary of all the values of mechanical properties used in the modelling of the present chemical constituents.

5.2.3 RVEs Finite element meshes

(i) *Microfibril - RVE*

In order to reduce computing times and memory requirements, point symmetry condition (Ohno et al. (2001) and Saavedra Flores and de Souza Neto (2010)) present in the geometry was taken into consideration. In consequence, only one half of the full RVE domain was modelled. Furthermore, to avoid possible shear locking problems, the final *microfibril*–RVE mesh used was obtained after a convergence analysis. The optimal finite element mesh chosen in this study is illustrated in Figure 5.1(a). To eliminate volumetric locking, the F-Bar methodology (de Souza Neto et al. 1996) is used in all the finite element meshes. The *microfibril*–RVE mesh contains 1008 F-bar eight-noded hexahedral elements with a total number of 2136 nodes.

(ii) *Cellulose core - RVE*

Finally, to obtain the optimal finite element mesh for the cellulose core–RVE, we also carry out here a finite element convergence study. The converged mesh consists of 24 F-bar eight-noded hexahedral elements and a total number of 100 nodes. Figure 5.1(b) shows the corresponding finite element mesh for the cellulose core–RVE.

5.3 Numerical results

In order to better understand the mechanical interactions present at the level of wood cell-wall, we investigate the strain state in the cell-wall when it is subjected to tensile loading in the direction of the cell axis. By means of numerical experiments, we study the viscous relaxation, loading/unloading cycles and the recovery mechanism in the cell-wall. In addition, we explore the effects of the degree of crystallinity on the overall mechanical response.

To make consistent direct comparisons with available experimental information (refer to Keckés et al. (2003)), all measures of stress calculated from the

Material/property	Value	References
Crystalline cellulose		
E_A (GPa)	134.00	(Salmén 2004)
E (GPa)	27.2	(Salmén 2004)
G_A (GPa)	4.4	(Salmén 2004)
ν	0.1	(Salmén 2004)
Amorphous cellulose		
E (GPa)	10.42	(Chen et al. 2004*a*)
ν	0.23	(Chen et al. 2004*a*)
σ_y (GPa)	0.4	(Chen et al. 2004*a*, Chen et al. 2004*b*)
Hemicellulose		
E (GPa)	4e-2[a]	(Salmén 2001)
ν	0.2[a]	(Salmén 2004)
η_p (GPa·s)	8.5	Fitted.[b]
η_m (GPa·s)	3.1	Fitted.[b]
σ_y (GPa)	1.9e-2	Estimated[c] from (Fratzl et al. 2004)
Lignin		
E (GPa)	1.56[d]	Estimated[e] from (Salmén 2004)
ν	0.3[d]	(Salmén 2004)
η_p (GPa·s)	20.0	Fitted.[b]
η_m (GPa·s)	6.5	Fitted.[b]
σ_y (GPa)	1.9e-2	Estimated[c] from (Fratzl et al. 2004)

Table 5.1: Summary of the mechanical properties adopted in the constitutive modelling of the chemical constituents. [a]The linearisation of the Prandtl/Maxwell rheological model adopted for the description of the hemicellulose coincides with a linear elastic response given by a Young modulus $E = 4\text{e-}2\text{GPa}$ and a Poisson ratio $\nu = 0.2$. [b]At present, no experimental data for this constant is available in the literature, neither for isolated hemicellulose nor for isolated lignin. [c]Estimated indirectly by means of the von Mises criterion. Original value was used in the modelling of the hemicellulose-lignin matrix. [d]The linearisation of the Prandtl/Maxwell rheological model adopted for the description of lignin coincides with a linear elastic response given by a Young modulus $E = 1.56\text{GPa}$ and a Poisson ratio $\nu = 0.3$. [e]Estimated from the relationship $G = E/[2(1+\nu)]$, where the shear modulus is $G = 0.6\text{GPa}$ and the Poisson ratio $\nu = 0.3$.

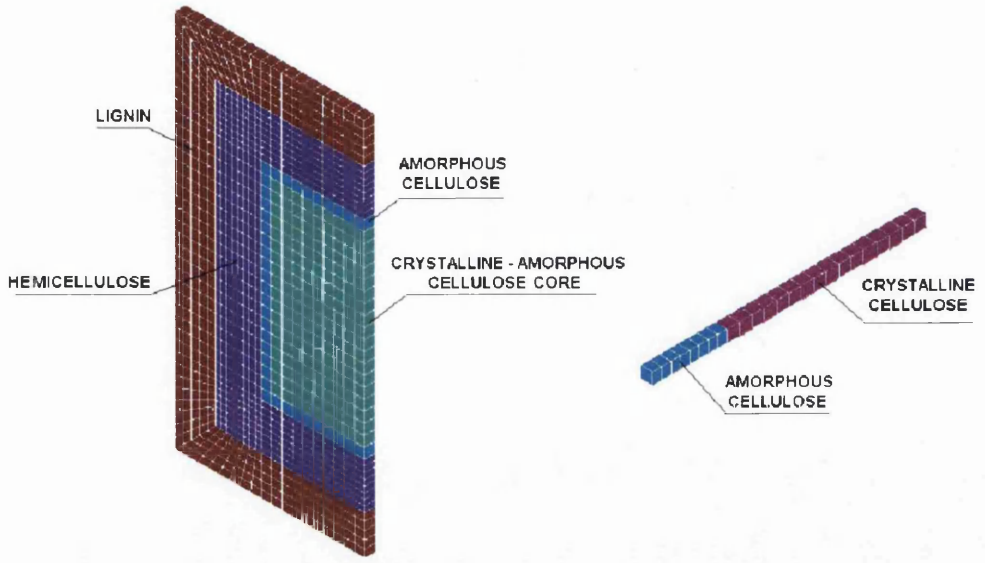

(a) Finite element *microfibril*–RVE mesh. By taking advantage of symmetry conditions, only half of the domain is modelled.

(b) Finite element cellulose core–RVE mesh.

Figure 5.1: Finite element RVE meshes utilised in the present multi-scale model.

homogenised mechanical response of the *microfibril*–RVE model correspond to homogenised first Piola-Kirchhoff stress components (or homogenised nominal stress) measured in the *reference* configuration. For the same reason, *Biot* strain tensor components (de Souza Neto et al. 2008), which measure changes in length per unit *reference* (initial) length, are used here to quantify straining.

In what follows, the cell-wall is assumed to be defined on the x-y plane, with y denoting the cell axis direction, and x, its corresponding normal direction. The z direction is defined perpendicular to the x-y plane, along the cell-wall thickness.

5.3.1 Strain state in the cell-wall under tensile loading

Here, we investigate the strain state in the cell-wall resulting from a tensile load applied in the direction y of the cell axis. By assuming an inextensible cellulose fibre and considering an uniform *microfibril* angle MFA, referred to as μ, it is possible to obtain a simple expression that relates the applied strain, ε_{yy}, in the direction y, with the resulting variation, $\Delta\mu$, of the MFA. If we consider a rectangular material element of cell-wall on the x-y plane, with dimensions lx and ly, in the corresponding x and y directions, it follows that

$\cos(\mu)$ is proportional to ly under the assumption of inextensible cellulose. Then, the relationship between the applied strain and the variation of MFA can be expressed as $\varepsilon_{yy} = -\tan(\mu_o)\Delta\mu$ (Keckés et al. 2003), with μ_o denoting the initial *microfibril* angle. Despite the limitation of this expression to small strains, it has shown good agreement with experimental data for different wood specimens and different MFAs and even for strains up to 20% (Keckés et al. 2003). Similarly, a second relationship can be obtained in the x direction. Here, the length lx in the portion considered of cell-wall, is proportional to $\sin(\mu)$ under the assumption of inextensible fibre. In this case, the strain in the direction x can be calculated as $\varepsilon_{xx} = \cot(\mu_o)\Delta\mu$. Moreover, if we relate the expressions for ε_{xx} and ε_{yy} by means of the in-plane Poisson ratio of the cell-wall, $\nu = -\varepsilon_{xx}/\varepsilon_{yy}$, we can obtain the relationship $\nu = [\cot(\mu_o)]^2$. By taking an initial *microfibril* angle in *compression wood*, equal to 45.7^o (Keckés et al. 2003), we can estimate an in-plane Poisson ratio $\nu = 0.95$ for the cell-wall. High values of in-plane Poisson ratio have been also determined by Marklund and Varna (2009*a*) and Marklund and Varna (2009*b*), for the S2 layer when using classical laminate theory.

With the above estimated in-plane Poisson ratio in the cell-wall, we proceed to define a prescribed incremental strain array to be applied in the *microfibril*–RVE of the cell-wall. If we assume a strain history whose final state in the direction of the cell axis is $\varepsilon_{yy} = 0.2$, a corresponding lateral strain $\varepsilon_{xx} = -0.19$ is obtained under the consideration of $\nu = 0.95$. Also, since *compression wood* cells present thick cell-walls, and considering that the existing load acts only along the axis of the cell, it is reasonable to assume $\varepsilon_{zz} = \gamma_{xz} = \gamma_{yz} = 0$. In addition, the interaction between two or more adjacent cells in wood tissue severely constrains torsion about the cell axis, so that we can assume $\gamma_{xy} = 0$ (Keckés et al. 2003) in the cell-wall. Similarly, for single cells under tensile loading, the torsional rotation is prevented by the tensile testing device and in this case it is also reasonable to take $\gamma_{xy} = 0$ (Marklund and Varna 2009*a*). Finally, the end strain state in the cell-wall, to be prescribed incrementally to the *microfibril*-RVE in the analyses presented in the following, is chosen as

$$\boldsymbol{\varepsilon} = \{\varepsilon_{xx}, \varepsilon_{yy}, \varepsilon_{zz}, \gamma_{xy}, \gamma_{yz}, \gamma_{xz}\}^T = \{-0.19, 0.2, 0, 0, 0, 0\}^T, \qquad (5.5)$$

in standard engineering strain array format.

We emphasise that, in our analyses we assume the cell-wall to be free from pits or defects so that there will be no distinction between the cell-wall in wood tissue and individual cells. Hence, we assume here that the variation $\Delta\mu$, of the MFA, is identical in tissue and in single cells under axial straining. Note, however, that this assumption could be questionable because of the existence of pits and defects over the length of individual cells, which generally results in an inhomogeneous deformation not observed in wood tissue due to the cell-cell interactions mediated by the middle lamella (Keckés et al. 2003).

We also remark that the assumption of inextensible cellulose is used here only to define the macroscopic strain path to be imposed in the analysis of the cell-wall subjected to tensile loads, as an approximation to the actual (more complex) strain path. It should be emphasised though that this assumption is *not* made in the definition of the multi-scale model of the cell wall. That is, in the microfibril-RVE the cellulose fibre (both crystalline and amorphous constituents) is modelled as a deformable material. We note that more realistic strain paths could be naturally obtained if the proposed three-scale model were used in fully coupled three-scale analyses, where the macroscopic (wood tissue level) strain is determined as a result of the corresponding macroscopic equilibrium problem. Fully coupled schemes of this nature are discussed, among others, by Miehe et al. (1999) and Terada et al. (2003) but are not the focus of the present study. The high memory requirements and computing times associated with such methodologies make them a prohibitive alternative for the simulation of large-scale boundary value problems at present. The purpose of our study is precisely to gain insight into the behaviour of wood cell-wall with a view to the future development of new simplified phenomonological constitutive models able to render accurate predictions of macroscopic behaviour at the reasonable computing costs of conventional single scale finite element analyses.

5.3.2 Stress relaxation and recovery mechanism

In this first numerical experiment, we proceed to apply the prescribed strain array, $\boldsymbol{\varepsilon}$, in Equation (5.5), in 32 time steps of 10s each. Consequently, the complete duration is 320s, however in order to investigate the mechanism of viscous relaxation, it is stopped for 30s at time $t_1 = 60$s, $t_2 = 120$s, $t_3 = 190$s and $t_4 = 250$s. Thus the strain rate adopted here, in the direction y, is 1e-3s^{-1}, which has been obtained from Keckés et al. (2003), when a thin wood foil of 50mm length is strained at a rate of 0.05mm/s. In order to study the recovery mechanism, a second numerical experiment is performed, in which the deformation is applied monotonically for 200s at the same strain rate without interruptions. The corresponding component of the homogenised stress array in the direction of the cell axis is plotted in Figure 5.2, for both cases. Here, sharp falls in the level of stresses are observed after each stop of the numerical experiment, as a consequence of the viscosity provided in the lignin-hemicellulose matrix. Furthermore, after stopping and loading again, the level of stress increases and the original stiffness, given by the monotonic straining, is recovered. The same phenomenological response has been experimentally observed by Keckés et al. (2003) in *compression wood* tissue of Norway spruce, under similar conditions of deformation rate, total duration and intervals of stops.

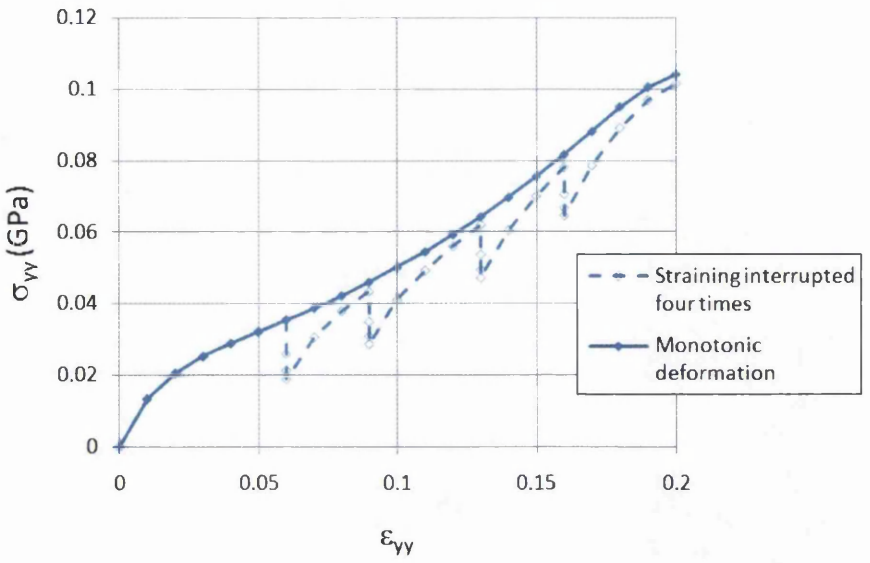

Figure 5.2: Cell-wall under axial tensile straining. Homogenised stress and strain.

5.3.3 Change of MFA under straining

In this section, we continue with the study of the previous numerical experiment, however we focus our attention in the variation of the *microfibril* angle MFA with the applied strain ε_{yy}. In this case, whether or not interruptions occur in the monotonic loading process is immaterial in the evolution of the MFA. Note that interrupting the straining in our model at any instant causes no variation in the orientation of the *microfibril* because of the prescription of the strain state.

Figure 5.3 shows both the experimental information reported in the literature (Keckés et al. 2003) during a tensile test of *compression wood* tissue, and the result obtained from the analysis of the *microfibril*–RVE. The general trend of the numerical curve is almost linear, showing an increase of the slope at the end of the complete deformation process in 3.5% (though not visible in the graph) with respect to the initial slope. This slight increase is due mainly to the geometric non-linear relationship between the prescribed strain and the variation of MFA. Note that the linear relationship assumed in Section 5.3.1, between the applied strain and the variation of MFA, is used exclusively to calculate the final strain state in the loading programme. However, it does not impose an exact linear variation between the *microfibril* orientation and the prescribed strain along the deformation process.

From numerical experiments (not shown here), we also note that the changes in the in-plane Poisson ratio can lead to substatial variations in slope in the graph of Figure 5.3. In addition, a relatively constant in-plane Pois-

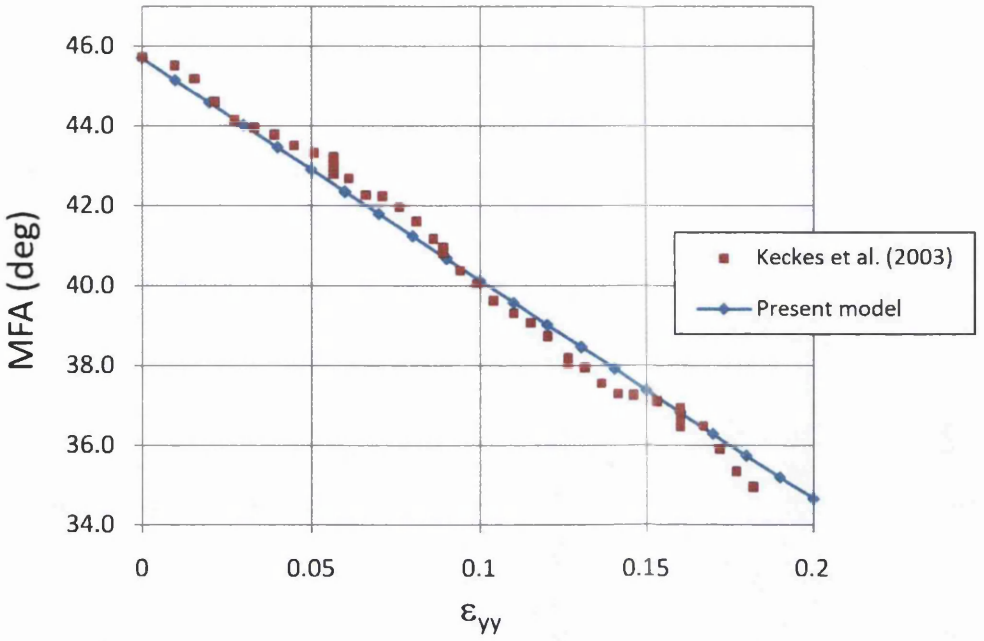

Figure 5.3: Change of MFA in the cell-wall under straining. Tensile experiment in *compression wood* tissue (Keckés et al. 2003) and numerical simulation.

son ratio during the deformation process results in a general linear trend. Therefore, the good agreement between numerical and experimental results suggests that a suitable Poisson ratio has been obtained when the expression $\nu = [\cot(\mu_o)]^2$ is used along with an initial *microfibril* angle $\mu_o = 45.7^o$. We note, however, that for lower (initial) *microfibril* angles, this expression will fail to predict the Poisson ratio. This is explained by the fact that for smaller MFAs the cellulose fibres begin to take larger portions of the axial loads leading to higher axial deformations. Then, the assumption of inextensible cellulose in this case is not clearly reasonable and the corresponding expression $\nu = [\cot(\mu_o)]^2$ will lead to unacceptable results for the Poisson ratio.

5.3.4 Loading/unloading cycles

Here, we investigate the effects of cyclic loading on the wood cell-wall. For comparison purposes, we select the experiment reported by Keckés et al. (2003), consisting of three loading/unloading cycles applied on a *compression wood* cell of Norway spruce. In this particular experiment, stresses were calculated considering the full initial area of the cell cross-section, including the area of the cell lumen (or central cavity). Consequently, in order to make it possible to compare our numerical simulations with this experiment, the ho-

mogenised stress values shown here (refer to Figure 5.4) have been divided by a factor 1.66. This factor is obtained by dividing the full initial area of the cell cross-section (including the cell lumen) by the net area of the cross-section after deduction of the lumen. Here, the corresponding factor is calculated considering the diameter of the tested cell reported by Keckés et al. (2003), equal to 25μm, and a thickness of 4.6μm, indicated as a mean wall thickness for *compression wood* cells of Norway spruce according to Tarmian and Azadfallah (2009). In addition, since the cell is long enough, with walls assumed to be free of pits and defects, a uniform deformation is considered along the cell, for the range of strains in study.

The experiment reported by Keckés et al. (2003) (Figure 5.4) shows a maximum strain of 0.22 in the cell-axis direction before total failure of the specimen. Consequently, in order to reach this maximum strain, we proceed to apply the prescribed strain array $\boldsymbol{\varepsilon}$, in Equation (5.5), but multiplied by a factor 1.1. That is to say, here we apply a prescribed strain array $\boldsymbol{\varepsilon} = \{-0.209, 0.22, 0, 0, 0, 0\}^T$, applied in 101 time steps of 5s each one. The adopted strain rate is 6.58e-4s^{-1} and is calculated from Keckés et al. (2003), when the tested cell of 0.76mm length is strained at a rate of 500nm/s. For unloading/reloading the same strain rate is used under contraction/stretching.

The corresponding time intervals of tensile straining are: [0,60]s, [75,110]s, [125,250]s and [305,505]s. For unloading, the intervals are [60,75]s, [110,125]s and [250,305]s. In order to investigate the recovery mechanism in the material, we perform another analysis under monotonic straining at the same strain rate. Figure 5.4 presents the stress-strain curves obtained in the experimental test of Keckés et al. (2003) and in the two numerical simulations. As in the previous examples, the direction of analysis is the cell axis. The corresponding graph shows a good agreement between the numerical simulations and the experimental result, which demonstrates the very good predictive capabilities of the present model. Moreover, after each loading/unloading cycle in the numerical curve, the level of stress tends to reach the original stiffness of the monotonic straining curve. This shows once more the ability of the model to capture the recovery mechanism at the cell-wall level. In addition, we also observe that the model is able to reproduce with accuracy the characteristic stiffening developed in the cell-wall, when the *microfibril* angle, MFA, decreases under the continued straining.

In spite of the good predictive capabilities shown by the present model, Figure 5.4 shows very low dissipated energy after the first and second hysteresis loop, when the response is supposed to be predominantly elastic. To address this issue, we remark however, that further improvements could be obtained with the adoption of more precise viscosity-related material constants obtained directly from experiments carried out on lignin and hemicellulose. In any case, a much better response is found in the third hysteretic cycle, when both numerical and experimental curves tend to coincide.

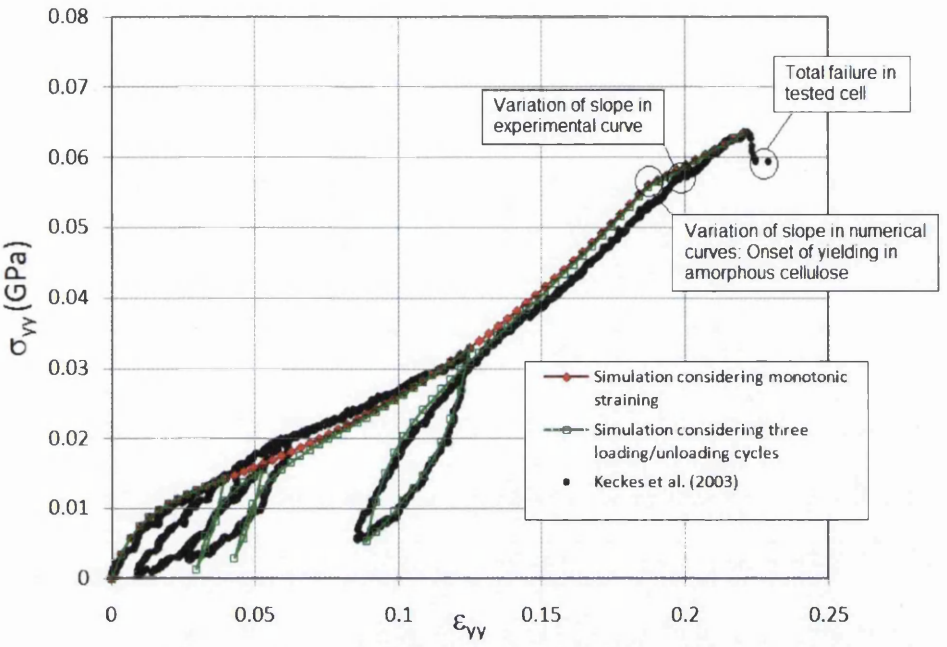

Figure 5.4: Loading/unloading cycles. Experimental test in *compression wood* cell (Keckés et al. 2003) and two numerical simulations.

5.3.5 Degree of crystallinity

In this section we investigate the variation of the degree of crystallinity, ev, in the overall mechanical response of the wood cell-wall. We compare the material response predicted by the *microfibril*–RVE for four different degrees of crystallinity, 45, 50, 55 and 60%. The different values of crystallinity are obtained in the model by suitably changing the length of the amorphous cellulose fraction between two consecutive crystalline portions, keeping constant the thickness of the outer amorphous cellulose layer. By setting the volume fraction of amorphous cellulose in the cellulose core–RVE model, we obtain four different *microfibril*–RVE models. Note that we compare here the overall response of the four different models, under the prescription of the same monotonically incremental engineering strain array $\boldsymbol{\varepsilon}$, in Equation (5.5), assuming that this strain state is representative for all the cases analysed. This is possible since $\boldsymbol{\varepsilon}$ has been obtained from considerations independent of the volume fractions of material and mechanical properties (we have assumed only that the cellulose fibre is much stiffer than the matrix). The adopted strain rate is 1e-3s^{-1}.

Figure 5.5 shows the stress-strain curves for the different degrees of crystallinity considered. In the corresponding graph, we see that the mechanical response is virtually independent of the degree of crystallinity for strains un-

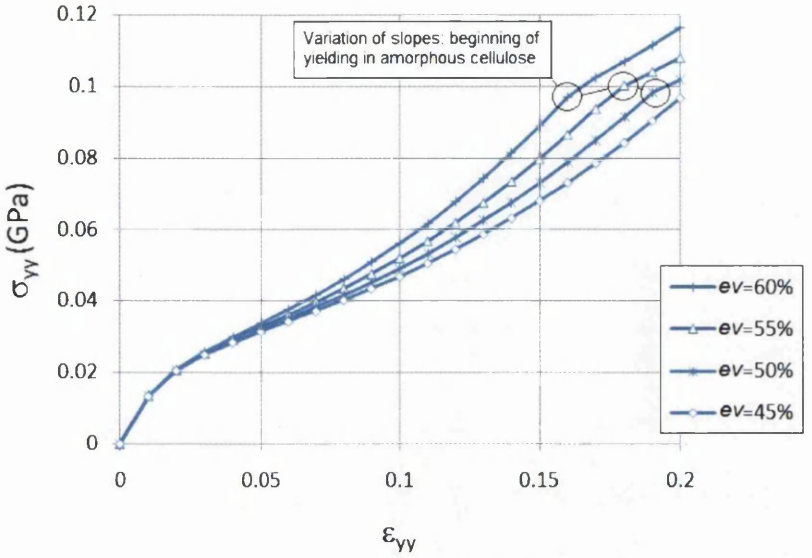

Figure 5.5: Stress-strain diagrams in the cell-wall, obtained from the *microfibril*–RVE with different degrees of crystallinity, *ev*.

der 4-5%. From the numerical results, it can be concluded that up to this level of strain, the cellulose fibre remains almost inextensible. After 8-9% of strain, however, the dependence of the response on the degree of crystallinity becomes more considerable. The little influence of the degree of crystallinity on the overall mechanical response at lower strain levels is attributed to the high MFAs (near 45%) at this stage. Here, only a small portion of the axial load is carried by the cellulose. In addition, the main mechanism of deformation in the cell-wall is shear, localised in the hemicellulose/lignin matrix, due to the relative displacements among cellulose fibres undergoing rigid body rotation and alignment in the direction of the external loads. Therefore, any increase of the stiffness in the cellulose due to a rise in the degree of crystallinity will not affect significantly the overall mechanical response of the cell-wall under low strain levels since the cellulose fibre will experience predominantly changes in its orientation rather than straining along its own axis. If the straining process continues, the *microfibril* angle will reduce considerably and the cellulose fibres will begin to take larger portions of axial loads and the overall response will stiffen accordingly. At this stage, the influence of the degree of crystallinity on the global mechanical response of the cell-wall will become significantly more pronounced as shown in Figure 5.5. We note that a higher influence of the degree of crystallinity on the macroscopic response should be observed throughout the entire loading process for smaller values of (initial) *microfibril* angles.

Another interesting aspect that can be observed in Figure 5.5 is the fact

that the onset of inelastic yielding in the cellulose fibre occurs for lower levels of strains, when the degree of crystallinity is increased. After about 15% of strain in the *microfibril*–RVE, curves show a slight change in their slopes. A further inspection of the numerical results shows that this slight change of the slope represents the beginning of yielding in the cellulose, specifically in the amorphous fraction. For instance, in the *microfibril*–RVE model with 60% of crystallinity, the cellulose starts to yield at about 16% of strain, however in the RVE model with degree of crystallinity 45%, cellulose begins to yield at strain level above 20%.

A third very important conclusion can be reached by examining Figures 5.4 and 5.5. Analogously to the curves of Figure 5.5, the experimental curve presented in Figure 5.4 shows a slight variation in its slope at about 20% strain, very close to the total failure of the tested cell. This variation of the slope in the numerical results (refer to Figure 5.4, about 19% strain) is caused by the onset of yielding in the amorphous region of the cellulose. The fact that the cell collapses almost immediately after the amorphous cellulose reaches the condition of plasticity, would indicate that yielding in the non-crystalline portion of cellulose would correspond to a mechanism of failure in the wood cell under straining. In fact, this explanation seems to be reasonable since the failure of the amorphous cellulose would jeopardize the whole integrity of the cellulose fibre and consequently, of the entire unit.

By taking these last two conclusions into consideration, the fact that an increase in the crystallinity would mean an onset of yielding in the amorphous cellulose for lower levels of strain, and that yielding of the amorphous cellulose would result in a potential mechanism of failure in the cell-wall, we could also conclude that the increase in the degree of crystallinity would result in a potential failure in the wood cell-wall for smaller strains. It is not a surprise that we arrive at this conclusion, since highly crystalline cellulosic materials show a very stiff response with low values of strain at fracture.

CHAPTER 6
Conclusions

The irreversible behaviour of wood cell-walls has been investigated by means of a finite element- based computational multi-scale approach. A finite strain three-scale model has been proposed under the periodic boundary displacement fluctuations kinematic constraint. where the overall response of the cell-wall composite is obtained by the computational homogenisation of a Representative Volume Element (RVE) of cell-wall material, called here *microfibril*–RVE, whose mechanical response prediction, in turn, is described by the computational homogenisation of a cellulose core RVE.

Numerical material tests have been conducted and the results have been compared to published experimental data, demonstrating the predictive capability of the proposed model. In particular, the model is able to capture phenomena such as fibre reorientation-induced stiffening, viscous relaxation, recovery mechanism and hysteresis. The analyses presented in this thesis suggest the inelastic yielding of the amorphous cellulose as the main mechanism of failure of the cell-wall under straining.

In addition, in order to reduce CPU times in the present three-scale finite element model, this research has also addressed the use of symmetry conditions to reduce computing times in multi-scale models. Two types of symmetry often present in materials of practical interest have been considered: staggered-translational and point symmetry. These have been considered under the three common types of assumed kinematical constraints of the RVE: Periodic boundary fluctuations; linear boundary displacement, and minimum constraint (or uniform boundary traction model). Their direct implementation within a Newton-Raphson based iterative procedure for the finite element solution of the RVE equilibrium problem is straightforward and for completeness has been shown in detail. Numerical examples have shown that as expected this leads to substantial savings in computing times. Speed-up factors in excess of seven have been found in such cases when both symmetry conditions considered are present at the same time. In conclusion, it appears that any efforts to improve overall efficiency in this context, such as the use of special solvers and parallel computing strategies, should be considered in conjunction with the (far more straightforward) implementation of the relevant RVE symmetry conditions.

The present modelling strategy, with the support of experimental work, can provide a robust platform for further investigations on the dissipative response of wood with a particular view to clarify features of the microscopic

behaviour, and their influence on the macroscopic response, which are not well-understood at present. For example, inclusion of further non-linear mechanisms such as frictional contact and debonding between phases is relatively straightforward and are likely to shed more light into the constitutive behaviour of such materials. Moreover, possible studies to establish functional forms of macroscopic failure surfaces for wood based on the present framework, or the development of new materials inspired in the structure and mechanics of wood cell-wall, are some the subjects to carry out in a near future.

Bibliography

Altaner, C. M. and Jarvis, M. C. (2008), 'Modelling polymer interactions of the 'molecular velcro' type in wood under mechanical stress', *Journal of Theoretical Biology* **253**(3), 434–445.

Amestoy, P. R. and Duff, I. S. (1993), 'Memory management issues in sparse multifrontal methods on multiprocessors', *International Journal of Supercomputer Applications* **7**, 64–82.

Andersson, S. (2006), A study of the nanostructure of the cell wall of the tracheids of conifer xylem by x-ray scattering, PhD thesis, University of Helsinki, Finland.

Andersson, S., Wikberg, H., Pesonen, E., Maunu, S. L. and Serimaa, R. (2004), 'Studies of crystallinity of scots pine and norway spruce cellulose', *Trees - Structure and Function* **18**(3), 346–353.

Baley, C. (2002), 'Analysis of the flax fibres tensile behaviour and analysis of the tensile stiffness increase', *Composites Part A: Applied Science and Manufacturing* **33**(7), 939–948.

Bergander, A. and Salmén, L. (2000), 'Variations in transverse fibre wall properties: Relations between elastic properties and structure', *Holzforschung* **54**(6), 654–660.

Bodig, J. and Jayne, B. (1982), *Mechanics of wood and wood composites*, Von Nostrand Reinhold, New York.

Bonet, J. and Burton, A. (1998), 'A simple orthotropic, transversaly isotropic hyperelastic constitutive equation for large strain computations', *Computer Methods in Applied Mechanics and Engineering* **162**, 151–164.

Booker, R. and Sell, J. (1998), 'The nanostructure of the cell wall of softwoods and its functions in a living tree', *European Journal of Wood and Wood Products. Holz als Roh- und Werkstoff* **56**(1).

Burgert, I., Keckés, J. and Fratzl, P. (2006), Mechanics of the wood cell wall, *in* 'Characterization of the cellulosic cell wall', Blackwell Publishing, Oxford, pp. 30–37.

Castaneda, P. P. (1991), 'The effective mechanical properties of nonlinear isotropic composites', *Journal of the Mechanics and Physics of Solids* **39**, 45–71.

Chen, W., Lickfield, G. C. and Yang, C. Q. (2004*a*), 'Molecular modeling of cellulose in amorphous state. part i: model building and plastic deformation study', *Polymer* **45**(3), 1063–1071.

Chen, W., Lickfield, G. C. and Yang, C. Q. (2004*b*), 'Molecular modeling of cellulose in amorphous state part ii: effects of rigid and flexible crosslinks on cellulose', *Polymer* **45**(21), 7357–7365.

de Souza Neto, E. A. and Feijóo, R. (2010), Variational foundations of large strain multi-scale solid constitutive models: Kinematical formulation, *in* M. V. Jr., E. de Souza Neto and P. M. oz Rojas, eds, 'Advanced multi-scale material modelling: From classical to multi-scale techniques', Wiley: Chichester. (to appear).

de Souza Neto, E. A. and Feijóo, R. A. (2006), 'Variational foundations of multi-scale constitutive models of solid: Small and large strain kinematical formulation', *National Laboratory for Scientific Computing (LNCC), Brazil, Internal Research and Development Report 16/2006* .

de Souza Neto, E. A., Perić, D., Dutko, M. and Owen, D. R. J. (1996), 'Design of simple low order finite elements for large strain analysis of nearly incompressible solids', *International Journal of Solids and Structures* **33**, 3277–3296.

de Souza Neto, E. A., Perić, D. and Owen, D. R. J. (2008), *Computational Methods for Plasticity: Theory and Applications*, Wiley: Chichester.

Dinwoodie, J. (1981), *Timber – Its nature and behavior*, Von Nostrand Reinhold, New York.

Donaldson, L. A. and Singh, A. P. (1998), 'Bridge-like structures cellulose microfibrils', *Holzforschung* **52**(5), 449–454.

Fengel, D. and Stoll, M. (1973), 'Variation in cell cross-sectional area, cell-wall thickness and wall layers of spruce tracheids within an annual ring', *Holzforschung* **27**, 1–7.

Fratzl, P., Burgert, I. and Keckes, J. (2004), 'Mechanical model for the deformation of the wood cell wall', *Zeitschrift fuer Metallkunde / Materials Research and Advanced* **7**(95), 579–584.

Gardner, D. (2002), Wood surface properties, *in* 'Wood structure and properties '02', Arbora Publishers, Zvolen, Slovakia, pp. 87–89.

Giusti, S. M., Blanco, P. J., de Souza Neto, E. A. and Feijóo, R. A. (2009), 'An assessment of the gurson yield criterion by a computational multi-scale approach', *Engineering Computations* **26**(3), 281–301.

Giusti, S. M., Novotny, A. A., de Souza Neto, E. A. and Feijóo, R. A. (2009), 'Sensitivity of the macroscopic elasticity tensor to topological microstructural changes', *Journal of the Mechanics and Physics of Solids* **57**(3), 555–570.

Hill, R. (1965), 'A self-consistent mechanics of composite materials', *Journal of the Mechanics and Physics of Solids* **13**(4), 213–222.

Hofstetter, K., Hellmich, C. and Eberhardsteiner, J. (2005), 'Development and experimental validation of a continuum micromechanics model for the elasticity of wood', *European Journal of Mechanics A/Solids* **24**(6), 1030–1053.

Hofstetter, K., Hellmich, C. and Eberhardsteiner, J. (2007), 'Micromechanical modeling of solid-type and plate-type deformation patterns within softwood materials. a review and an improved approach', *Holzforschung* **61**(4), 343–351.

Holmberg, S., Persson, K. and Petersson, H. (1999), 'Nonlinear mechanical behaviour and analysis of wood and fibre materials', *Computers and Structures* **72**(4-5), 459–480.

Keckés, J., Burgert, I., Frühmann, K., Müller, M., Kölln, K., Hamilton, M., Burghammer, M., Stanzl-Tschegg, S. and Fratzl, P. (2003), 'Cell-wall recovery after irreversible deformation of wood', *Nature Materials* **2**, 811–814.

Kollman, F. and Côté, W. (1968), *Principles of wood science and technology*, Vol. 1. Solid wood, Springer-Verlag, Berlin.

Lemaitre, J. and Chaboche, J. L. (1990), *Mechanics of Solid Materials*, Cambridge University Press, Cambrige.

Mandel, J. (1971), *Plasticit´e Classique et Viscoplasticit´e. CISM Lecture Notes*, Springer-Verlag, Udine, Italy.

Marklund, E. and Varna, J. (2009*a*), 'Modeling the effect of helical fiber structure on wood fiber composite elastic properties', *Applied Composite Materials* **16**(4), 245–262.

Marklund, E. and Varna, J. (2009*b*), 'Modeling the hygroexpansion of aligned wood fiber composites', *Composites Science and Technology* **69**(7-8), 1108–1114.

Marsden, J. and Hughes, T. (1983), *Mathematical Foundations of Elasticity*, Prentice-Hall, New Jersey.

Matsui, K., Terada, K. and Yuge, K. (2004), 'Two-scale finite element analysis of heterogeneous solids with periodic microstructures', *Computers and Structures* **82**, 593–606.

Michel, J. C., Moulinec, H. and Suquet, P. (1999), 'Effective properties of composite materials with periodic microstructure: a computational approach', *Computer Methods in Applied Mechanics and Engineering* **172**, 109–143.

Miehe, C., Shotte, J. and Lambrecht, M. (2002), 'Homogenization of inelastic solid materials at finite strains based on incremental minimization principles. application to the texture analysis of polycrystals', *Journal of the Mechanics and Physics of Solids* **50**(10), 2123–2167.

Miehe, C., Shotte, J. and Schröder, J. (1999), 'Computational micro-macro transitions and overall moduli in the analysis of polycrystals at large strains', *Computational Materials Science* **16**, 372–382.

Navi, P. (1995), 'Micromechanics of wood subjected to axial tension', *Wood Science and Technology* **29**(6), 411–429.

Nilsson, T. and Gustafsson, P. J. (2007), 'Influence of dislocations and plasticity on the tensile behaviour of flax and hemp fibres', *Composites Part A: Applied Science and Manufacturing* **38**(7), 1722–1728.

Ohno, N., Matsuda, T. and Wu, X. (2001), 'A homogenization theory for elastic-viscoplastic composites with point symmetry of internal distributions', *International Journal of Solids and Structures* **38**, 2867–2878.

Pellegrino, C., Galvanetto, U. and Schrefler, B. A. (1999), 'Numerical homogenization of periodic composite materials with non-linear material components', *International Journal for Numerical Methods in Engineering* **46**, 1609–1637.

Perić, D. and Dettmer, W. (2003), 'A computational model for generalized inelastic materials at finite strains combining elastic, viscoelastic and plastic material behaviour', *Engineering Computations* **20**(5/6), 768–787.

Perré, P. and Keey, R. (2007), Drying of wood: principles and practices, *in* 'Handbook of industrial drying', CRC Press, USA, pp. 821–878.

Peura, M., Kölln, K., Grotkopp, I., Saranpää, P., Müller, M. and Serimaa, R. (2007), 'The effect of axial strain on crystalline cellulose in norway spruce', *Wood Science and Technology* **41**(7), 565–583.

Qing, H. and Mishnaevsky, L. (2009*a*), '3d hierarchical computational model of wood as a cellular material with fibril reinforced, heterogeneous multiple layers', *Mechanics of Materials* **41**(9), 1034–1049.

Qing, H. and Mishnaevsky, L. (2009*b*), 'Moisture-related mechanical properties of softwood: 3d micromechanical modeling', *Computational Materials Science* **46**(2), 310–320.

Qing, H. and Mishnaevsky, L. (2010), '3d multiscale micromechanical model of wood: From annual rings to microfibrils', *International Journal of Solids and Structures* **47**(9), 1253–1267.

Reese, S. and Govindjee, S. (1998), 'A theory of finite viscoelasticity and numerical aspects', *International Journal of Solids and Structures* **35**(26), 3455–3482.

Saavedra Flores, E. I. and de Souza Neto, E. A. (2010), 'Remarks on symmetry conditions in computational homogenisation problems', *Engineering Computations* **27**(4), 551–575.

Saavedra Flores, E. I., de Souza Neto, E. A. and Pearce, C. (2011), 'A large strain computational multi-scale model for the dissipative behaviour of wood cell-wall', *Computational Materials Science* **50**(3), 1202–1211.

Salmén, L. (2001), Micromechanics of the wood cell wall: a tool for the better understanding of its structure, *in* P. Navi, ed., 'Proceedings of 1st International Conference of the European Sociaty for Wood Mechanics', EPFL, Lausanne, Switzerland, pp. 385–398.

Salmén, L. (2004), 'Micromechanical understanding of cell-wall structure', *Comptes Rendus Biologies* **327**(9-10), 873–880.

Sedighi-Gilani, M. and Navi, P. (2007), 'Experimental observations and micromechanical modeling of successive-damaging phenomenon in wood cells' tensile behavior', *Wood Science and Technology* **41**(1), 69–85.

Smith, I., Landis, E. and Gong, M. (2003), *Fracture and fatigue in wood*, John Wiley & Sons Ltd, Chichester.

Somer, D. D., de Souza Neto, E. A., Dettmer, W. G. and Perić, D. (2009), 'A sub-stepping scheme for multi-scale analysis of solids', *Computer Methods in Applied Mechanics and Engineering* **198**, 1006–1016.

Speirs, D. C. D., de Souza Neto, E. A. and Perić, D. (2008), 'An approach to the mechanical constitutive modelling of arterial tissue based on homogenization and optimization', *Journal of Biomechanics* **41**, 2673–2680.

Suquet, P. (1993), 'Overall potentials and extremal surfaces of power law or ideally plastic materials', *Journal of the Mechanics and Physics of Solids* **41**, 981–1002.

Tarmian, A. and Azadfallah, M. (2009), 'Variation of cell features and chemical composition in spruce consisting of opposite, normal, and compression wood', *BioResources* **1**(4), 194–204.

Terada, K., Saiki, I., Matsui, K. and Yamakawa, Y. (2003), 'Two-scale kinematics and linearization for simultaneous two-scale analysis of periodic heterogeneous solids at finite strains', *Computer Methods in Applied Mechanics and Engineering* **192**, 3531–3563.

Timar-Balazsy, A. and Eastop, D. (1998), *Chemical principles of textile conservation*, Butterworth – Heinemann, Oxford.

Timell, T. (1982), 'Recent progress in the chemistry and topochemistry of compression wood', *Wood Science and Technology* **16**(2), 83–122.

Timell, T. (1986), *Compression wood in gymnosperms*, Springer, Berlin.

Tsoumis, G. (1991), *Science and technology of wood: Structure, properties, utilization*, Von Nostrand Reinhold, New York.

Watanabe, I., Terada, K., de Souza Neto, E. and Perić, D. (2008), 'Characterization of macroscopic tensile strength of polycrystalline metals with two-scale finite element analysis', *Journal of the Mechanics and Physics of Solids* **56**, 1105–1125.

Watanabe, U., Norimoto, M. and Morooka, T. (2000), 'Cell wall thickness and tangential young's modulus in coniferous early wood', *Journal of Wood Science* **46**, 109–114.

Wellmann, C. and Wriggers, P. (2008), 'Comparison of the macroscopic behavior of granular materials modeled by different constitutive equations on the microscale', *Finite elements in analysis and design* **44**, 259–271.

Xu, P., Donaldson, L. A., Gergely, Z. R. and Staehelin, L. A. (2007), 'Dual-axis electron tomography: a new approach for investigating the spatial organization of wood cellulose microfibrils', *Wood Science and Technology* **41**(2), 101–116.